Synthesis, Photophysical Properties and Electron Transfer Dynamics of Perovskite Nanocrystal Heterostructures

By

Yang Yongge

THE UNIVERSITY OF ELECTRO-COMMUNICATIONS

2024

Synthesis, Photophysical Properties and Electron Transfer Dynamics of Perovskite Nanocrystal Heterostructures

Yang Yongge

Doctor of Philosophy

THE UNIVERSITY OF ELECTRO-COMMUNICATIONS

GRADUATE SCHOOL OF INFORMATICS AND ENGINEERING

MARCH 2024

Synthesis, Photophysical Properties and Electron Transfer Dynamics of Perovskite Nanocrystal Heterostructures

SUPERVISOR: Prof. Qing Shen

APPROVED BY THE DOCTORAL DISSERTATION REVIEW COMMITTEE:

平野　誉	(Takashi Hirano)	教授
奥野　剛史	(Tsuyoshi Okuno)	教授
曽我部　東馬	(Tomah Sogabe)	准教授
早瀬　修二	(Shuzi Hayase)	特任教授
沈　青	(Qing Shen)	教授

和文要旨

近年、ペロブスカイトナノ結晶ヘテロ接合は、ナノ結晶システムの応用範囲を大幅に拡大し、さまざまな用途における光電子デバイスの性能を向上させることができるため、多くの注目を集めている。 しかし、従来溶液プロセスに基づくペロブスカイトナノ結晶ヘテロ接合は、主に 2 つの成分を混合する（2 段階法としても知られる）ことによって形成され、通常は安定性と光励起キャリアの移動に問題がある。またその形成メカニズムの理解とヘテロ界面の制御も困難であった。本研究では、ペロブスカイトナノ結晶のヘテロ接合をその場室温でエピタキシャル成長させる 1 ステップ合成法を開発した。この新しい合成法によるペロブスカイトナノ結晶のヘテロ接合の形成機構を明らかにした。さらに、これらのヘテロ接合界面において非常に高速な電荷移動が発生することを見出した。

第 1 章では、主に本論文の研究背景を紹介した。 量子ドットやペロブスカイトナノ結晶は、フォトルミネッセンスの量子収率が高く、バンドギャップを調整でき、溶液処理が可能な特性から大きな注目を集めている。 これに加えて、ペロブスカイトナノ結晶ヘテロ接合は、これらの特性を強化または拡張するプラットフォームとしての可能性を秘めている。 そこで、第 1 章では、量子ドットとペロブスカイトナノ結晶の開発経緯、光電子特性、合成法を概観した上で、ペロブスカイトナノ結晶ヘテロ接合の合成法、構造、物性、応用について紹介する。

第 2 章では、この論文に関連する計測と特性評価の方法について説明した。 主にフォトルミネッセンス分光法(PL)、時間依存蛍光分光法(TRPL)、フォトルミネッセンス量子収率法(PLQY)、紫外可視近赤外吸収分光法(UV-Vis)、フーリエ変換赤外分光法(FT-IR)、X 線回折分析(XRD)、X 線光電子分光法(XPS)、斜入射広角 X 線散乱法(GI-WAX)、過渡吸収分光法(TAS)、透過型電子顕微鏡(TEM)が含まれた。

第 3 章では、完全コロイド $CsPbBr_3$–PbS ヘテロ構造を室温でその場合成する手法を紹介し、短波赤外イメージングの可能性を実証した。 全コロイド状

の $CsPbBr_3$-PbS ヘテロ構造の合成は、Cs-DOPA(ジイソオクチルホスホン酸)を TOPO-$PbBr_2$(トリオクチルホスフィンオキシド)系に導入し、爆発的な核生成と緩慢な成熟プロセスを引き起こし、続いてトリメチルアンモニウムチオ硫化($(TMS)_2S$)を導入して in situ ヘテロ構造の形成を引き起こすことによって達成された。 本研究で作製した全コロイド量子ドット $CsPbBr_3$-PbS ヘテロ構造は、優れた溶液加工性を持ち、可視および赤外スペクトル範囲で持続可能なデュアルエミッションを示す。TEM、XRD、XPS を用いて、全コロイド状 $CsPbBr_3$-PbS ヘテロ構造の形成に成功したことを確認した。ヘテロ接合界面におけるペロブスカイト量子ドットから PbS 量子ドットへの超高速キャリア注入(開始時間<1 ps) を実証した。 さらに、本研究で作製した全コロイド $CsPbBr_3$-PbS ヘテロ構造は、周囲条件下で可視スペクトルと赤外スペクトルで調整可能で耐久性のある二重発光を示し、180 時間以上の連続太陽放射にも耐えることがわかった。全コロイド $CsPbBr_3$-PbS ヘテロ構造の蛍光特性は、Pb/S モル比を 1:1 ～ 1:30 の範囲で調整することで簡単に調整できる (CsPbBr3 の場合: 505 ～ 471 nm、PbS の場合: 950 ～ 1156 nm)。 本研究で開発した全コロイド $CsPbBr_3$-PbS ヘテロ構造に対して、まず短波赤外イメージング(SWIR:波長 1000-2000nm)への応用を試みたところ、365nm 励起で純粋な PbS 量子ドットよりも高い分解能を達成し、応答閾値は 18mW/cm^2 と低く、国際電気標準会議(IEC)の安全閾値(10mW/cm^2)に近かった。本研究は、低コストで超高速電荷移動が可能な量子ドットヘテロ構造を構築するための革新的な道筋を明らかにし、将来の応用への道を切り拓くものである。

第 4 章では、室温で溶液処理可能な in-situ エピタキシャル成長法を開発し、初めて２次元 (2D) －３次元 (3D) PMA_2PbBr_4-$CsPbBr_3$ ナノ結晶横ヘテロ接合の作製に成功した。 ここで、ナノ結晶ヘテロ接合の合成は、良溶媒に溶解した CsBr、$PbBr_2$、PMA(ベンザミン)および BA(安息香酸)の前駆体溶液を貧溶媒に迅速に注入することによって達成された。反応中、$CsPbBr_3$ ナノ結晶は溶液中で遊離 PMA^+イオンと臭化鉛イオンの結合を誘導し、それによって $CsPbBr_3$ の表面上で PMA_2PbBr_4 の熱力学的に安定した in-situ 成長を引き起こした。その結果、$[PbBr_4]^{6-}$八面体の 2 つの成分が直接結合し、絶縁性有機カチオンのブ

ロッキングを回避する。STEM、XRD、斜入射広角 X 線回折(GI-WAX)、XPS などの分析法を用いて、2D-3D PMA_2PbBr_4- $CsPbBr_3$ナノ結晶横ヘテロ接合の合成に成功したことを確認できた。第一原理計算(DFT)は、このヘテロ接合の形成が熱力学的制御によるものであることを理論的にサポートした。温度可変蛍光分光測定結果により、界面の強い化学結合は PMA_2PbBr_4 に大きな格子歪みをもたらしたことが示唆された。また、TRPL や TAS より、この２D-3D ヘテロ構造における光励起キャリアの超高速移動過程を解明した。本研究は、$[PbBr_4]^{6-}$八面体の直接結合による 2D-3D ナノ結晶ヘテロ接合の構築に革新的な道筋を提供し、それらの合成化学と光物性を研究するための優れたプラットフォームとして、将来の応用への指針を与えることができる。

第 5 章では、本論文の研究内容と結論をまとめ、ペロブスカイト系ナノ結晶ヘテロ接合の今後の開発の方向性と応用に述べた。

Abstract

In recent years, perovskite nanocrystal heterojunctions have attracted significant attention due to their ability to greatly expand the application scope of nanocrystal systems and enhance the performance of optoelectronic devices across various applications. However, most perovskite nanocrystal heterojunctions prepared through solution processing, commonly known as the two-step method, involve mixing two components, leading to poor stability and charge carrier transfer properties. This complexity has made it challenging to understand the formation mechanisms and control the interfaces of these heterojunctions. Furthermore, from the perspectives of synthetic chemistry and photophysics, developing a low-cost, reproducible method and employing chemical bonds as the bonding mode for heterojunction interfaces to demonstrate rapid charge carrier transfer pose significant challenges. Addressing these challenges is essential to unleash the full potential of perovskite nanocrystal heterojunctions in practical applications. In this study, we have developed a one-step synthesis method for in situ room-temperature epitaxial growth of heterojunctions using different types of perovskite nanocrystals. Based on our developed approach, we have extensively investigated the synthetic chemistry, photophysical properties, and charge carrier transfer characteristics of these heterojunctions.

Specifically, in the Chapter 1, we primarily delve into the research background of this thesis. Quantum dots and perovskite nanocrystals have garnered considerable attention due to their high photoluminescent quantum yields, tunable bandgaps, and solution processability. Furthermore, the heterojunctions formed by perovskite nanocrystals serve as a promising platform with the potential to enhance or extend these properties. Thus, in this Chapter 1, we systematically review the developmental trajectory and optoelectronic properties of quantum dots and perovskite nanocrystals. We elucidate their synthesis methods and subsequently introduce the synthesis techniques, structures, properties, and applications of heterojunctions based on perovskite nanocrystals.

In the Chapter 2, we provide an overview of the instruments and characterization methods relevant to this thesis. This encompasses photoluminescence spectroscopy (PL), time-resolved photoluminescence spectroscopy (TRPL), photoluminescent quantum yield measurements (PLQY), ultraviolet-visible-near-infrared absorption spectroscopy (UV-Vis), Fourier-transform infrared spectroscopy (FT-IR), X-ray diffraction analysis (XRD), X-ray photoelectron spectroscopy (XPS), grazing-incidence wide-angle X-ray scattering (GI-WAXs), transient absorption spectroscopy (TAS), and transmission electron microscopy (TEM).

In the Chapter 3, we introduce an in-situ synthesis strategy for all-CQD $CsPbBr_3$–PbS heterostructures at room temperature and demonstrate their potential in short-wave infrared imaging. The synthesis of all-CQD $CsPbBr_3$–PbS heterostructures is realized by introducing Cs-DOPA (diisooctylphosphinic acid) into the TOPO-$PbBr_2$ (trioctylphosphine oxide) system, sparking a burst nucleation and slow maturation process, followed by the introduction of trimethylsulfonium sulfide ($(TMS)_2S$) to trigger in situ heterostructure formation. Various analyses, including transmission electron microscopy (TEM), X-ray diffraction (XRD), and X-ray photoelectron spectroscopy (XPS), were utilized to confirm the successful formation of all-CQD $CsPbBr_3$–PbS heterostructures. Using time-resolved photoluminescence (TRPL) spectra and transient absorption spectroscopy (TAS), we demonstrate that ultrafast interdot carrier injection initiation time (<1 ps) from the perovskite QDs to the PbS QDs occurs in the heterostructures. Furthermore, our all-CQD $CsPbBr_3$–PbS heterostructures demonstrated tunable and enduring dual emission in both the visible and infrared spectra under ambient conditions, even withstanding over 180 h of continuous solar illumination. The fluorescence properties of all-CQD $CsPbBr_3$–PbS heterostructures can be conveniently tuned by adjusting the Pb/S molar ratio from 1:1 to 1:30 (for $CsPbBr_3$: 505–471 nm; for PbS: 950–1156 nm). Utilizing our low-cost processing of all-CQD heterostructures, we made the first attempt to explore its application in short-wave infrared imaging (SWIR: wavelength range from 1000 to 2000 nm) and attained a higher resolution compared to pure PbS QDs at a low response

threshold of 18 mW/cm^2 (under 365 nm Excitation), which coming within reach of the International Electrotechnical Commission's (IEC) safety threshold (10 mW/cm^2).Our research sheds light on an innovative route to construct controllable and low-cost processing QD heterostructures capable of ultrafast charge transfer, thereby paving the way for their future applications.

In the Chapter 4, we present the pioneering synthesis of thermodynamically controlled, solution-processed, room-temperature in situ epitaxial growth of 2D-3D PMA_2PbBr_4-$CsPbBr_3$ nanocrystal horizontally heterojunctions. The heterojunctions were synthesized by swiftly injecting precursor solutions of CsBr, $PbBr_2$, PMA (phenylmethylamine), and BA (benzoic acid) dissolved in a good solvent into a poor solvent. During the maturation process, $CsPbBr_3$ nanocrystals induce the binding of free PMA^+ and lead bromide ions in the solution, triggering the in-situ growth of thermodynamically stable PMA_2PbBr_4 on the surface of $CsPbBr_3$. The outcome is the direct connection of $[PbBr_4]^{6-}$ octahedra of the two components, avoiding the insulating organic cations' hindrance. The successful synthesis of 2D-3D PMA_2PbBr_4-$CsPbBr_3$ nanocrystal horizontally heterojunctions were confirmed using various analytical techniques such as STEM, X-ray diffraction (XRD), GI-WAXS, and X-ray photoelectron spectroscopy (XPS). First-principles density functional theory (DFT) calculations theoretically support the conclusion that the heterojunction formation is thermodynamically controlled. Temperature-dependent fluorescence spectra reveal strong chemical bonding at the interface, introducing significant lattice distortion in PMA_2PbBr_4. Furthermore, through time-resolved photoluminescence spectroscopy (TRPL) and TAS, we demonstrate the ultrafast charge carrier transfer within the heterostructures.

In the Chapter 5, we summarize the research content and conclusions of this thesis, and provide insights into the future directions and applications based on perovskite nanocrystal heterojunctions.

Table of Contents

Chapter 1 Introduction

This thesis predominantly delves into the in-situ synthesis chemistry and photophysical properties of heterostructures based on perovskite nanocrystals. To elucidate the significance of this study and provide a better understanding of the topic, the author offers essential research background in this chapter. Specifically, Section 1.1 expounds upon the discovery and development of quantum dots, their characteristics, synthesis, and classification, with a focal point on PbS quantum dots. Section 1.2 discusses the emerging field of perovskite nanocrystals, highlighting their exceptional optoelectronic properties, synthesis, and classification, with special emphasis on $CsPbBr_3$ nanocrystals and two-dimensional heterojunctions. Section 1.3 provides a detailed exposition on the synthesis, structure, properties, and applications of heterojunctions based on perovskite nanocrystals. Section 1.4 outlines the purpose and motivation of the study, while Section 1.5 provides an overview of the research content and its innovativeness. Finally, Section 1.6 presents the outline of the paper.

1.1 Quantum dots

1.1.1 What are quantum dots

Now, it is well-known that Moungi G. Bawendi, Louis E. Brus, and Alexei I. Ekimov were awarded the Nobel Prize in Chemistry for their research on quantum dots. Quantum dots have once again captured the public's attention. But what exactly are quantum dots According to scientific definitions, when the radius of semiconductor nanocrystals of a certain element or compound is smaller than or close to the exciton Bohr radius of that element or compound, they are considered quantum dots. From this definition, we can understand that quantum dots can also be referred to as nanocrystals. Quantum dots are confined in three dimensions, and their initial discovery took place in volume-confined glasses.

As depicted in Figure 1-1 (a, b), people in medieval times already utilized the different colors formed by quantum dots of various sizes in glass to decorate doors and windows. However, at that time, people were unaware that the rich and beautiful colors were partly caused by the quantum size effect of metal oxides and semiconductor nanoparticles. The manufacturing methods were empirical, lacking scientific exploration. It wasn't until 1937 that physicist Herbert Fröhlich theoretically predicted that materials would exhibit entirely different properties when their size is reduced to the nanoscale[1]. Subsequently, in 1937, the German company Schoot used colored glass as a filter, also known as Schoot glass (Figure 1-1 c, d).

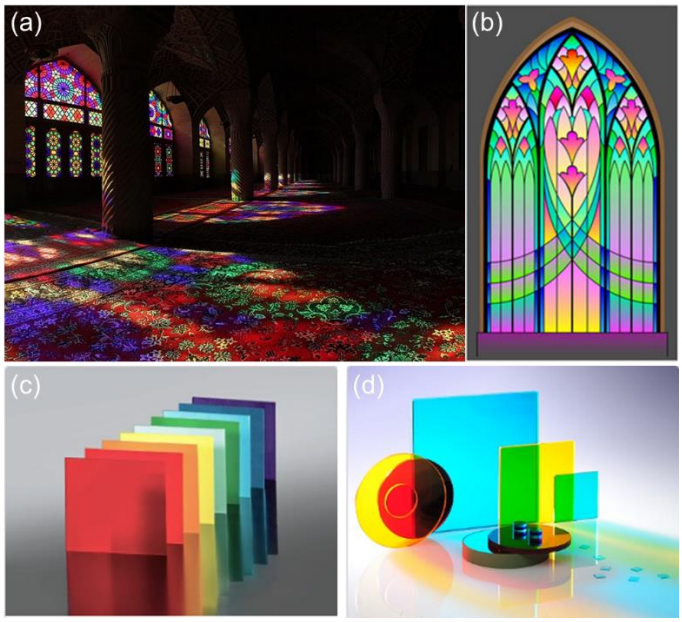

Figure 1-1. (a, b) Different colors formed by quantum dots of various sizes in glass. (c, d) Colorful Schoot glass.

In 1979, while working at the Moscow State Institute of Optics, Alexei I. Ekimov conducted continuous research on the preparation process of Schoot glass and its rich colors. Deliberately adding only CuCl compound to the glass matrix, he heated it to 700°C and annealed for 1 hour. As shown in Figure 1-2 (a), the absorption spectrum measured at a low temperature of 4.2 K exhibits a distinct signal of CuCl crystals (red line 1). In contrast, the pure glass matrix shows no apparent absorption signal (blue line 2). However, this clear absorption signal almost coincides with the absorption peak position of bulk CuCl material, indicating that the size of CuCl crystals in the glass is not effectively controlled. Subsequent research, however, revealed that the size of CuCl crystals in the glass could be effectively controlled by annealing temperature and duration, resulting in a significant blue shift in the absorption spectrum[2]. Ekimov and his collaborators further explored the relationship between the blue shift caused by size

effects and annealing temperature and duration. Specifically, they heated a series of samples to 500-700°C, with annealing times ranging from 1 to 96 hours. After cooling, glasses of different colors were obtained. Small-angle X-ray scattering analysis was conducted to determine their average size a (17-310 Å). To further theoretically understand the relationship between these factors and the final size, Ekimov and his collaborators introduced the concept of Ostwald ripening, suggesting that nucleation and growth are controlled by the diffusion coefficient[3]. Ultimately, they derived the relationship between the average size a and annealing time t and annealing temperature T as shown in Equation 1-1:

$$a = \left(\frac{4\alpha\left(D_0 \exp\left(-\frac{\Delta E}{kT}\right)\right)t}{9}\right)^{1/3} \qquad 1\text{-}1$$

Here, α represents the surface energy, D is the diffusion coefficient, and ΔE is the activation energy. As illustrated in Figure 1-2(b, c), this equation fits well with the values obtained in experiments. Subsequently, Ekimov and his collaborators developed methods to optimize the size distribution. They achieved this by employing high-temperature heating and rapid cooling processes, resulting in a final size uniformity of less than 5%[4] (Figure 1-2 d).

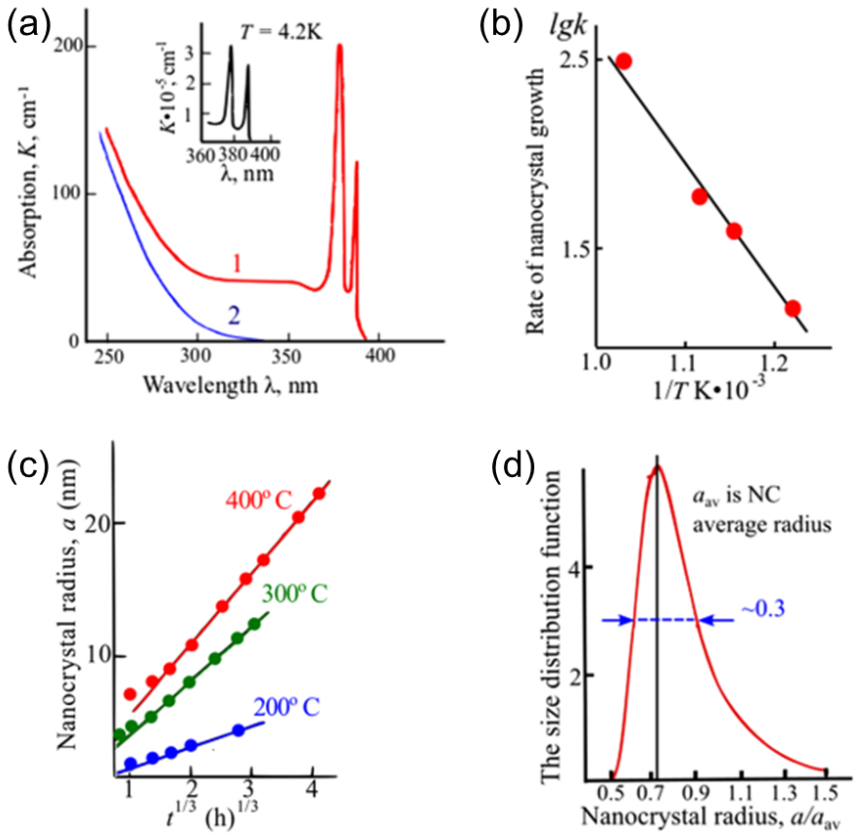

Figure 1-2. (a) Absorption spectrum of CuCl crystals[5]. (b) Rate of NC growth as a function of inverse temperature. (c) Dependence of NC radius on the duration of annealing conducted at three temperatures T = 200, 300, and 400 °C[6]. (d) Universal distribution of NC sizes creating during Ostwald ripening stage of NC growth described by Lifshitz and Slyosov[3].

Ekimov and his collaborators achieved a groundbreaking synthesis of quantum dots in glass, demonstrating their distinctive size effects. Almost concurrently, on the other side of the globe, a group of Western scientists led by Louis E. Brus were actively exploring the synthesis of colloidal quantum dots in solution[7-12]. During a crystalline testing process involving CdS in solution, Brus observed spectral changes over time, astutely attributing them to the size effects inherent in quantum dots. Consequently, by

growing smaller CdS crystals through a reduction in solution temperature, he successfully showcased pronounced quantum size effects. As illustrated in Figure 1-3a, CdS quantum dots obtained at different temperatures exhibited sizes of 12.5 and 4.5 nm. When compared to the larger 12.5 nm quantum dots (depicted by the green line), the absorption spectrum of the smaller 4.5 nm quantum dots displayed a significant blue shift. Subsequently, to elucidate these notable shifts, Brus developed a set of effective mass and dielectric polarization theories[13-14]. He extended and applied these theories to various systems, including CdSe, PbS, ZnS, among others[15-17].

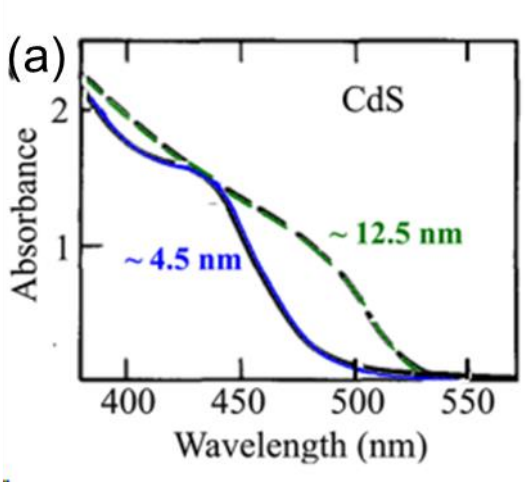

Figure 1-3. (a) Room-temperature absorption spectra of "fresh" and aged for 1 day CdS NC in aqueous solution[13].

Subsequently, in 1986, Dr. Paul Alivisatos, a postdoctoral researcher at Murray Hill, initiated research on the synthesis of colloidal quantum dots in solution. He pioneered the synthesis method now known as the reverse-phase microemulsion. Taking the synthesis of CdS as an example, the Cd source and S source were dissolved separately in water. They were then added to a solution of n-hexane containing a

surfactant, forming a clear and transparent solution. At this stage, micro-sized droplets, or micelles, were formed independently in the solution, serving as microreactors for the synthesis. The next step involved mixing the two solutions. With continuous stirring, the droplets collided and exchanged substances with each other, eventually resulting in the formation of CdS quantum dots. Despite the relative simplicity of the synthesis process and the subsequent development of methods for synthesizing core-shell structured quantum dots, the crystallinity of the quantum dots obtained was poor due to the synthesis being conducted at room temperature, as depicted in Figure 1-4[18].

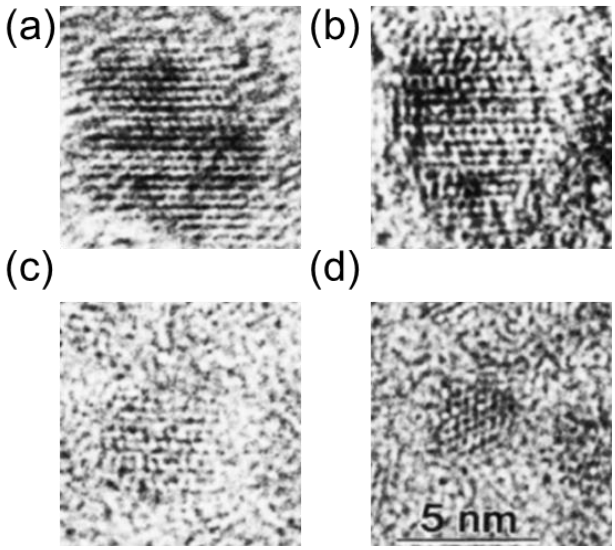

Figure 1-4. TEM images of CdS clusters of different size reveal lattice planes. The bar in panel d corresponds to 50 Å, and the magnification is the same in alt four panels. A statistically large enough sample of such images provides a basis for sizing[18].

The milestone achievement of synthesizing high-quality quantum dots was realized by Moungi G. Bawendi and his collaborators. In 1988, while still at Murray Hill, Bawendi developed Alivisatos's synthesis method further. The quantum dots

synthesized at high temperatures significantly improved their crystallinity. Subsequently, in 1993, Bawendi and his collaborators, now at MIT, introduced the high-temperature thermal injection method that is still in use today. They dissolved Cd and Se sources separately in the solvent system of trioctylphosphine (TOP) and trioctylphosphine oxide (TOPO). Then, at a temperature of 300°C, one of the sources was rapidly injected into the other, causing a rapid burst of nucleation in the mixed solution. Subsequent rapid cooling prevented further nucleation, allowing control over the growth rate[19]. As depicted in Figure 1-5a, by simply controlling the injection temperature, Bawendi and his team could obtain quantum dots ranging in size from 11.5 to 1.2 nm. The absorption spectrum spanned almost the entire visible spectrum. Furthermore, due to the remarkably high uniformity and improved crystallinity of quantum dots (Figure 1-5b, c).

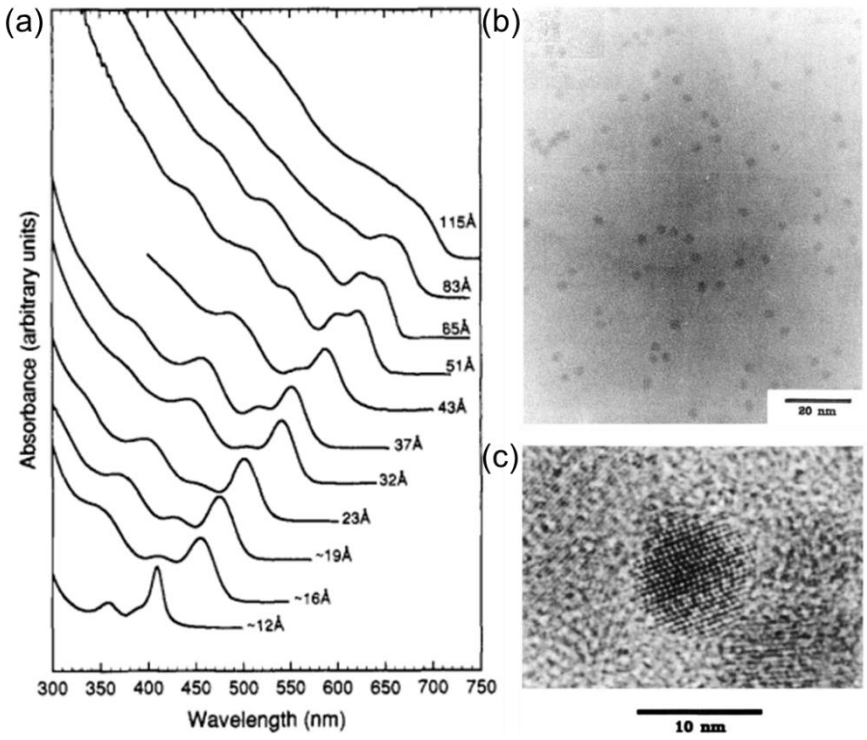

Figure 1-5. (a) Room temperature optical absorption spectra of CdSe nanocrystallites

dispersed in hexane. (b) TEM image taken in bright field with lattice contrast shows a collection of slightly prolateparticles. (c) An 80 Å diameter CdSe crystallite imaged in bright field with atom contrast shows the presence of stacking faults.

At this juncture, quantum dots, as an enchanting and burgeoning nanomaterial, have taken center stage, capturing the attention of scientists worldwide. Countless young researchers continue to tread the path paved by their predecessors in the realm of quantum dots, achieving a series of advancements. In 1996, following the experimental scheme proposed by Bawendi and his colleagues, Hines, Guyot-Sionnest, and others[20-21]developed a core-shell structure, such as CdSe/ZnS, obtaining quantum dots with a photoluminescence quantum yield (PLQY) as high as 50% (Figure 1-6a). The core-shell structure proves to be one of the most effective ways to enhance the luminescence efficiency of quantum dots and passivate defects, as scientists discovered that the blinking frequency of individual core-shell quantum dots is much lower than that of pure quantum dots[22] (Figure 1-6b). Subsequently, chemist adept at controlling quantum dots fabricated superlattices composed of quantum dots, also known as quantum dot superlattices[23-25] (Figure 1-6c). Furthermore, Peng and his colleagues26-28 even manufactured quantum rods (rod-shaped quantum dot structures), ushering in the exploration of shape-controlled quantum dots (Figure 1-6d). Additionally, Alivisatos[26-28]and Norris et al.[29-33]embarked on investigations into the applications of quantum dots in fluorescence bioimaging and the impact of doping on the optical and electronic properties of quantum dots, respectively.

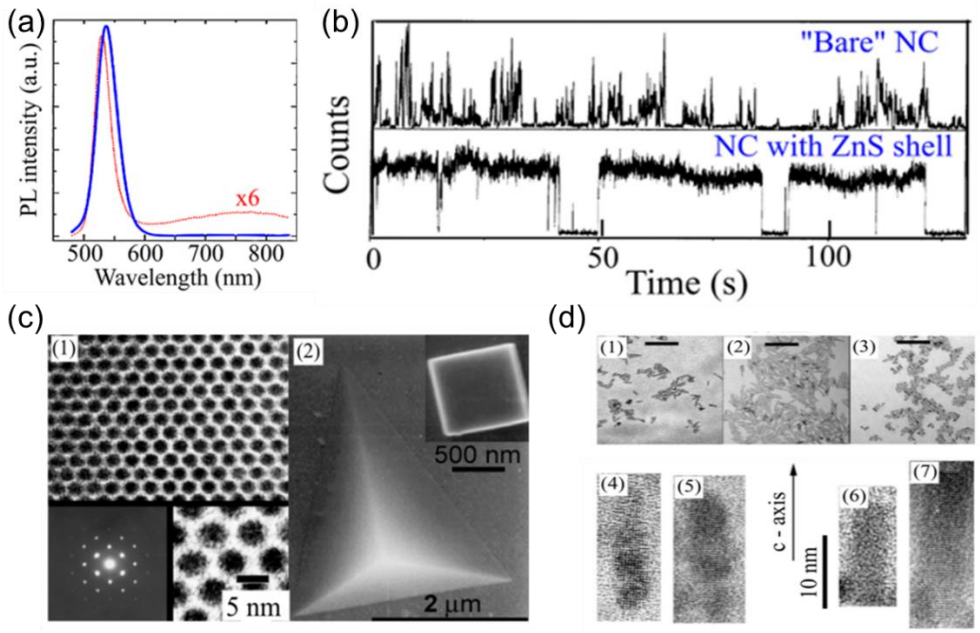

Figure 1-6. (a) Photoluminescence (PL) of CdSe NC passivated by TOPO (dotted line) and CdSe NCs passivated by ZnS (solid line) normalized by their absorption at excitation wavelength (470 nm)[20]. (b) Time dependence of photoluminescence intensity of a single 2.1 nm radius CdSe NCs[22]. (c) (1) A (101) $_{SL}$ projection of an fcc array of 2.4 nm radius NCs with characteristic ED pattern shown in the inset. (2) TEM image of NC solid crystal made of 2.4 nm radius CdSe NCs showing the characteristic pyramidal shape[23]. (d) TEM images of different sample of nanorods. (1−3) Low-resolution of TEM images of three nanorod samples with different sizes and aspect ratios; (4−6) High-resolution TEM images of four nanorods[34].

However, the fervor of quantum dot research cannot overshadow the challenges present in the synthetic schemes proposed by Bawendi and his colleagues: (1) the expensive, toxic, and flammable nature of organometallic sources, and (2) the impact of coordinating solvents such as TOP and TOPO on quantum dots. These challenges

were illuminated at the dawn of the 21st century when Peng and his collaborators[35-39] introduced a new era. They replaced TOP and TOPO with non-coordinating solvent 1-octadecene (ODE), employed inexpensive and stable metal oxides as metal sources, and used long-chain oleic acid (OAc) and oleylamine (OAm) as ligands to synthesize a series of high-quality quantum dots. The universal applicability of the high-temperature thermal injection method was eventually established. Since then, research on quantum dots based on this method has been conducted in nanolabs worldwide, and to this day, there have been no significant modifications to this established approach.

1.1.2 Characteristics of quantum dots

1.1.2.1 Quantum size effect

In the previous discussion on the development history of quantum dots, the term "quantum size effect" or "quantum confinement effect" has been mentioned several times. This effect, which can directly impact the optical properties of quantum dots, is most visibly manifested through changes in size. As illustrated in Figure 1-7, for a specific bulk semiconductor material, the states within its conduction and valence bands are continuous, and the energy gap between bands is minimized. As the size decreases, the energy levels near the band edges become discrete, and the energy gap between bands gradually increases, although levels far from the band edges remain continuous. When the size continues to decrease, the most discrete energy levels are referred to as HOMO (highest occupied molecular orbital) and LUMO (lowest unoccupied molecular orbital). The transition from bulk materials to quantum dots and then to clusters with

only a few atoms results in a gradual increase in the bandgap and the discrete nature of energy levels, a phenomenon known as the quantum size effect.

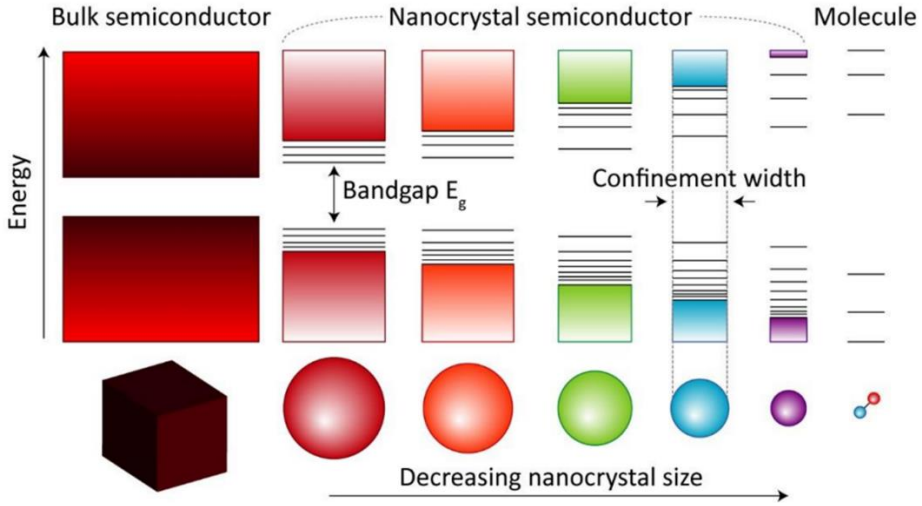

Figure 1-6. Quantum confinement effect. Comparison of bulk, NCs and molecules, indicating the size dependent bandgap of NCs and the formation of discrete states near the band edge.

From the vantage point of excitons, a more profound elucidation of quantum size effects can be achieved. It is widely acknowledged that excitons emerge from the binding of electron-hole pairs due to Coulombic interactions. One may approximate excitons as spherical entities, thereby ascribing to them a radius denoted as a_0. This characteristic can be encapsulated through the following equation (1-2):

$$E_{excition\ Bohr\ radius}(a_0) = \frac{\hbar^2 \mathcal{E}}{e^2}\left(\frac{1}{m_e^*} + \frac{1}{m_h^*}\right) \qquad 1\text{-}2$$

From equation 1-2, it becomes evident that the excitonic Bohr radius a_0 is contingent upon the effective masses of the electron (m_e^*) and hole (m_h^*). These physical quantities, in turn, vary with different semiconductor materials. When the dimensions of the semiconductor material exceed a_0, excitons can move freely within the

semiconductor. Conversely, as the dimensions approach a_0, excitons encounter constraints, impeding their unrestricted mobility. In cases where dimensions fall below a_0, severe limitations ensue, accompanied by an escalation in energy. This phenomenon mirrors the behavior of particles experiencing heightened energy within confined spaces as dimensions diminish. The aforementioned behaviors of quantum dots resembling spherical entities can be aptly expounded using the Box Particle Model, encapsulated in the Brus equation (equation 1-3):

$$E_{QD} = E_{gap} + \frac{h^2}{8r^2}\left(\frac{1}{m_e^*} + \frac{1}{m_h^*}\right) \qquad 1\text{-}3$$

From the above equation, we discern that the band gap of quantum dots increases as the size diminishes. The manifestation of confinement effects, however, hinges on the composition of the semiconductor material. In the case of PbTe with an average size of 16 nm, possessing a_0 of 104 nm, pronounced quantum size effects are exhibited. Conversely, for $CsPbBr_3$ of the same size, the absence of size effects is observed, attributed to its a_0 measuring 5 nm[40-41]. Beyond this, quantum dots exhibit three-dimensional confinement, with Density of States (DOS) appearing at specific locations (Figure 1-8 d)[42]. In contrast, the DOS of bulk materials is continuous, and the band structure is proportional to the square root of energy ($E^{\frac{1}{2}}$) (Figure 1-8 a). In the realm of one-dimensional confined quantum wells, DOS assumes a stepped structure, with a constant relationship between band and energy; although all energies are accessible, they increase only in quantized increments (Figure 1-8 b). As for two-dimensional confined quantum wires, the band is inversely proportional to the square root of energy ($E^{-\frac{1}{2}}$), increasing in quantized steps, rapidly diminishing between two quantization steps

(Figure 1-8 c).

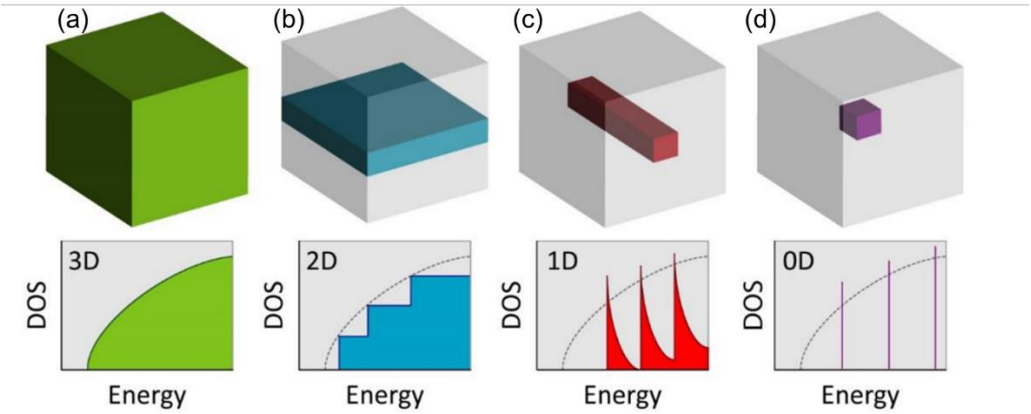

Figure 1-8. Effect of dimensional confinement on the density of states. (a) bulk(3D) with continues DOS, (b)quantum wells with a step-like DOS, (c)quantum wire(1D) with a saw-tooth dependent DOS and(d)Quantum dots (OD)with only discrete sates available.

1.1.2.2 Small size effect

When the size of quantum dots approaches or falls below the wavelength of light or the de Broglie wavelength, the crystalline periodic boundary conditions are disrupted. In the case of non-crystalline particles, a phenomenon known as the small size effect occurs, characterized by a reduction in atomic density near the particle's surface. This leads to significant alterations in properties such as optics, acoustics, magnetism, heat, and mechanics compared to bulk materials. For instance, conventional metallic bulk materials typically exhibit a metallic luster. However, when reduced to the nanoscale, they lose their metallic sheen and transform into black powder with a reflectance below 1%. Paradoxically, they demonstrate excellent absorption of sunlight, making them promising materials for high-efficiency photovoltaic conversion and stealth

applications. Similarly, ceramic materials, known for their brittleness at larger scales, acquire enhanced toughness at the nanoscale due to the presence of larger interfaces. The arrangement of atoms between these interfaces becomes highly disordered, facilitating atomic migration under external forces and imparting significant toughness. Moreover, the small size effect of particles is evident in various aspects, including superconducting behavior, dielectric properties, acoustic characteristics, and chemical reactivity.

1.1.2.3 Surface effect

The surface area of spherical particles is directly proportional to the square of their diameter, while their volume is directly proportional to the cube of the diameter. Consequently, the specific surface area (surface area/volume) is inversely proportional to the diameter. As the particle diameter decreases, the specific surface area significantly increases, indicating a substantial increase in the percentage of surface atoms. Surface effects for particles with diameters greater than 0.1 μm can be negligibly small. However, when the size is less than 0.1 μm, the specific surface area experiences a sharp rise, and surface effects become non-negligible. The heightened specific surface area results in an insufficient coordination of surface atoms, with the presence of numerous dangling bonds, leading to a rapid increase in surface energy. This abundance of uncoordinated atoms and surface dangling bonds imparts a high level of reactivity to surface atoms, rendering them highly unstable and prone to bonding with other atoms. The surface of ultrafine particles differs significantly from that of large bulk objects.

Under real-time observation with a high-magnification electron microscope, these particles exhibit no fixed shape. Over time, they spontaneously form various shapes such as cubes, octahedra, dodecahedra, etc. This behavior sets them apart from typical solids and liquids, representing a quasi-solid state. Under electron beam irradiation in an electron microscope, the surface atoms seem to enter a state of "boiling." The instability in the particle structure is not observable until the size exceeds 10 nm, at which point nanocrystals attain a stable structural state.

1.1.2.4 Quantum tunneling effect

As illustrated in Figure 1-9, within the realm of quantum mechanics, the Quantum Tunneling Effect refers to the quantum behavior where microscopic particles, such as electrons, can penetrate or traverse potential barriers, even when the height of the barrier exceeds the total energy of the particle[43]. In classical mechanics, particles can overcome a barrier only if their kinetic energy surpasses the barrier's potential. Particles with energy less than the barrier would be reflected. In quantum mechanics, owing to the wave-particle duality of particles, there exists a probability for particles with energy less than the barrier to tunnel through. This phenomenon is known as the Quantum Tunneling Effect. The probability of quantum tunneling is correlated with the height and width of the potential barrier, as well as the effective mass of the particle.

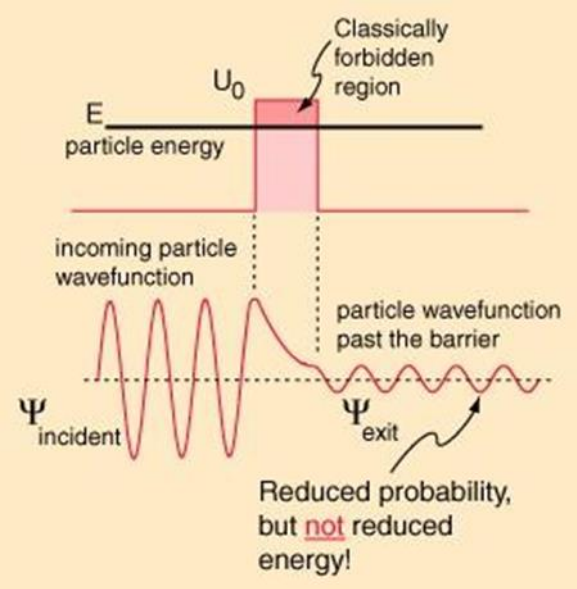

Figure 1-9. Schematic of Quantum tunneling effect.

1.1.3 Synthesis and classification of quantum dots

1.1.3.1 Understanding the nucleation and growth

Before delving into the synthesis of quantum dots, it is imperative to acquaint ourselves with the principles governing their nucleation and growth. As previously mentioned, the synthesis of quantum dots involves a burst of nucleation followed by controlled growth. As depicted in Figure 1-10, the precursor molecules undergo a phase transition to form monomers initially (Stage I). Subsequently, a multitude of monomers triggers nucleation, leading to a simultaneous decline in monomer concentration. When the diminishing monomer concentration no longer meets the nucleation conditions, the second stage terminates. Crystal nuclei, acting as templates for nanocrystal formation, continue to grow by consuming monomers. As monomer concentration approaches depletion, further growth is achieved through Ostwald ripening, a process involving the

dissolution of smaller quantum dots to facilitate the growth of larger ones (Stage III). These stages can be precisely controlled through the modulation of surface ligands, which concurrently contribute to the stability of quantum dots.

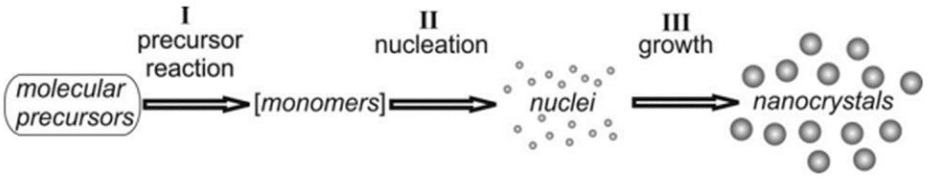

Figure 1-10. Illustration of the three key steps in the synthesis of colloidal NCs: precursor-to- monomer conversion, homogeneous nucleation, and heterogeneous growth.

To achieve uniformly dispersed quantum dots, it is often necessary to separate nucleation from growth, requiring a sufficiently rapid nucleation rate. As depicted in Figure 1-11, La Mer and others proposed the concept of burst nucleation, suggesting a connection to the rapid nucleation that occurs when monomer concentration exceeds a certain threshold[44-47]. A prerequisite for rapid nucleation is the exceptionally high reactivity of the precursor. Within the framework of classical nucleation theory, the nucleation rate $\frac{dN}{dt}$ can be described by the following equation (1-4) [48]:

$$\frac{dN}{dt} = Aexp\left(-\frac{\Delta G^N}{RT}\right) \qquad 1\text{-}4$$

In this equation, $\Delta G^N = \frac{16\pi\gamma^3 V_m^2}{3(RTlnS)^2}$ represents the activation free energy, where γ is the surface tension, V_m is the molar volume, S is the supersaturation. Supersaturation is defined as the ratio of monomer concentration to the solubility of the material in bulk ($S = \frac{Monomer}{C^o_{buik}}$). Therefore, at a given temperature, the precursor must be rapidly converted into monomers within a short time frame (0.1-10 seconds). Furthermore, if

the initial accumulation of monomers is slow, indicating a lack of burst nucleation, the separation of nucleation and growth stages can be achieved by carefully heating the reaction mixture steadily[49]. Typically, high-boiling-point solvents are employed to provide a broad reaction temperature range of 25–350 °C. One notable example is Oleylamine (ODE), as mentioned earlier.

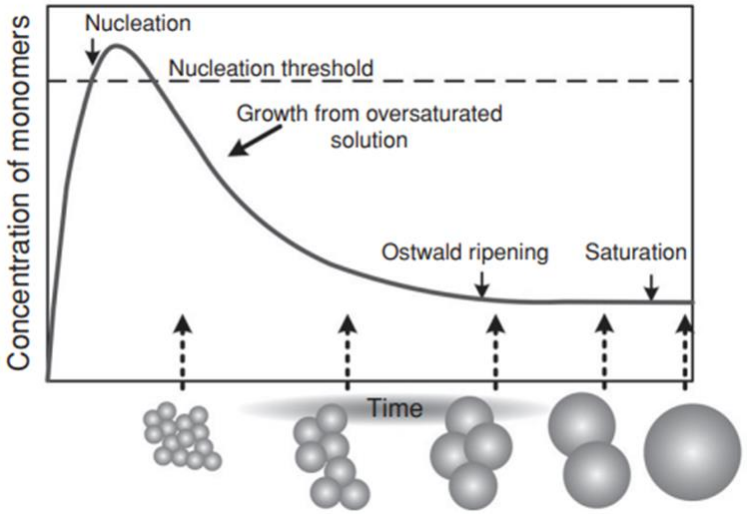

Figure 1-11. Schematics of the main stages in the synthesis of colloidal NCs in relation to the concentration of the monomers.

As previously discussed, the transition from precursor to monomer marks the initial step in nucleation. The occurrence of this phase transition is contingent upon the Gibbs free energy (ΔG) of the entire system:

$$\Delta G = \Delta H - T\Delta S \qquad 1\text{-}5$$

where ΔH denotes enthalpy, T signifies temperature, and ΔS represents the system's entropy, a pivotal criterion arises when the entropy change in the system's free energy surpasses the enthalpy alteration, denoted by $\Delta G < 0$. Under such conditions,

a phase transition transpires uniformly across the entire parent phase or at nucleation sites—localized regions such as structural impurities or container edges. Primarily, let us delve into nucleation transpiring uniformly within the parent phase, a phenomenon aptly termed homogeneous nucleation. In the context of solidification transitions, such as the formation of nanoscale particles in a solution, the free energy ΔG comprises two distinct components. The first component is the volumetric free energy, denoted as ΔG_v, encapsulating the disparity between the solid and liquid phases. The second component is the interfacial or surface free energy, denoted as γ[50], representing the energy required to extend the solid-liquid interface during the solidification process. For a spherical particle with a radius r, the comprehensive expression for ΔG can be articulated as:

$$\Delta G = \frac{4}{3}\pi r^3 \Delta G_v + 4\pi r^2 \gamma \qquad 1\text{-}6$$

Given that $\Delta G_v < 0$ and $\gamma > 0$, the stability of a nucleus and its potential for growth are fundamentally governed by ΔG_v (refer to Figure 1-12). Stability is attained at the critical radius, denoted as r_c, where ΔG achieves its maximum value (calculated by identifying the value of r for which $\frac{d}{dr}\Delta G = 0$). Assuming ΔG_v and γ are constants independent of r, the expression becomes:

$$\frac{d}{dr}\Delta G = \frac{4}{3}\pi r^3 \Delta G_v + 4\pi r^2 \gamma = 0 \qquad 1\text{-}7$$

By solving for r, we can obtain the critical radius r_c:

$$r = -\frac{2\gamma}{\Delta G_v} r_c \qquad 1\text{-}8$$

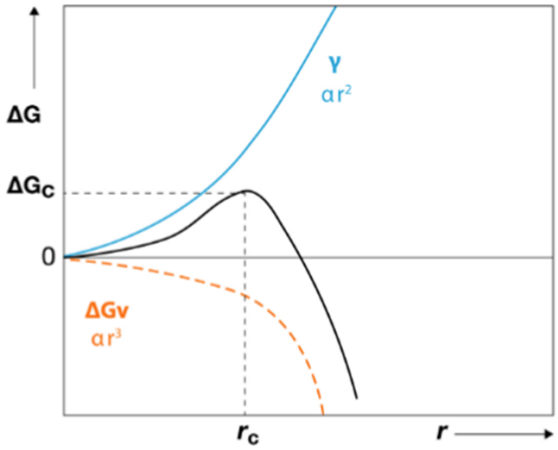

Figure 1-12. The contribution of volume free energy(red):and surface free energy (blue)to the total free energy change (black) as a function of nucleus size. The critical radius r_c indicates the minimum size for which the nuclei are stable enough to proceed to growth.

Now, let us consider the scenario where nucleation occurs at specific sites, termed heterogeneous nucleation. These nucleation sites could be impurities within the reaction, the edges of the container, or even bubbles—essentially, any phase different from the parent phase. When nucleation events transpire at such sites, the contact angle between the nucleus and the site decreases, leading to a reduction in surface area compared to homogeneous nucleation. This reduction in surface energy, denoted as γ, makes the volumetric free energy ΔG_v the dominant factor, thereby lowering the maximum value of ΔG_v (refer to Figure 1-13). Post-nucleation, growth occurs as monomers diffuse to the surface of the nucleus, where subsequent reactions transpire. This diffusion process is aptly described by Fick's laws[51-52]. Consider the monomer concentration, C, at a distance x from the center of the particle. At the surface of the nanoscale particle where $x = r$, $C = C_s$, and in the bulk phase where $x = r + \delta$, $C = C_b$.

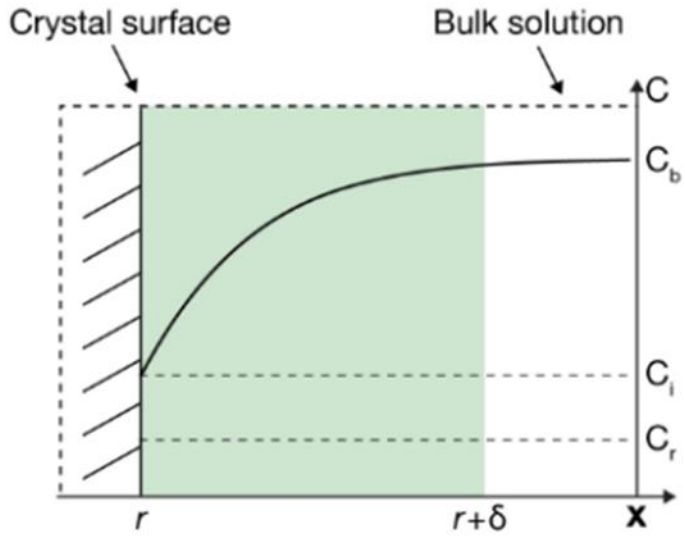

Figure 1-13. Diffusion layer structure near the surface of a nanocrystal is shown on the left side, and a plot for the monomer concentration as a function of distance x is shown on the right side.

In accordance with Fick's law, the flux of a monomer can be expressed by the following equation:

$$J = 4\pi x^2 D \frac{dC}{dx} \qquad 1\text{-}9$$

Here, D represents the diffusion coefficient, independent of x. Therefore, by integrating equation 1-9 between r and $r + \delta$, we obtain:

$$J = \frac{4\pi D r(r+\delta)}{\delta}(C_b - C_s) \qquad 1\text{-}10$$

Assuming a first-order reaction occurs at the surface, equation 1-10 can also be expressed as:

$$J = 4\pi r^2 k(C_s - C_r) \qquad 1\text{-}11$$

Here, k denotes the rate constant, and C_r is the particle's solubility, dependent on

particle size. Combining equations 1-9 and 1-10, we can ascertain whether the growth of quantum dots is diffusion-controlled or reaction-controlled, as indicated in equation 1-12:

$$\frac{C_s - C_r}{C_b - C_s} = \frac{D}{kr}\left(1 + \frac{r}{\delta}\right) \qquad 1\text{-}12$$

When $D \ll kr$, $C_s \approx C_r$, signifying diffusion-controlled growth. Conversely, when $D \gg kr$, $C_b \approx C_s$, indicating reaction-controlled growth. LaMer and colleagues proposed a universal model for comprehending nucleation and growth[52], as per their model, nucleation and growth can be delineated into three stages:

1. The precursor concentration undergoes a rapid increase until reaching a critical concentration, triggering supersaturation;
2. Nucleation initiates and continues until the precursor concentration drops below the critical level;
3. Controlled growth ensues over time until monomers are depleted.

It is essential to emphasize our objective of minimizing the particle size distribution to ensure the uniformity of optical properties. This can be achieved by maintaining a sufficiently high monomer concentration in the growth solution. Ensuring a high monomer concentration allows the formation of numerous rapidly growing small particles, resulting in a uniformly dispersed batch. Stopping the reaction after a certain duration can also provide monodisperse batches[47]. Typically, lower temperatures and lower precursor concentrations result in fewer nuclei, coupled with an extended reaction time, leading to larger particle sizes and broader size distributions. In the synthesis process without optimization, colloidal nanocrystals may undergo

uncontrolled growth through a phenomenon known as Ostwald ripening. The nomenclature of this mechanism derives from the chemist who first observed this phenomenon. In this growth mechanism, smaller particles with higher surface energy dissolve, releasing monomers that are absorbed by larger particles[47]. This process causes the size distribution of the synthesis batch to widen or diverge.

1.1.3.2 Synthesis of quantum dots

As illustrated in Figure 1-14, since the discovery of quantum dots, various methods have evolved. In addition to molecular beam epitaxy (MBE) and chemical vapor deposition (CVD), which require substrate support, the production of monodisperse quantum dots primarily involves both bottom-up and top-down approaches. The top-down approach can be achieved through mechanical means (such as ball milling) or chemical methods (photolithography, exfoliation, etching, etc.). Bottom-up assembly starts from molecules, atoms, and ions, progressing through gas or liquid-phase chemical reactions, aggregation, and crystallization. Liquid-phase synthesis in aqueous or non-aqueous solvents (wet chemical methods) is particularly convenient and successful, and it is the focus of detailed discussion in this paper.

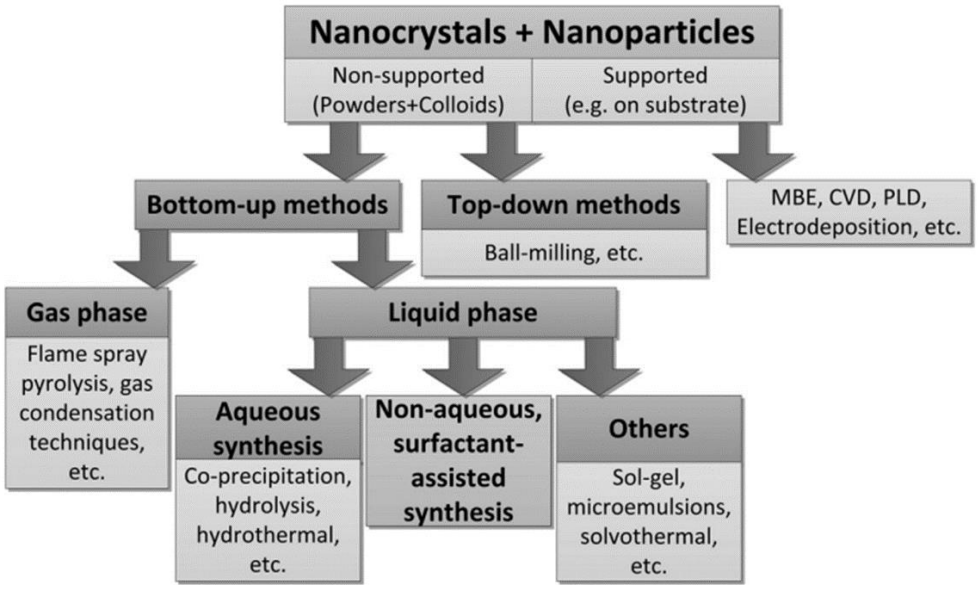

Figure 1-14. An overview of various methods for fabrication of inorganic nanoparticles and nanocrystals.

The most widely used method is commonly referred to as the "hot injection method." The synthesis apparatus for hot injection is illustrated in Figure 1-15. Taking the synthesis of Cd as an example, $Cd(CH_3)_2$ reacts with a compound such as bis(tri-methylsilyl) sulfide or trialkylphosphine sulfide at elevated temperatures[53]. At room temperature, Group II and VI precursor solutions are mixed in a high-boiling, weakly coordinating solvent, such as trioctylphosphine (TOP), and swiftly injected into a reaction vessel containing a high-boiling, strongly coordinating solvent, such as trioctylphosphine oxide (TOPO). The system is then heated to 200-350°C under an inert atmosphere [19, 54]. Although the reaction rates of these precursors in viscous, coordinating trialkylphosphine are slow at room temperature, or even non-existent, injecting them into a heated vessel rapidly elevates the precursor solution temperature, inducing the generation of monomer species. Monomer concentration rapidly surpasses

supersaturation and is relieved through nucleation processes. Injection reduces the temperature of the vessel, slowing down the decomposition of precursors and the formation of monomers. Within less than a minute, the nucleation stage concludes, and the colloid enters the growth stage. Around 10-30 minutes later, Ostwald ripening becomes significant. However, a prevalent drawback of the initial hot injection method is its complex dependence on variables such as injection rate, mixing rate, and small temperature fluctuations for the initial nucleation distribution. This poses a challenge when aiming for reproducibility of specific sizes in production. Early organic-metal methods were undesirable due to the reactivity (self-flammability) and extreme toxicity of metal alkyl precursors. To address this issue, Peng and colleagues introduced a less toxic, non-volatile II-group CdO precursor, enabling the hot injection synthesis of high-quality quantum dots. In quantum dot synthesis, a significant portion of coordinating TOP−TOPO was replaced with a solvent that is non-coordinating or at least weakly coordinating, such as octadecene (ODE) or mineral oil/paraffin[38, 55-56]. This forms a mixed solvent, and a small amount of coordinating substance is added to further reduce reaction costs and toxicity. Today, the hot injection method is still widely used on a laboratory scale. The primary reason for its continued use is its capability to produce various types of semiconductor quantum dots, including IB−VI group Ag2S and Ag2Se[57-58], II−VI group CdS, CdSe, CdTe, ZnS, ZnSe, and ZnTe[59-61], IV−VI group PbS, PbSe, and PbTe[62-65], as well as III−V group InP and InAs[66-67].

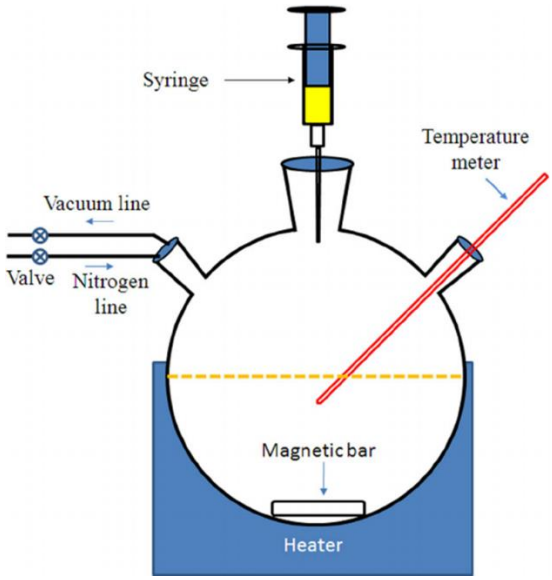

Figure 1-15. Scheme diagram of hot-injection method[68]

As depicted in Figure 1-16, the heating synthesis is another extensively utilized method. This approach relies on favorable conditions of gradually increasing temperature and precursor decomposition kinetics, allowing the in-situ generation of monomers, thereby achieving the time-discrete nucleation emphasized by the LaMer model[47]. Subsequent sustained growth leads to the formation of monodisperse colloids[46, 69]. Comprehensive reviews of the heating synthesis process have been provided by van Embden et al. and Hyeon et al[70-71]. In the heating synthesis method, all reactants are mixed in a reaction vessel and heated at a controlled rate, inducing nucleation and growth. As the temperature of the reaction vessel rises, precursor decomposition forms monomers. Monomers can aggregate and transiently exceed supersaturation, triggering nucleation. Careful balancing of the kinetics of the decomposition reaction and the growth rate on formed nuclei is crucial. The choice of precursors, ligands, and reaction conditions is paramount. Nucleation must be rapid enough to generate a significant

number of nuclei within a relatively short time window, while growth must be slow enough to allow size focusing without returning the monomer concentration to the supersaturation required for induced secondary nucleation. Over time, many synthesis methods initially based on the hot injection approach have been modified to achieve more scalable "heating" methods[72-73] for synthesizing various combinations of metal sulfide and nitride quantum dots[74-76].

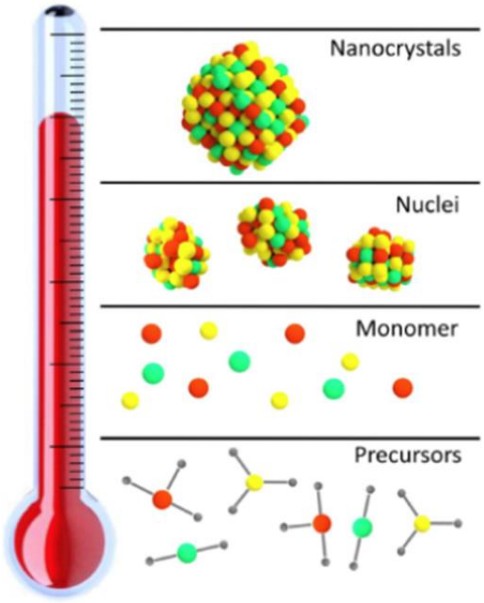

Figure 1-16. Schematic diagram of heat-up method[77]

1.1.3.3 Classification of quantum dots

Figure 1-17 provides an overview of the most prominent and widely studied quantum dots along with their spectral ranges. Depending on the spectral range of quantum dots, they find different applications. For instance, PbS quantum dots, with their suitable bandgap, are primarily used in solar cells and detectors. Similarly, InAs is also used as a detector. In the context of solar cells, the CuInSe2 system is

advantageous due to its non-toxic nature compared to PbS. CdSe quantum dots are mainly utilized in displays because of their wide color gamut, covering almost the entire visible spectrum. However, Cd is a toxic element, leading to extensive research on InP quantum dots as an excellent alternative.

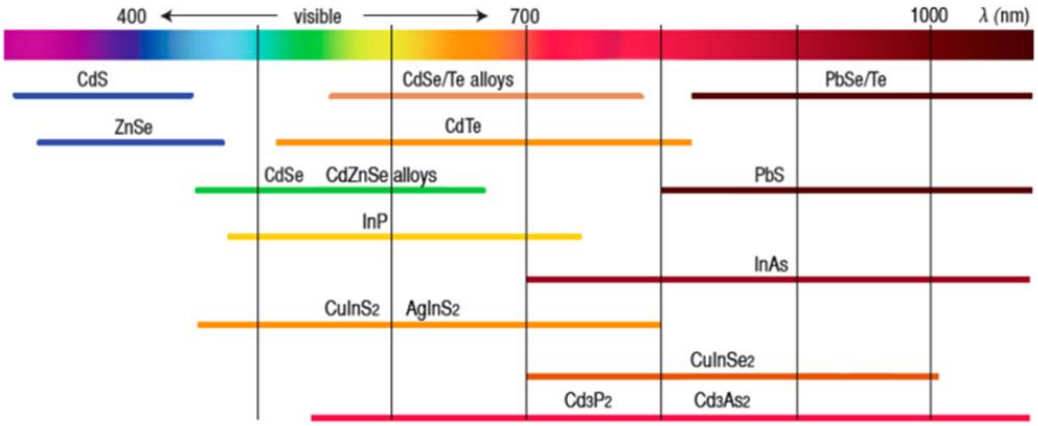

Figure 1-17. Various quantum dots[78].

1.1.4 Lead sulfide quantum dots

PbS quantum dots (QDs) represent a highly significant class within the quantum dot family due to their outstanding stability and tunable bandgap. As illustrated in Figure 1-18a, the Wulff construction results for quantum dots with a given size demonstrate that quantum dots smaller than 2.7 nm consist of an octahedral shape terminated entirely by lead atoms on the (111) crystal plane[79]. As the size increases, truncated (100) crystal planes emerge, and when the size exceeds 4.74 nm, a cubic octahedron particle is formed, comprising eight (111) hexagonal crystal planes and six (100) square crystal planes. Figure 1-18b displays the arrangement of surface atoms for different sizes. Calculations reveal that for sizes larger than 4.74 nm, (111) crystal planes occupy 77.6% of the total surface area, while (100) crystal planes constitute

22.4%.

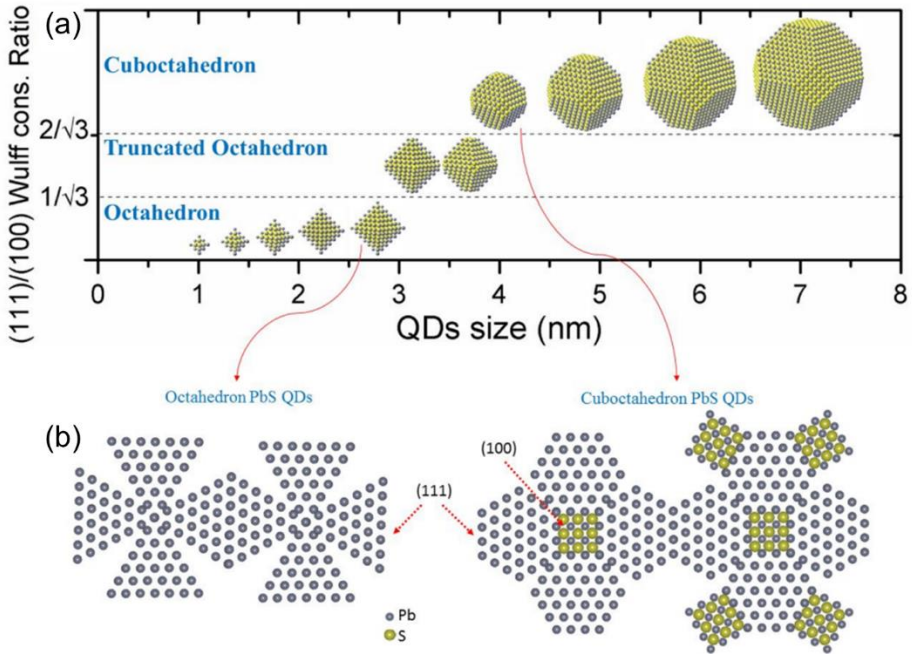

Figure 1-18. (a) Equilibrium shape of 1 to 7.5 nm PbS QDs, (b) arrangement of Pb and S atoms at the surface of octahedron and cuboctahedron PbS quantum dots[79].

In line with the preceding exposition, the current mainstream approach for synthesizing PbS quantum dots remains the thermal injection method, employing oleic acid and oleylamine as ligands (111) crystal facets, terminated by lead atoms, exhibit elevated binding energies with ligands. Consequently, the (111) facets display reduced susceptibility to oxidation and fewer defects. However, this heightened binding also impedes facile ligand exchange, presenting a contrasting scenario for the (100) facets[80]. Hence, achieving precise control over the size of PbS quantum dots emerges as a formidable challenge. As depicted in Figure 1-19 a [81-82], leveraging the pronounced size effects of PbS quantum dots enables the facile tuning of absorbance spectra from near-infrared to mid-infrared by simple adjustments in temperature and other conditions.

This correlates with varying average sizes observed under transmission electron microscopy (Figure 1-19 b-f).

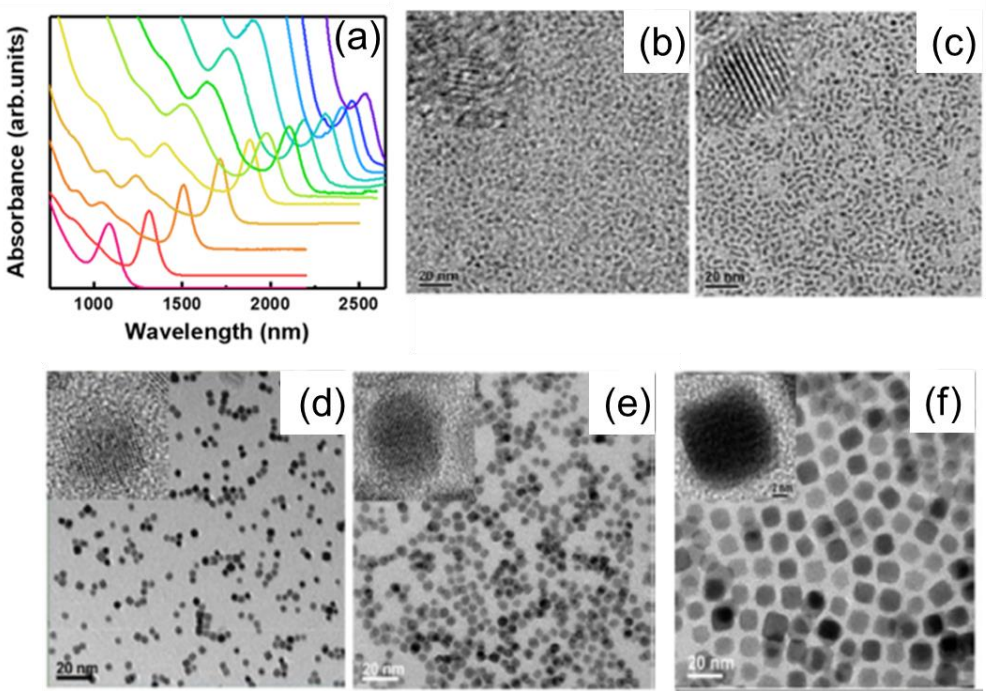

Figure 1-19. (a) Absorbance spectra for QDs sensing from 1100 to 2600 nm[81]. (b-f) Transmission electron microscopy (TEM) images of (a) 2.3, (b) 2.7, (c) 3.5, (d) 5.5, and (e) 10 nm sized PbS NCs synthesized at 110, 120, 130, 150, and 160 ℃ temperatures, respectively. All scale bars are 20 nm[82].

1.2 Perovskite nanocrystals

1.2.1 What are perovskite nanocrystals

Since the discovery of quantum dots, illuminating laboratories worldwide with their brilliance, another captivating nanocrystal has gradually captured the attention of some scientists, destined to draw global scrutiny due to its exceptionally unique properties. This brings us to the intriguing realm of perovskite nanocrystals. Let us direct our focus

to perovskite, a material whose discovery and nomenclature predates that of quantum dots. In 1829, mineralogist Gustav Rose and his associates, during their explorations of mines and deposits in the Ural Mountains, stumbled upon and brought back rock samples. By 1839, upon sharing these samples with colleagues, Rose identified a mineral previously unreported, ultimately naming it "Perovskite" and publicly disclosing its mineral composition as "$CaTiO_3$."

However, this was the initial form of perovskite, and the perovskite now under extensive investigation possesses the structural formula ABX3 (A: Cs^+, FA^+, MA^+; B: Pb^{2+}, Sn^{2+}; X: Cl^-, Br^-, I^-). Crystalline compounds consisting of $CsPbX_3$, $CsPb_2X_5$, and Cs_4PbX_6 were first reported in the 1890s[83]. In the late 1950s, it was discovered that $CsPbX_3$ crystallizes in a perovskite lattice and exhibits photoconductivity[84-85]. The high ionic conductivity in $CsPbX_3$ was reported in the 1980s, attributing to the instability of perovskite materials in photovoltaic devices and the crucial factor enabling rapid ion exchange in nanocrystals[86]. At least by the 1970s, the emission peak at around 2.45 electron volts (506 nanometers) in Pb-doped CsBr single crystals was observed, with the origin traced to the atomic emission of Pb^{2+} centers associated with ns^2 cations under Jahn-Teller splitting. This finding marked a significant milestone in understanding the intricate behavior of perovskite nanocrystals[87].

In the mid-1990s, scientists provided further insights into Pb-doped CsX single crystals grown through the Bridgman or Stockbarger methods and thermally evaporated thin film materials. They proposed the existence of several-nanometer-sized fluorescent clusters related to $CsPbX_3$ in the samples. This could explain the observed phenomenon

where the bright photoluminescence (PL) peak of these clusters is typically higher than that of bulk $CsPbX_3$ due to quantum size effects. For instance, in 1995, the PL at 400-420 nanometers in Pb-doped CsCl single crystals was interpreted as excitonic emission from CsPbCl3 clusters. Similar observations were made in Pb-doped CsBr, indicating the presence of analogous phenomena[88-90].

To intentionally induce and repeatedly form nanosized $CsPbX_3$ within CsX matrices, Pb-doped CsX single crystals or polycrystalline materials grown using the Bridgman or Stockbarger methods must undergo annealing at temperatures between 150 and 300°C for 10-100 hours to nucleate $CsPbX_3$. These annealing temperatures are sufficiently high to induce ion motion and aggregation but still below the melting point of the CsX matrix. Interestingly, distinct PL spectra observed in samples annealed at 210°C and 240°C suggest the possible formation of non-spherical, plate-like $CsPbCl_3$ nanocrystals. From the late 1990s onwards, attention turned to synthesizing phase-pure $CsPbX_3$, often achieved through thermal evaporation with thicknesses reaching several micrometers[91-93]. At 77 K, amorphous deposition of $CsPbBr_3$ thin films followed by heating to room temperature to induce crystallization into nanocrystalline $CsPbBr_3$ films displayed remarkably bright PL excitonic emission with quantum size effects. These films even exhibited stimulated emission under nanosecond pulse excitation at room temperature (0.5 ns, at an average threshold of 0.5 kW /cm^2). These early observations spurred the development of the thermal injection synthesis route for $CsPbX_3$ nanocrystals in early 2015[41]. These nanocrystals were the first in the colloidal nanocrystal series to exhibit bright PL across the entire visible spectrum without the

need for electronic surface modifications. They demonstrated high photoluminescent quantum efficiency (>90%) and narrow full-width at half-maximum (FWHM) of <100 meV (12-42 nm).

Similarly, the history of organic-inorganic hybrid perovskite nanocrystals can be traced back to the late 1970s when the synthesis and crystal structure of $MAPbX_3$ were introduced[94]. The structures and properties of $FAPbBr_3$ and $FAPbI_3$ were only reported in the past decade. Since 2012, researchers have gradually reported on the toluene dispersion of MA-based and other alkylammonium lead halides[95-96]. The colloidal dispersibility of $MAPbBr_3$ nanoparticles was significantly improved by employing an assistant-assisted reprecipitation method in the presence of long-chain ligands, a technique first introduced in 2014[97]. Since 2015, reports have emerged on sheet-like and cubic-shaped $FAPbBr_3$ and $FAPbI_3$ nanocrystals[98-101].

1.2.2 crystal structure of perovskite nanocrystals

As illustrated in Figure 1-20, within the typical cubic-phase crystal structure of perovskite, B-site atoms coordinate with six X atoms, forming an octahedral structure. Every two octahedra share an X atom at their apex. Each A-site cation is surrounded by eight such octahedra, creating a stable cubic structure that extends infinitely in three-dimensional space periodically. However, the standard cubic structure is only realized under specific conditions. Due to the inherent flexibility of the three-dimensional framework of BX_6 octahedra, perovskites are likely to exhibit tetragonal or orthorhombic crystal phases (Figure 1-21a) in certain scenarios[102].

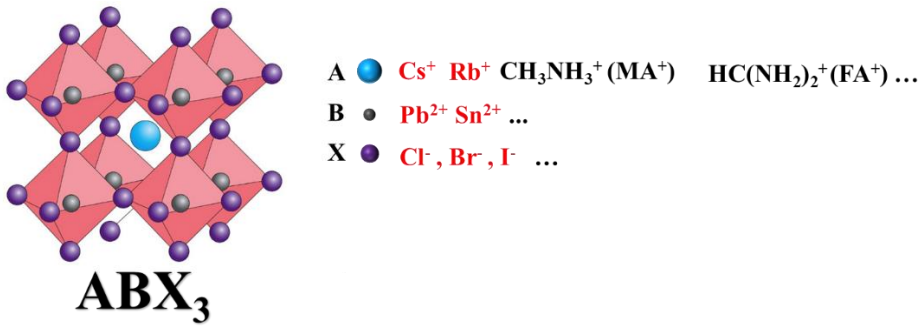

Figure 1-20. Crystal structure of ABX_3 perovskites

The occurrence of these lower-symmetry crystal phases is primarily attributed to variations in the B-X-B bond angles, as depicted in Figure 1-21b. Changes in the X_{eq} direction leads to the tetragonal phase (P4/m), while changes in the X_{ax} direction result in the orthorhombic phase. According to convention, these phases are respectively termed α, β, and γ[103]. At room temperature, the general formula $ABCl_3$ typically exhibits the α phase, while $ABBr_3$ adopts the γ phase. In the case of ABI_3, it assumes a δ phase, which is nearly devoid of fluorescence activity (characterized by edge-sharing octahedra rather than corner-sharing octahedra). As the temperature decreases, the transition from the α phase to phases with lower symmetry gradually occurs[103]. Additionally, distortions in the three-dimensional framework induced by octahedral tilting can lead to crystal splitting into multiple domains and the formation of twin boundaries[104].

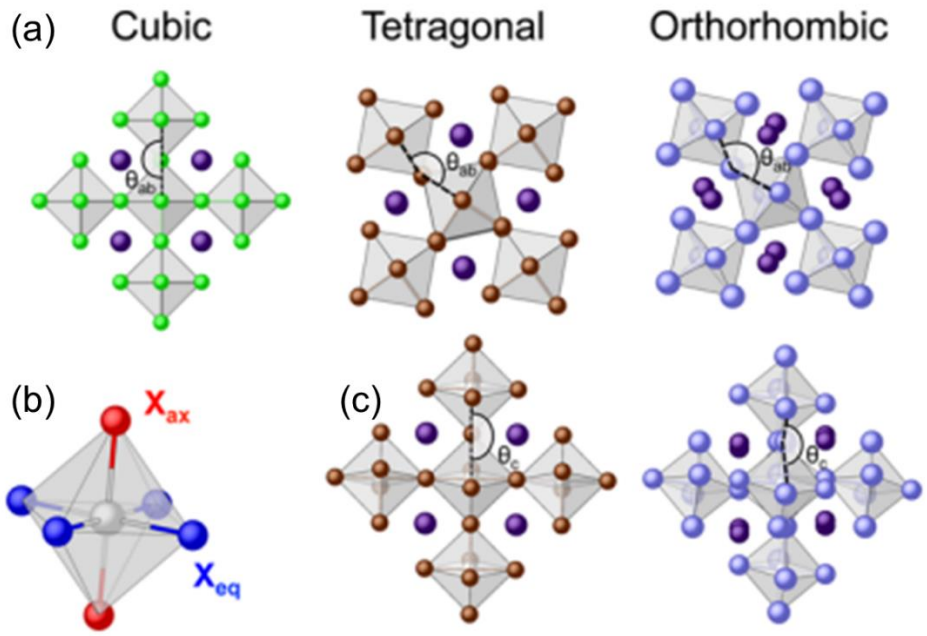

Figure 1-21. Sketch of the 3D arrangement of the PbX_6 octahedra in $CsPbX_3$ perovskites exhibiting a cubic (C), tetragonal (T), or orthorhombic (O) structure[105]

The stability of the perovskite crystal structure is crucial, influencing whether perovskites can successfully transition to commercial applications. Therefore, researchers employ the Goldschmidt tolerance factor (t)[106] to describe the stability of the perovskite crystal structure, as shown in Equation 1-13:

$$t = \frac{r_A + r_X}{\sqrt{2}(r_B + r_x)} \qquad 1\text{-}13$$

Here, r_A, r_B, and r_x are the ionic radii of components A, B, and X atoms, respectively. According to studies, most 3D perovskite structures have Goldschmidt tolerance factor (t) values within the range of 0.8–1. When (t) falls within this range, a stable 3D structure is formed. Structures related to perovskites are typically unstable outside this range. Some perovskite structures at the edges of the tolerance factor range, such as $CsPbI_3$ ($t \approx 0.8$) and $FAPbI_3$ ($t \approx 1$), undergo rapid structural phase transitions

at room temperature, transforming into more stable hexagonal/orthorhombic phases[107]. Another criterion for measuring structural stability is the octahedral factor $\mu = \frac{r_B}{r_X}$, which depends on the radii of B and X ions and typically falls within the range of $0.442 \leq \mu \leq 0.895$[108]. Today, both the octahedral factor and the tolerance factor are widely used to predict and explain the stability of perovskite structures[98, 105, 109]. In addition to the 3D structures mentioned above, perovskites can also be categorized into 2D, 1D, and 0D structures, where the dimensions of the perovskite depend on the corner-sharing arrangement of the BX_6 octahedra.

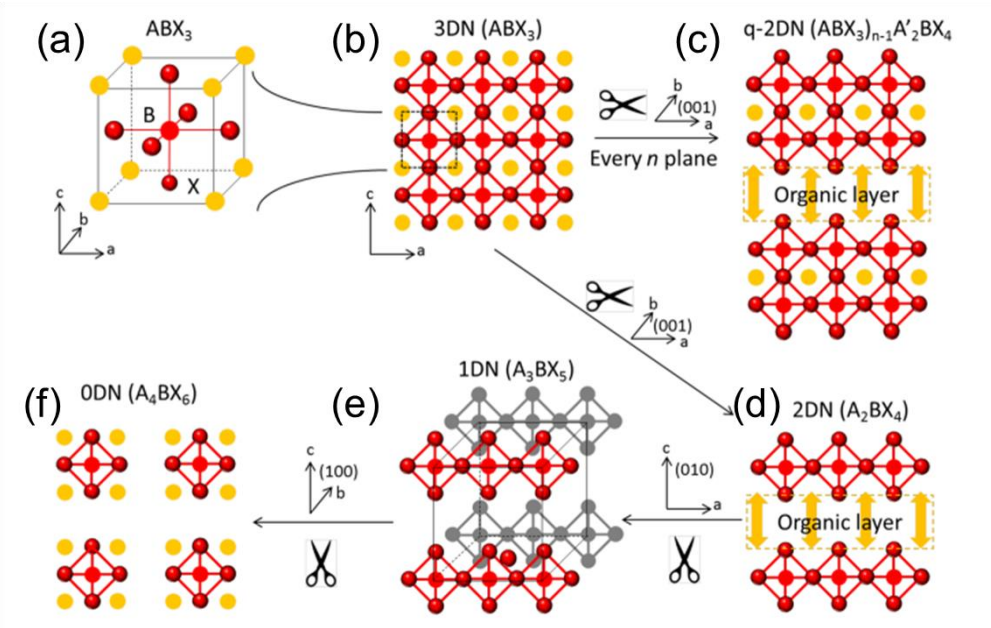

Figure 1-22. Schematic representations showing the connectivity of BX_6 octahedra in low dimensional perovskites and their formation by slicing three-dimensional along crystallographic planes[105].

1.2.3 Electrical structure of perovskite nanocrystals

In accordance with the depiction presented in Figure 1-23a, utilizing $CsPbI_3$ as an illustrative case in point, our first-principles computational findings elucidate that the conduction band minimum (CBM) and valence band maximum (VBM) predominantly originate from the contributions of Pb and I atoms, as highlighted in the range of [110-112]. To delineate the specific contributions of each constituent, a Crystal Orbital Hamilton Population (COHP) analysis is employed to scrutinize the electronic structure. The COHP analysis, illustrated in Figure 1-23b, delineates the covalent and antibonding characteristics of the Density of States (DOS) at each energy point, pinpointing the involved atomic orbitals. Figure 1-23b distinctly reveals the absence of Cs-related features in COHP, while prominently showcasing four pairs of bonding and antibonding states. This further underscores that Cs does not partake in the formation of covalent bonds; instead, it arises from the hybridization of s and p orbitals of Pb and I atoms. Specifically, the VBM comprises Pb's s antibonding orbital and I's p antibonding orbital, while the CBM is constituted by Pb's p antibonding orbital and I's s antibonding orbital. Consequently, we present s simplified energy level diagram in Figure 1-23c, where the energies of CBM and VBM, denoted as E_1 and E_2, respectively, correspond to antibonding states. Their bonding counterparts are represented by E_3 and E_4, as elucidated in [113].

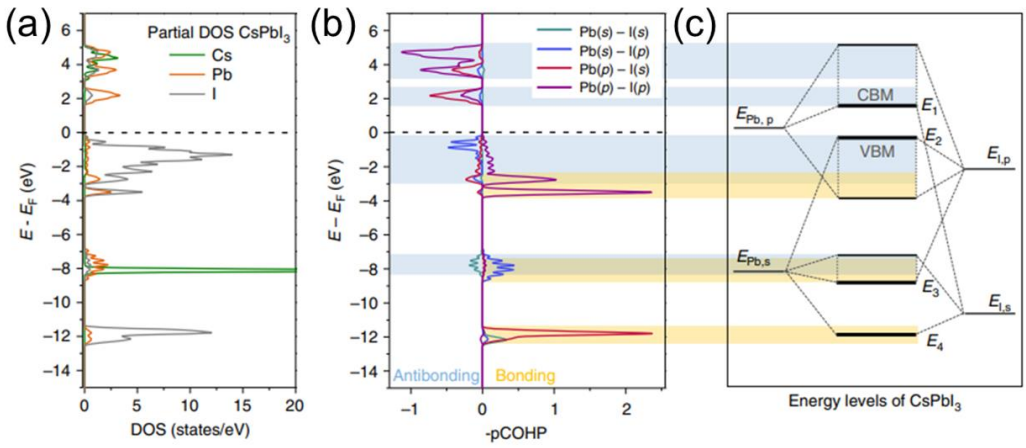

Figure 1-23. Electronic states in $CsPbI_3$. (a) The partial density of state of the Cs, Pb, and I atoms in $CsPbI_3$. (b) Orbital-resolved Crystal Orbital Hamiltonian Population (COHP) analysis; positive (negative) sign indicates bonding (anti-bonding) character. (c) Energy level diagram obtained from COHP analysis[113].

As illustrated in Figure 1-24 a, the gradual upward shift of CBM levels with the transition of atomic species from I to Cl at position X may be attributed to the heightened restriction on electrons in the p orbital of Pb atoms, resulting in an increase in energy. Conversely, the downward trend in the movement of VBM is primarily influenced by the augmented electronegativity of the X site atoms, causing the downward displacement of the p orbital. This trend, however, is mitigated by the rise in the s orbital of Pb atoms and the concurrent elevation of the hybridized orbitals with the p orbitals of X atoms. Upon substituting Pb with Sn at the M position in metal cations, the smaller electronegativity of Sn leads to lower ionization energy (IE) and electron affinity (EA) compared to their respective Pb compounds, causing an upward shift in energy levels. Simultaneously, in the Sn-based perovskite, the upward

movement of the s orbital exceeds that of the p orbital, indicating that the band gap of Sn-based perovskite is consistently smaller than its Pb-based counterpart (Figure 1-24 b). Nevertheless, $FASnBr_3$, $MASnCl_3$, and $FASnCl_3$ deviate from this trend due to lattice distortions, as elucidated by [113-114]. Concerning the impact of changing the A-site cation, as depicted in Figure 1-24 c, no uniform pattern emerges. Given that the A-site cation does not participate in bonding but influences the electronic structure through alterations in lattice volume or the introduction of lattice distortion, lattice distortion induces downward shifts in both VBM and CBM. However, its effect is more pronounced on VBM, thereby exerting a greater influence on IE. Conversely, an increase in volume enhances both IE and EA, yet the effect on EA is more significant.

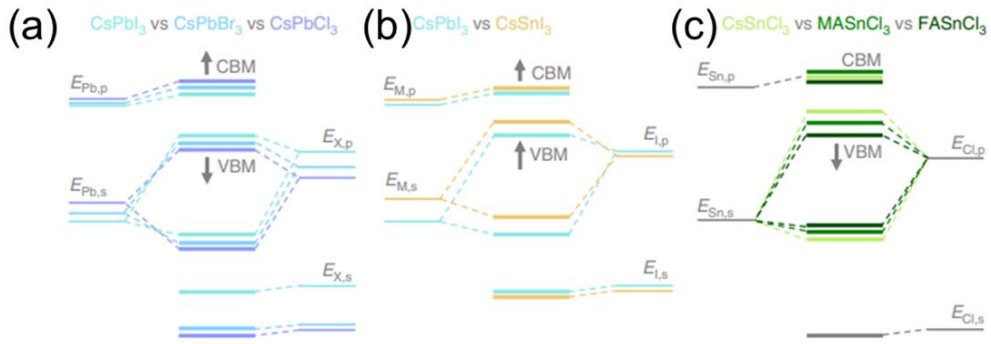

Figure 1-24. Schematic energy levels in ABX_3 perovskites. (a-b) The trends of electronic states in changing the X-cite anions and the B-cite cations, respectively. (c) The changes in electronic state caused by structural distortions in tin-based perovskites[113].

In summary, as depicted in Figure 1-25, the energy level diagrams of common perovskite structures are presented. Owing to the hybridization between metal cations and halide anions, the variations in VBM (valence band maximum) and IE (ionization

energy) are more pronounced than those in CBM (conduction band minimum). The A-site cation exhibits a negligible impact on the band gap, while substantial changes in the band gap can be achieved through the modulation of metal cations and halide anions. The trend generally entails an increase in band gap from I to Br, then to Cl, and from Sn to Pb in perovskite structures, owing to the adjustments in metal cations and halide anions. This exemplifies the profound influence that precise alterations in the constituents of metal cations and halide anions can wield on the band gap of perovskite materials.

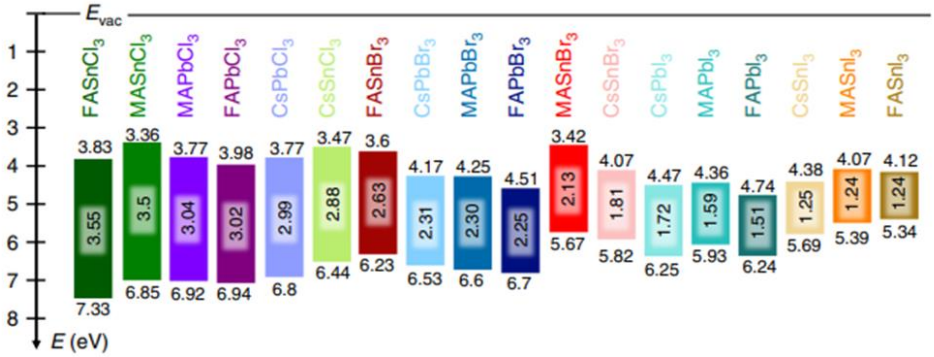

Figure 1-25. Schematic energy level alignments of the 18 metal halide perovskites[113].

1.2.4 Optoelectronic properties of perovskite nanocrystal

1.2.4.1 Tunable optical properties

It is widely acknowledged that the fluorescence of nanocrystals can be extensively tuned by altering their size. However, for perovskite nanocrystals, facile attainment of this objective can be achieved through compositional engineering, given the distinctive

characteristics of ionic crystals. Figure 1-26 a illustrates the realization of a broad visible spectrum fluorescence in organic-inorganic hybrid perovskite nanocrystals achieved by adjusting the anion composition[115], spanning effortlessly from 390 to 790 nm. Similarly, such tuning is achievable in all-inorganic nanocrystals, as depicted in Figure 1-26 b. Post-treatment with anionic solutions enables the rapid transformation of $CsPbBr_3$ with an energy gap (Eg) of 2.43 eV to $CsPbBr_xCl_{3-x}$ with Eg=3.03 eV and $CsPbBr_xI_{3-x}$ with Eg=1.88 eV. This exchange is so convenient and stable that the optical properties of nanocrystals are comparable to those synthesized through precursor-controlled methods, exhibiting remarkable optical characteristics as outlined in references [116-118].

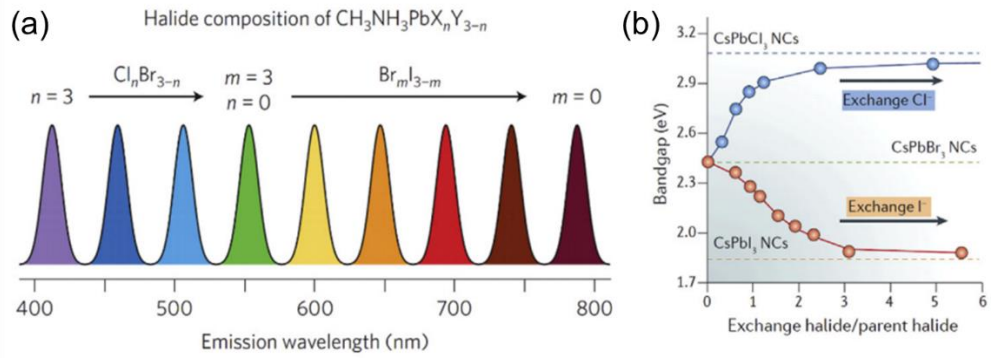

Figure 1-26. Bandgap tuning through composition substitution in the perovskite lattices. (a) The emission wavelength of the organic-inorganic hybrid $MAPbX_nY_{3-n}$ perovskites[115]. (b) Evolution of bandgap energy of inorganic $CsPbX_3$ perovskite NCs[116-118].

1.2.4.2 Large absorption coefficient

As depicted in Figure 1-27, 3D perovskite nanocrystals with a direct band gap have been reported to exhibit a remarkably high optical absorption coefficient. In

comparison to other semiconductor materials, the absorption coefficient at the band edge for perovskites reaches 10^4 cm^{-1}, with a short-wavelength absorption coefficient soaring to 10^5 cm^{-1}. This high absorption capability is of paramount importance for the applications of perovskite nanocrystals. Moreover, the absorption at the band edge and the tail of the band in perovskites follows an exponential trend, indicative of the absence of optically detectable deep-level defects[119]. Additionally, the Urbach energy, extracted through fitting the exponential part of the absorption curve, is approximately 15 meV. In contrast, amorphous silicon exhibits a Urbach energy of about 40-45 meV. This observation underscores the extremely low structural disorder in perovskite nanocrystals, as highlighted in references[119-120].

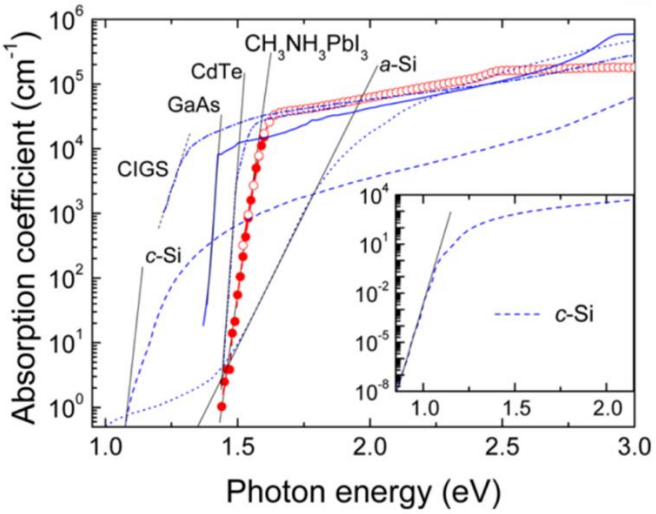

Figure 1-27. A comparation of the absorption coefficient in $CH_3NH_3PbI_3$ perovskite thin film with other typical photovoltaic materials[120].

1.2.4.3 High photoluminescence quantum yields

The distinctive feature of perovskite quantum dots lies in the fact that most of their

defects typically reside within the band, affording perovskite quantum dots the effortless achievement of 100% photoluminescence quantum yield (PLQY). As depicted in Figure 1-28 a, despite the initial report in 2014 of lead-based perovskite quantum dots optimized for green light exhibiting a modest PLQY of 20%[97], a mere year later, Kovalenko et al. reported green light lead-based perovskite quantum dots with a remarkable PLQY of up to 90% (Figure 1-28 b) [41]. Through continuous experimental optimization by researchers, perovskite quantum dots based on Cl, Br, and I have successively reached nearly 100% PLQY (Figure 1-28c) [121], showcasing the enormous advantages of perovskites in display, lighting, laser technologies, and beyond. However, in light of the toxicity issues associated with lead, researchers have redirected their focus to tin-based perovskite quantum dots. Due to the oxidation issues with tin, the PLQY of tin-based perovskite quantum dots currently remains at a relatively low level.

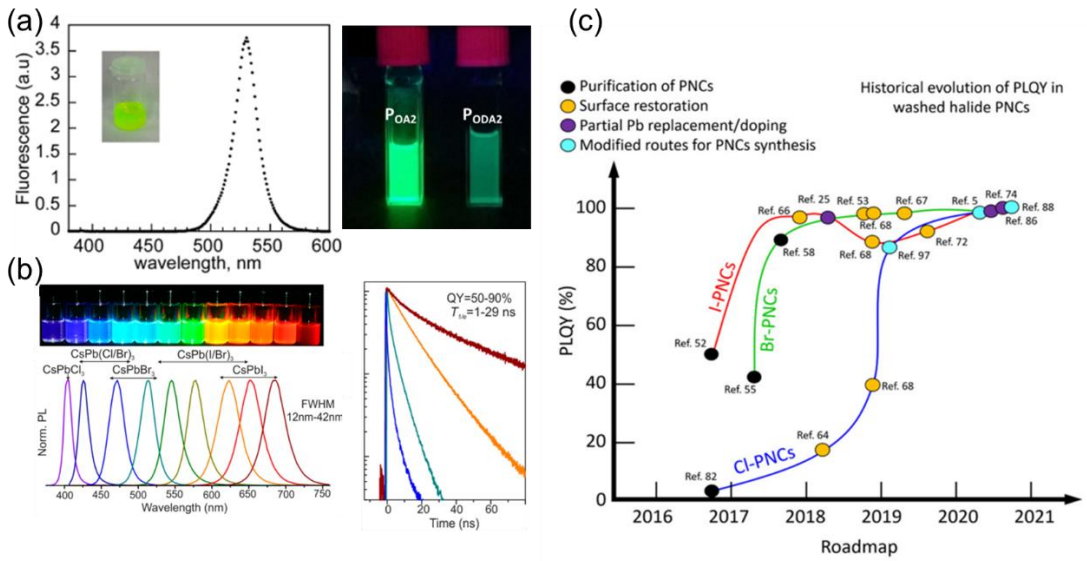

Figure 1-28. (a) The PLQY of $MAPbBr_3$[97]. (b) The PLQY of $CsPbBr_3$[41]. (c) Historical evolution of PLQY in perovskite nanocrystals[121].

1.2.4.4 High color purity

Achieving exceptionally high color purity is a prerequisite for the use of quantum dots in fields such as lasers and displays. High color purity also translates to an extremely narrow full-width at half-maximum (FWHM). $CsPbBr_3$ perovskite quantum dots, for instance, exhibit an FWHM comparable to traditional II-VI quantum dots at room temperature. Meanwhile, $CsPbCl_3$ perovskite quantum dots boast an FWHM of 9 nm at room temperature, a critical characteristic for their applications[122-123].

1.2.4.5 High defect tolerance

One of the most evident distinctions between perovskite quantum dots and traditional quantum dots lies in the perovskite's extremely high defect tolerance, contributing significantly to its high photoluminescence quantum yield (PLQY). In the study of traditional semiconductors such as silicon and GaAs, the significance of intrinsic point defects is well-established. Controlling defect levels in silicon and GaAs to the parts per billion (ppb) level is imperative for their application in photovoltaic devices, as these defects can act as electron traps or electron dopants[124]. However, despite the considerable presence of point defects in perovskite materials prepared at room temperature or without undergoing specific passivation through core-shell structures, perovskites still exhibit bright fluorescence. This indicates a high tolerance to defects within the perovskite thin films, grain boundaries, and perovskite nanocrystals[125-127]. One contributing factor to such high defect tolerance is that, among the three types of point defects (vacancies, interstitials, and antisites), only vacancies

have lower formation energies, while the latter two typically have higher formation energies, sometimes even exceeding that of the perovskite structure itself. Therefore, perovskite nanocrystals predominantly harbor vacancy defects without the presence of defect states that would induce deep energy levels (interstitials, antisites)[125, 128] (see Figure 1-29).

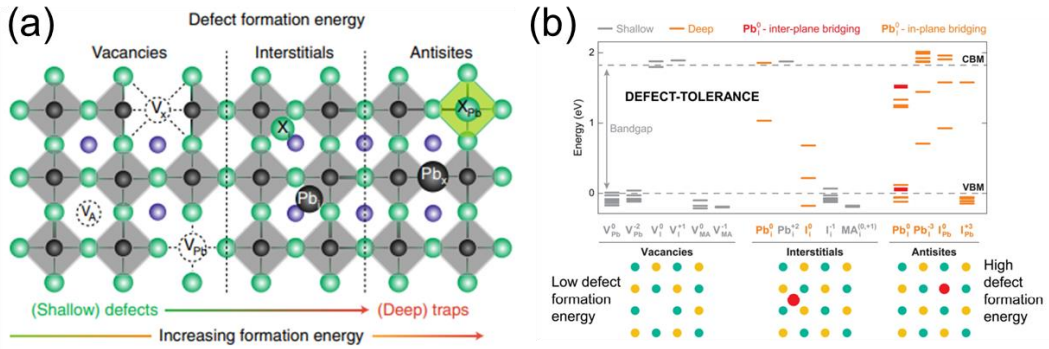

Figure 1-29. Schematic diagram of point defects in perovskite nanocrystals with vacancy defects possessing lower formation energy[110, 129].

Another reason for the extremely high defect tolerance is the unique bonding within perovskite nanocrystals. As shown in Figure 1-30a, in contrast to traditional semiconductors, the conduction band minimum (CBM) and valence band maximum (VBM) in perovskite nanocrystals are formed between two antibonding orbitals. Consequently, vacancy-induced defect states exist within the bandgap, either in the valence or conduction band, or at worst, form shallow defects. This explains why perovskite nanocrystals exhibit high PLQY. However, when we shift our focus from $CsPbBr_3$ to $CsPbCl_3$, as the bandgap widens, more defects are exposed, resulting in lower PLQY (10-20%). Additionally, an examination of the dangling bonds formed on the surface of perovskite nanocrystals reveals that they mostly give rise to shallow

defects without significantly impacting the optical properties, as shown in Figure 1-30b. For nanocrystal surfaces typically terminated with Cs^+, Br^-, and MA^+, removing the MA ions from the surface in the form of MABr (simulating the removal of amine ligands) and further eliminating CsBr (simulating a washing effect) results in a bandgap that retains no apparent traps[127].

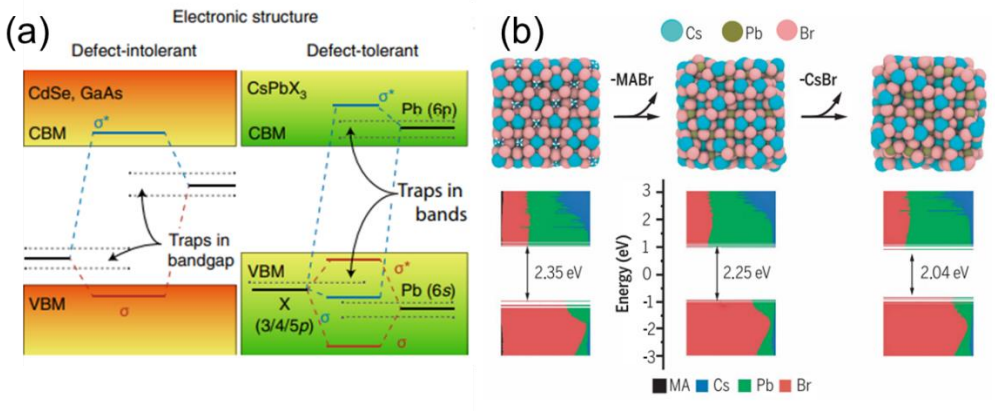

Figure 1-30. (a) Schematic representation of electronic band structure of typical defect-intolerant semiconductors and LHPs[129]. (b) Electronic structure diagrams for $CsPbBr_3$ NCs at the DFT/PBE level of theory[130].

The final reason for the exceptionally high defect tolerance in perovskites is attributed to their soft lattice and dynamic nature. To underscore their characteristics that lie between a crystal and a liquid, perovskite nanocrystals are also defined as crystalline liquids. Studies suggest that this feature shields charge carriers from the influence of defect states and scattering phenomena[131]. As shown in Figure 1-31, at room temperature, there is a strong coupling between electrons and holes within perovskite nanocrystals, leading to the formation of polarons through ion displacement. Researchers propose that polarons can shield Coulomb potential, reducing trap and

charge carrier scattering, and interact with charged defects and optical phonons [131-132]. In A-site mixed perovskites, the molecular rotation of A-site cations on a picosecond or sub-picosecond scale can be utilized to shield hot carriers, offering opportunities for utilizing or observing hot carriers. The tolerance of defects in perovskite nanocrystals is primarily attributed to the contributions from the s and p orbitals of Pb atoms. Researchers have also summarized strategies for introducing defect tolerance in lead sulfide quantum dots, emphasizing the importance of dielectric constants, effective mass, and the interactions between defects[133].

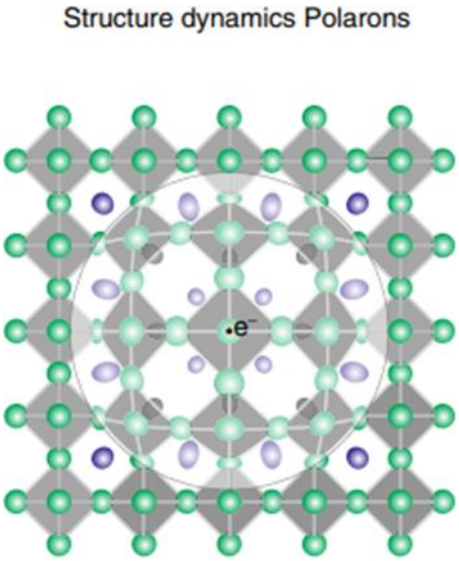

Figure 1-31. Schematic representation of local structural deformation of the Pb–Br framework that, combined with a charge carrier (electron or hole), forms a polaron[129].

1.2.4.6 Excellent transport properties

Perovskites exhibit outstanding transport properties owing to their low exciton binding energy, high charge carrier mobility, and long diffusion lengths[134-136]. As depicted in Figure 1-32 a, the exciton binding energy in halide perovskites is only a few

tens of meV, indicating that non-equilibrium charge carriers generated at room temperature primarily exist in the form of free electrons and holes. Additionally, the coupling of the Pb atoms' s and p antibonding orbitals results in a small effective mass for both electrons and holes, contributing to the material's high mobility (Figure 1-32 b). Coupled with the minimal defect states and lower defect energy levels mentioned earlier, non-equilibrium charge carriers exhibit diffusion lengths exceeding several hundred nanometers (Figure 1-32 c) [137].

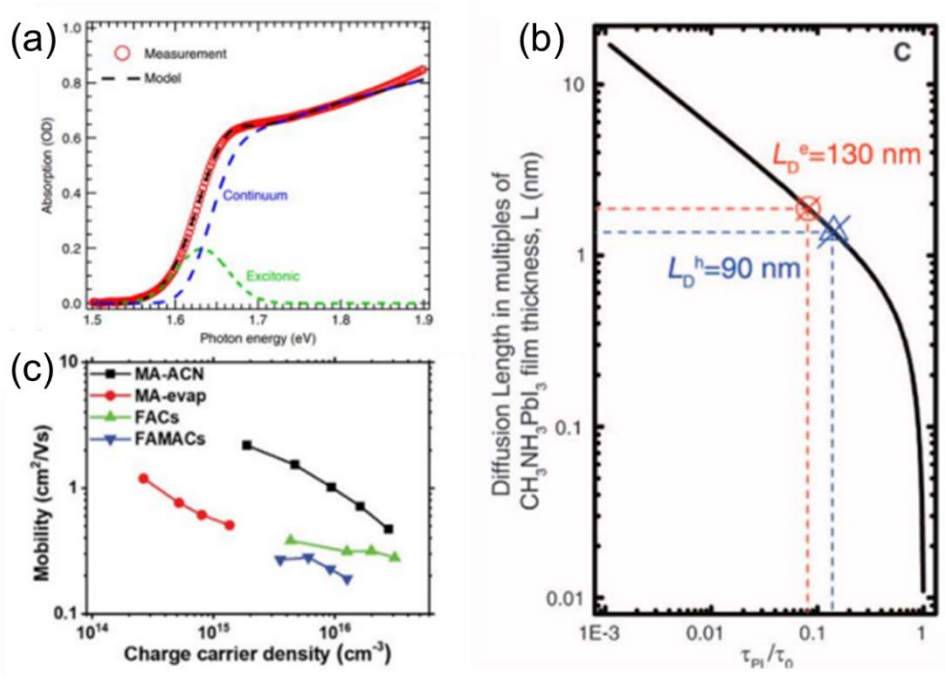

Figure 1-32. (a) The band edge absorption of $MAPbI_3$ film. The exciton binding energy fitted with Elliott formula is about 11 meV[136]. (b) Mobility of perovskites as a function of carrier density[134].(c) Carrier diffusion length of $MAPbI_3$ film[137].

1.2.5 Synthesis and classification of perovskite nanocrystals

Presently, researchers have developed various methods for synthesizing perovskite

nanocrystals. One widely used method is the hot injection method (HI), as illustrated in Figure 1-33 a. In this approach, precursor solutions for A-site cations are first prepared separately. Then, a solution containing metal halides and long-chain alkyl ligands is dried under vacuum. After heating to a specific temperature, the A-site cation solution is rapidly injected. Ligand-assisted reprecipitation (LARP) is another extensively employed synthetic method[138]. As shown in Figure 1-33 b, the precursor solution is a mixture of A-site cation source, metal halide source, and ligands dissolved in N,N-dimethylformamide (DMF). The precursor is then dripped into toluene or 1-octadecene (ODE), inducing the formation and aggregation of perovskite nanocrystals (PNCs). LARP technology is a low-cost and scalable process applicable for the preparation of all-inorganic and organic-inorganic hybrid PNCs. In addition to the above methods, the emulsion method shows promise as a synthetic route[139]. As depicted in Figure 1-33 c, a milky solution is formed by uniformly mixing the DMF solution containing precursors with a nonsolvent (toluene or n-hexane). The addition of a surfactant (typically tert-butanol) induces nucleation and growth instantly[140]. Microwave-assisted synthesis is also utilized for perovskite nanocrystal preparation, as shown in Figure 1-33 d. The use of microwaves allows for controlled shaping of nanocrystals and facilitates the rapid synthesis of perovskite nanocrystals, providing an observable time window for studying nucleation and growth[141]. Additionally, other methods for synthesizing perovskite nanocrystals include ball milling, ultrasonication, hydrothermal methods, etc.

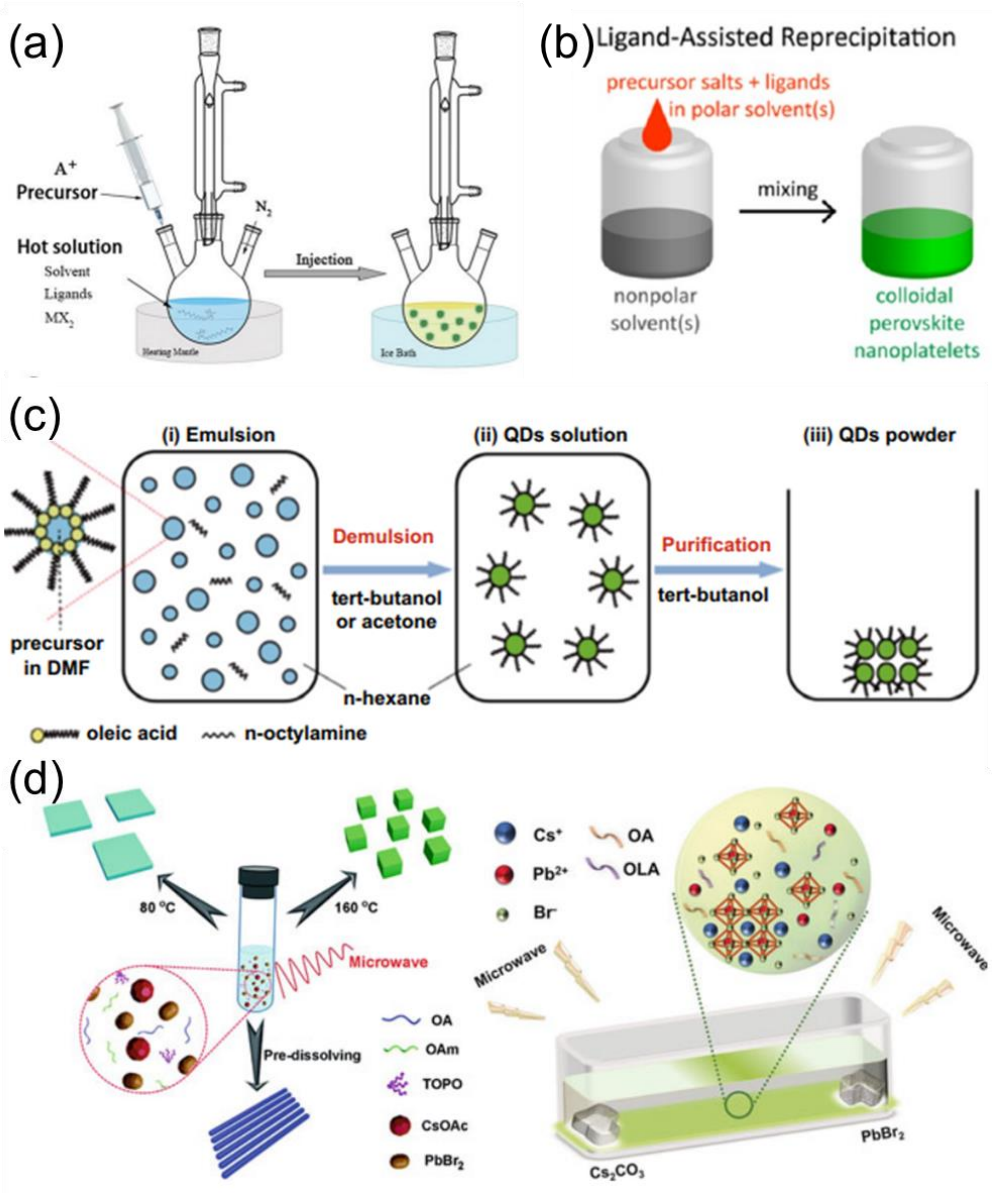

Figure 1-33. (a) Schematic diagram of the hot-injection method for synthesizing inorganic perovskite QDs[138]. (b) Schematic diagram of the LARP method for synthesizing inorganic perovskite QDs[139]. (c) Schematic diagram of the emulsion method for synthesizing inorganic perovskite QDs[140]. (d) Schematic diagram of the wavelength-assisted method for synthesizing inorganic perovskite QDs[141].

1.2.6 $CsPbBr_3$ nanocrystals

Among the perovskite family ABX_3 (X = Cl, Br, I), $CsPbBr_3$ stands out as the most

representative. Compared to $CsPbCl_3$, it exhibits higher defect tolerance, making it easier to achieve near 100% photoluminescence quantum yield (PLQY). In comparison to $CsPbI_3$, $CsPbBr_3$ demonstrates better phase stability, improved mechanical properties, and water stability. Additionally, $CsPbBr_3$ is a direct bandgap semiconductor with high charge carrier mobility and a long electron-hole diffusion length. It possesses excellent optical properties such as strong absorption coefficients and tunable emission wavelengths. These characteristics make $CsPbBr_3$ highly promising for potential applications in areas such as light-emitting diodes (LEDs), lasers, and high-energy radiation detectors[142].

1.2.7 Two-dimensional perovskites

The 2D perovskite, composed of organic cations in the stacked layers of mixed-halide perovskite, forms a semiconductor material. These layers are separated by organic cation-based interlayers or barriers. 2D perovskites exhibit a range of unique structural and physical properties, including a soft and dynamic structure, strong anisotropy, high photoluminescence quantum efficiency, broad light emission, intense bound excitons at room temperature, prospects for room-temperature all-optical spin manipulation, large Rashba splitting, significant ferroelectric and nonlinear effects, and layered ferromagnetism. The heterostructure of 2D perovskite and 3D halide perovskite enhances the efficiency and stability of photovoltaic (PV) and light-emitting diode (LED) devices. It has achieved stability for hundreds of hours in high-efficiency solar cells and an external quantum efficiency exceeding 20% in high-color purity and

tunable LEDs. 2D perovskites, made from abundant earth elements, are cost-effective and easy to synthesize using low-temperature (100°C) solution processing methods. Furthermore, the physical properties of 2D perovskites observed at the single-layer level often remain unchanged in bulk samples. Their properties seem to integrate the best features of 3D halide perovskites, multiple quantum wells (MQWs), graphene-like 2D semiconductors, and organic semiconductors, as summarized in Table 1-1[143].

Table 1-1. Physical properties of organic–inorganic 2D halide perovskites and canonical semiconductors[143].

	2D hybrid perovskite $A'A_{n-1}B_nX_{3n+1}$	Quantum wells	2D graphene-like semiconductors	3D hybrid perovskite, ABX_3	Organic semiconductors
Structure	Perovskite layer $A_{n-1}B_nX_{3n+1}$ ~10^0–10^1 nm; Organic spacer A′ ~10^{-1}–10^0 nm	Quantum well ~10^0–10^1 nm; Barrier <5 nm	2D atomic layer ~10^{-1} nm; van der Waals ~10^{-1} nm	Octahedra BX_6^- ~0.63 nm; Organic A ~10^{-1} nm	C_{70}; Y6 (BTP-4F)
Material examples	A′ = aliphatic, aromatic organics A = methylamonium B = Pb, Sn, Ge, Mn X = I, Br, Cl	AlGaAs/GaAs, InGaAs/GaAsp	Transition metal dichalcogenides (MoS_2, WSE_2), phosphorene	A = methylamonium, formanidinium B = Pb, Sn, Ge X = I, Br, Cl	Fullerene, PPV, polyacetylene, BTP-4F, IT-4F
Electronic bandgap (typical range)	1.4–3.8 eV	0.1–4.0 eV	1.0–6.0 eV	1.4–3.2 eV	1.0 – 5.0 eV
Exciton binding energy	<0.5 eV	<50 meV	0.1–0.3 eV	<50 meV	0.5–1.0 eV
Exciton reduced mass (units of m_0)	0.1–0.25	0.1–0.2	0.1–0.4	0.1	
Young's modulus	1–10 GPa	500–200 GPa	50–350 N m^{-1} 250 Gpa (> 2 layers)	1–40 GPa	~1 GPa
Synthesis, processing methods	In solution (~100 °C), dry and wet exfoliation	MBE, MOCVD	Dry and wet exfoliation, CVD	In solution (~100 °C), CVD, sputtering	Wet, organic chemistry
Sample types	Single crystal, down to 1 layer, thin film	Expitaxial layers, a few heterolayers	1–5 layers	Single crystal, thin film	Thin film, assembly of molecules

1.3 Perovskite nanocrystal heterojunctions

At the nanoscale, the exploration of heterostructures—wherein two or more materials are intricately interwoven into a singular unit—has become a focal point of extensive investigation, propelled by the remarkable material properties inherent in such configurations. In the domain of optical materials, these nanostructures, shaped by

the characteristics of heterogenous combinations, prove instrumental in constraining or efficiently transmitting photogenerated charge carriers from one component to another. Consequently, these nanomaterials have found widespread applications in realms such as enhancing luminescent efficiency, elevating photovoltaic performance, and augmenting catalytic activity. Capitalizing on the superb optoelectronic attributes inherent in perovskite nanocrystals, heterostructures grounded in perovskite nanocrystals have garnered heightened attention. Under the influence of diverse coupling materials, these structures exhibit heightened optical stability, increased emission intensity, and the intriguing coupling of excitons with plasmon resonances, thereby attracting broader interest and scrutiny within the scientific community.

1.3.1 Synthesis of perovskite nanocrystal heterojunctions

The in-situ epitaxial growth of perovskite heterostructures stands out as a pivotal technique, given that smaller lattice stresses and robust bonding synergistically contribute to the overall stability of these heterostructures—an attribute advantageous for their application in optoelectronic devices. Chen et al. pioneered the synthesis of $CsPbBr_{3-x}I_x$ quantum dots using the conventional hot injection method within the 1-octadecene (ODE), oleic acid (OA), and octadecene amine system. Subsequently, zinc stearate and 1-dodecanethiol were sequentially introduced into the $CsPbBr_{3-x}I_x$ solution to facilitate the growth of ZnS[144] on $CsPbBr_{3-x}I_x$ quantum dots (Figure 1-34 a). Heterostructures comprising $CsPbBr_3$ and gold were also successfully synthesized in situ (Figure 1-34 b) [145]. Bromine gold salt served as the precursor for gold, while the

introduction of $PbBr_2$ into the solution acted as a competitive reagent, preventing the substitution of gold ions into the quantum dot lattice. Yang et al. demonstrated an in-situ synthesis of $CsPbBr_3$-TiO_2 heterostructures at room temperature using a grinding method. Remarkably, the rigid TiO_2 spheres, during the grinding process, transformed the cubic shape of $CsPbBr_3$ into spherical, firmly anchoring onto the surface of $CsPbBr_3$ (Figure 1-34 c) [146]. Additionally, as depicted in Figure 1-34 d, Yang et al. employed a microwave-assisted approach to prepare $CsPbBr_3$ nanocrystals encapsulated with dimethylsiloxane. The hydrophobic nature of dimethylsiloxane significantly enhanced the thermal stability of $CsPbBr_3$ nanocrystals, showcasing improved performance in both thermal stability and light-emitting diodes (LEDs) [147].

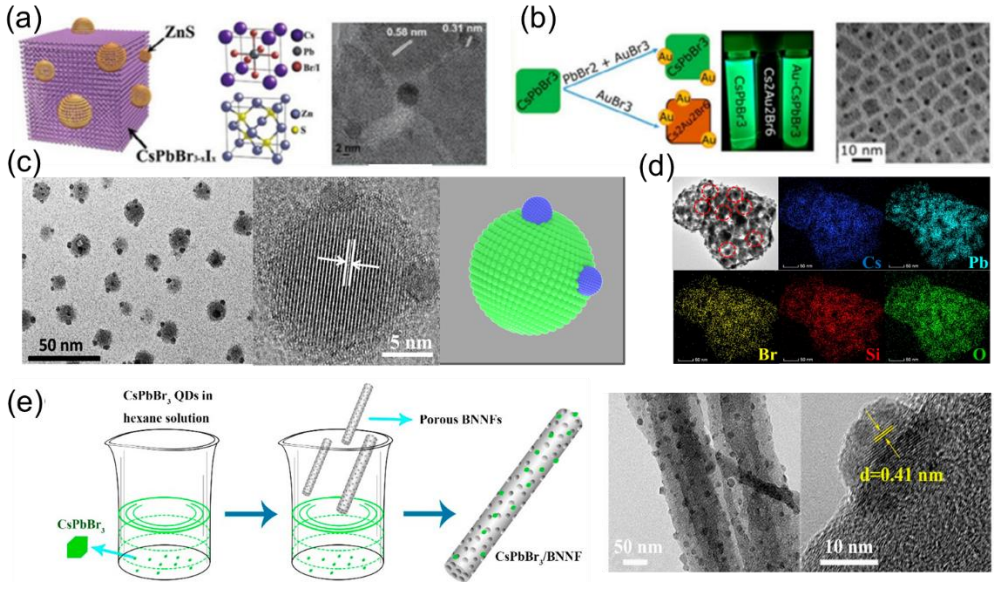

Figure 1-34. (a) $CsPbBr_{3-x}I_x$–ZnS QD heterojunctions[144]. (b) Au–$CsPbBr_3$ nano-heterojunctions[145]. (c) TiO_2@$CsPbBr_3$ architectures and the corresponding structure models[146]. (d) TEM elemental mapping images of coated $CsPbBr_3$ NCs[147]. (e) Preparation and HRTEM images of $CsPbBr_3$–BNNFs heterojunctions[148].

In addition to the aforementioned in-situ methods for fabricating perovskite nanocrystal heterostructures, an alternative approach involves a non-in-situ, one-step synthesis. The notable advantage of this method lies in the high controllability of parameters for both components, as they are pre-designed. However, a limitation of this approach is that the heterostructures produced often entail simple physical adsorption or relatively weak van der Waals forces. The fundamental synthetic concept revolves around the separate preparation of perovskite and heterostructure materials, followed by their integration to form the heterostructure (Figure 1-34e) [148]. Perovskite quantum dots can be deposited onto the target surface of the heterostructure material. Alternatively, a mixture of perovskite quantum dots and heterostructure materials can be spin-coated or dip-coated onto a substrate, resulting in the formation of the heterostructure. Despite its simplicity, this method provides a robust platform for tailoring the properties of the heterostructure, yet it is essential to acknowledge that the interactions governing the assembly are primarily dominated by physical adsorption or weaker van der Waals forces.

1.3.2 Structure of perovskite nanocrystal heterojunctions

The structural configuration of nanoscale heterojunctions, dictated by the varying bandgap widths and relative vacuum energy level positions of two different semiconductors, manifests as discontinuous steps at the conduction band minimum (CBM) and valence band maximum (VBM), resulting in band offsets known as conduction band offset (CBO) and valence band offset (VBO). Consequently, three

fundamental types of heterojunction structures emerge, as illustrated in Figure 1-35 [149]. The first type, referred to as "straddling gap" (type I), alternatively termed charge carrier recombination type, typically comprises a combination of a wide-bandgap semiconductor and a narrower-bandgap semiconductor. In this arrangement, photogenerated carriers swiftly transfer from the wide-bandgap semiconductor to the narrow-bandgap semiconductor, facilitating radiative recombination and ultimately leading to enhanced photoemission. The second type, termed "staggered gap" (type II), also known as charge separation type, involves the transfer of electrons to a semiconductor with a lower CB position, while holes migrate to a semiconductor with a higher VB position. This configuration facilitates effective electron-hole separation. Quasi-type II heterojunctions can induce electron (or hole) diffusion, while the corresponding hole (or electron) remains confined. The third type, known as "broken gap" (type III), constitutes the well-known simplest form of a PN junction. Apart from semiconductor-semiconductor combinations, heterojunctions can also involve semiconductors with conductors (such as metal nanoparticles) or insulators. In contrast to heterojunctions, homojunctions are structures formed by the same material but with different doping types or doping levels within the semiconductor.

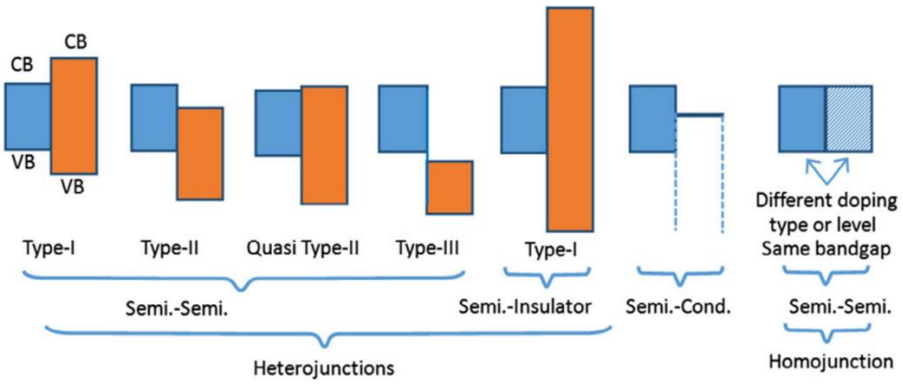

Figure 1-35. The band diagram of semiconductor heterojunctions and homojunctions[149].

1.3.3 Photophysical properties of perovskite nanocrystal heterojunctions

Comprehending the photophysical processes within perovskite materials is crucial for a profound understanding of the photophysical processes within perovskite nanocrystal heterostructures. As depicted in Figure 1-36, when optically excited to generate excitons, the resulting electron-hole pairs may partake in various physical processes within the perovskite, including internal, surface, and interface phenomena such as thermal carrier extraction, biexciton generation, singlet or triplet recombination, Auger processes[150], traps/dark states[151], and radiative emission. Among these processes, thermal carrier Auger and cooling processes imply the cooling of hot carriers associated with Auger-type energy transfer within the band structure. Under conditions where hole-state density is high and electron-state density is low, hot electrons can cool to hole states through Auger-type energy transfer. Subsequently, hot holes rapidly cool via phonon emission. If both electrons and holes possess symmetric discrete energy levels, the cooling of hot carriers slows down, a phenomenon known as the phonon bottleneck effect. These properties are of paramount importance in investigating the electronic structure and physical processes of complex systems, especially in heterostructures based on perovskites[152].

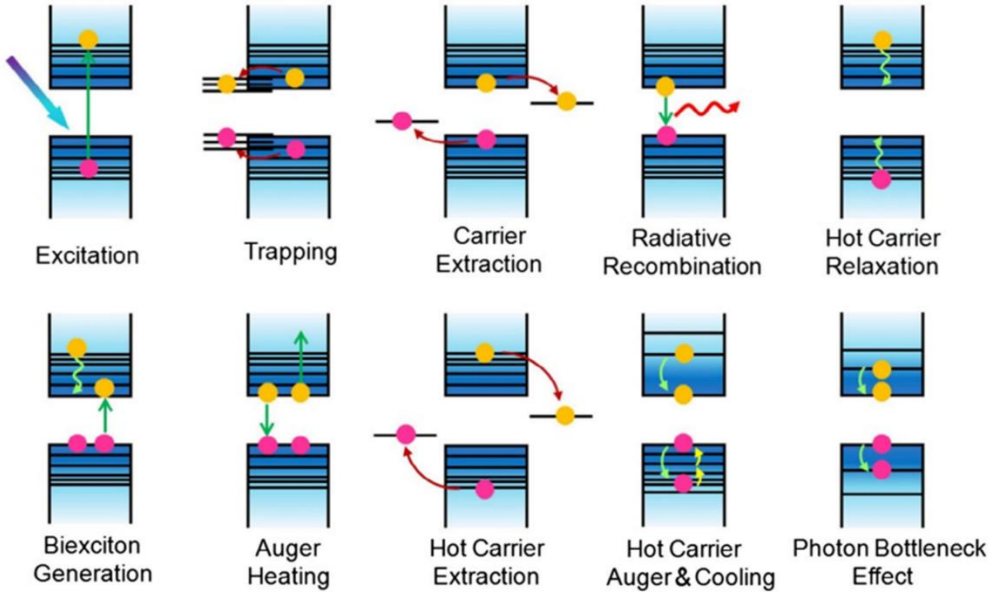

Figure 1-36. Schematic illustration of exciton or charge carrier process in QDs[149].

Research on hot carriers in perovskite heterostructures is particularly significant. Calculations indicate that if hot carriers can be effectively extracted, the efficiency of single-junction solar cells could reach 66% [153]. As illustrated in Figure 1-37a, Sarkar et al. reported the phenomenon of thermal electron and hole transfer from $CsPbBr_3$ to the LUMO of BQ and the HOMO of PTZ, respectively [154]. Li et al. also documented thermal electron transfer between MAPbBr3 and Bphen. Due to the type I heterojunction between Bphen and $MAPbBr_3$, only thermal electrons with energies exceeding ~0.2 can be extracted. The crucial requirements for efficient hot carrier transfer include high acceptor-state density in the LUMO and strong coupling between the high-energy electron state density and the heterojunction interface [155].

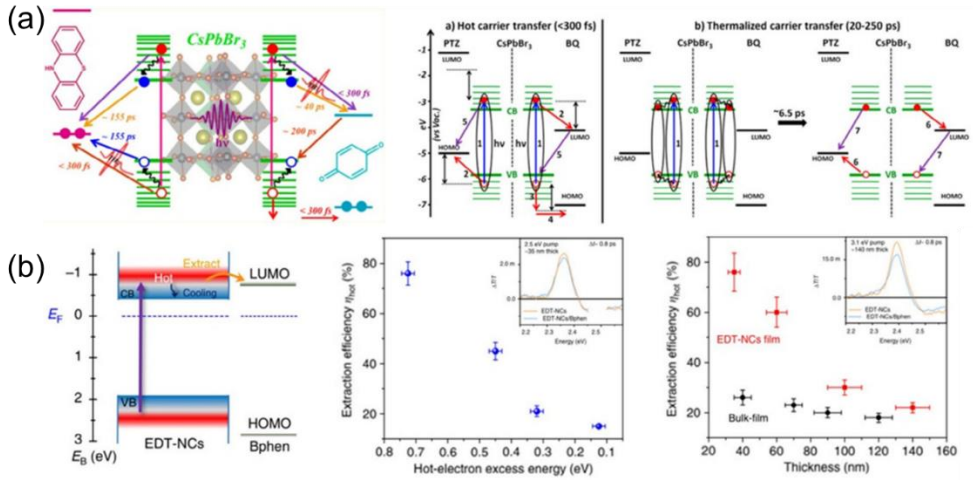

Figure 1-37. (a) Schematics of the carrier transfer and recombination processes in CsPbBr3 NC-BQ and NC-PTZ systems upon photo excitation[154]. (b) Schematic illustration of the energy-level diagram and the hot electron extraction from perovskite NCs to Bphen with competing hot-electron cooling pathways[155].

1.3.4 Applications of perovskite nanocrystal heterojunctions

The distinctive structure of perovskite nanocrystal heterostructures has laid the foundation for their applications in solar cells, photodetectors, LEDs, and photocatalysis. As depicted in Figure 1-38 a, compared to pure $CsPbI_3$ nanocrystal solar cells (with a power conversion efficiency, PCE, of approximately 10.2%), $CsPbI_3$-PbSe heterojunction solar cells exhibit an enhanced PCE of 13.9%, attributed to superior charge separation within the heterostructure[156]. Utilizing $CsPbCl_3$ as a foundation, an AuCu-$CsPbCl_3$ core-shell nanocrystal heterostructure in photodetectors demonstrates higher photoresponsivity in the range of 300-600 nm, owing to the plasmon-exciton coupling effect within the heterojunction (Figure 1-38 b) [157]. Constructing a NiOx layer of as thin as 10 nm at the upper and lower interfaces of $CsPbBr_3$ nanocrystal films

creates the $CsPbBr_3$-NiOx heterostructure, enhancing radiative recombination. Based on this design, the highest external quantum efficiency (EQE) achieved in LEDs reaches 26.7% (Figure 1-38 c)[158]. Similarly, the $CsPbBr_3$-$Pb_4S_3Br_2$ heterojunction, based on $CsPbBr_3$, is a quasi-type-II structure. This configuration not only facilitates carrier transfer but also enhances the rate of catalytic reactions (Figure 1-38d) [159].

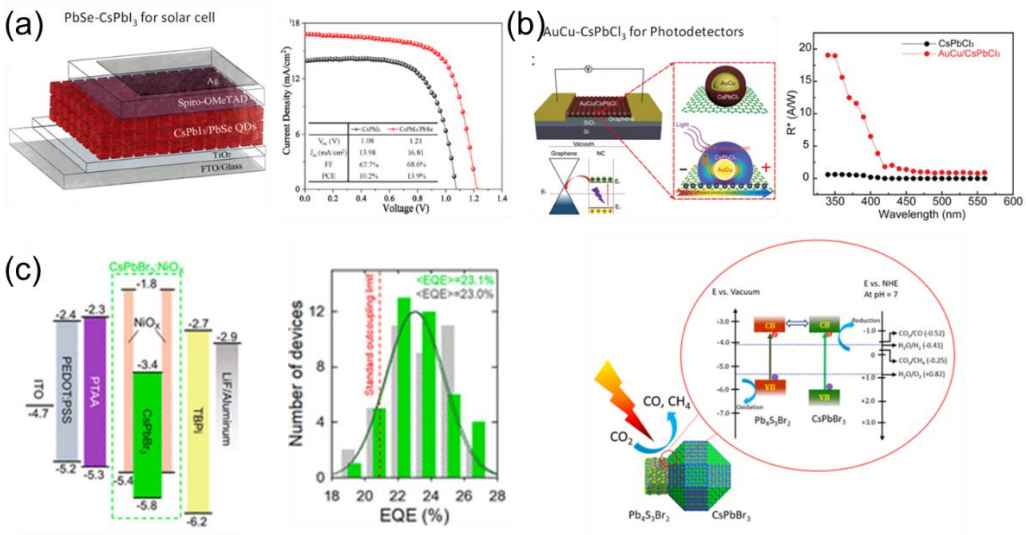

Figure 1-38. (a) Schematic representation of the $CsPbI_3$/PbSe nanocrystal-based solar cell device and its J-V cuves[156]. (b) Schematic illustration and Photoresponsivity of the AuCu/$CsPbCl_3$ core/shell nanocrystals/graphene nanohybrids photodetector and the inset describing schematically an individual AuCu/$CsPbCl_3$ core/shell nanocrystal on graphene in dark conditions (top) and under light illumination (bottom) showing the evanescent field in the $CsPbCl_3$ shell[157]. (c) Flat band energy diagram of a multilayer LED highlighting the shift of the frontiers level of $CsPbBr_3$ PNCs upon treatment with NiO_X[158]. (d) Schematic presentation of the energy band diagram and photocatalytic CO_2 reduction reaction at the junction of the poly (110) $CsPbBr_3$–$Pb_4S_3Br_2$ heterostructure[159].

1.4 Research purpose and motivations

Nano heterostructures derived from perovskite nanocrystals hold immense potential across various research domains. However, a comprehensive understanding of the synthesis chemistry involved in fabricating these heterostructures, particularly achieving facile, rapid, and in situ epitaxial growth for solution-processed nanoscale heterostructures, remains a challenging endeavor. Furthermore, delving into the photophysical properties of heterostructures synthesized via in situ epitaxial growth and exploring diverse application scenarios across different systems is of significant importance.

1.5 Research contents and innovations

In this study, based on our research in synthetic chemistry, we have developed a method for the in-situ external derivation and growth of $CsPbBr_3$-PbS nano heterostructures at room temperature. Investigations into their photophysical properties have revealed a faster carrier transfer rate, indicating a higher photoluminescence quantum yield (PLQY) for the $CsPbBr_3$-PbS heterojunction, owing to the enhanced carrier transfer dynamics. Building upon this discovery, we have pioneered the application of the nano heterostructures we synthesized in the field of shortwave infrared imaging (SWIR). This marks the first instance where such nano heterostructures have found utility in this domain, signifying a breakthrough in the realm of SWIR technology.

Furthermore, under room temperature conditions, For the first time, we have

achieved the in-situ epitaxial growth of 3D-2D $CsPbBr_3$-PMA_2PbBr_4 lateral heterostructures. These structures exhibit rapid carrier separation and an extended carrier diffusion length, attributed to their type-II heterojunction characteristics. This innovative approach not only advances the current understanding of heterostructure formation but also opens new avenues for the development of high-performance optoelectronic devices, showcasing the potential of these unique 3D-2D lateral heterostructures in various applications within the realm of materials science and beyond.

1.6 Outline of this thesis

Chapter 1 serves as an introduction, providing a historical overview of quantum dots, their characteristics, synthesis methods, and classification. It briefly introduces PbS quantum dots and outlines the research history, crystal structure, electronic structure, and optoelectronic properties of perovskite nanocrystals. The chapter further discusses the synthesis and classification of $CsPbBr_3$ nanocrystals and two-dimensional perovskites. Finally, it outlines the research objectives and scope of this thesis.

Chapter 2 provides a comprehensive introduction to the pertinent knowledge on characterization techniques, specifically focusing on transient absorption spectroscopy and electron microscopy.

Chapter 3 presents our in-situ synthesis of $CsPbBr_3$-PbS heterostructures under ambient conditions. This chapter primarily encompasses our research on the synthetic chemistry of these heterostructures. Ultrafast transient absorption spectroscopy has

been employed to unravel rapid carrier transfer rates and efficiency, shedding light on our pioneering exploration in the Short-Wave Infrared (SWIR) domain.

Chapter 4 primarily delves into the in-situ synthesis of 3D-2D $CsPbBr_3$-PMA_2PbBr_4 structures. This chapter encompasses several key aspects, including the optimization of heterostructure synthesis based on synthetic chemistry. It explores the transfer and diffusion lengths of carriers using time-resolved fluorescence spectroscopy and ultrafast transient absorption spectroscopy. The chapter delves into the mechanism of epitaxial growth through the utilization of aberration-corrected electron microscopy. Theoretical confirmation of our results is provided through Density Functional Theory (DFT) calculations. Additionally, insights into the origin of lattice strain within the heterostructure are revealed through low-temperature fluorescence studies.

Chapter 5 concludes this thesis by summarizing the research findings and provides a prospective outlook on future work.

1.7 Bibliography

1. Efros, A. L.; Brus, L. E., Nanocrystal quantum dots: from discovery to modern development. *ACS nano* **2021,** *15* (4), 6192-6210.
2. Ekimov, A. I., Quantum size effect in three-dimensional microscopic semiconductor crystals. *Jetp Lett.* **1981,** *34*, 345.
3. Lifshitz, I.; Slezov, V., Kinetics of diffusion decomposition of supersaturated solid solutions. *Soviet Physics JETP* **1959,** *35* (2), 8.
4. Ekimov, A. I.; Hache, F.; Schanne-Klein, M.; Ricard, D.; Flytzanis, C.; Kudryavtsev, I.; Yazeva, T.; Rodina, A.; Efros, A. L., Absorption and intensity-dependent photoluminescence measurements on CdSe quantum dots: assignment of the first electronic transitions. *JOSA B* **1993,** *10* (1), 100-107.

5. Ekimov, A.; Onushchenko, A.; Tsekhomskii, V., Exciton absorption by copper (I) chloride crystals in a glassy matrix. *Fizika i Khimiya Stekla* **1980,** *6* (4), 511-2.

6. Golubkov, V.; Ekimov, A.; Onushchenko, A.; Tsekhomskii, V., The Growth Kinetics of CuCl Microcrystals in a Vitreous Matrix. *Fiz. Khim. Stekla* **1981,** *7* (4), 397-401.

7. Mau, A. W.-H.; Huang, C.-B.; Kakuta, N.; Bard, A. J.; Campion, A.; Fox, M. A.; White, J. M.; Webber, S. E., H2 photoproduction by Nafion/CdS/Pt Films in H20/S2-solutions. *J. Am. Chem. Soc* **1984,** *106* (22), 6537-6542.

8. Tricot, Y. M.; Emeren, A.; Fendler, J. H., In situ generation of catalyst-coated cadmium sulfide particles in polymerized and unpolymerized surfactant vesicles and their utilization for efficient visible-light-induced hydrogen production. *The Journal of Physical Chemistry* **1985,** *89* (22), 4721-4726.

9. Grätzel, M.; Moser, J., Multielectron storage and hydrogen generation with colloidal semiconductors. *Proceedings of the National Academy of Sciences* **1983,** *80* (10), 3129-3132.

10. Henglein, A., Photochemistry of colloidal cadmium sulfide. 2. Effects of adsorbed methyl viologen and of colloidal platinum. *The Journal of Physical Chemistry* **1982,** *86* (13), 2291-2293.

11. Fojtík, A.; Weller, H.; Koch, U.; Henglein, A., Photo-Chemistry of Colloidal Metal Sulfides 8. Photo-Physics of Extremely Small CdS Particles: Q-State CdS and Magic Agglomeration Numbers. *Berichte der Bunsengesellschaft für physikalische Chemie* **1984,** *88* (10), 969-977.

12. Koch, U.; Fojtik, A.; Weller, H.; Henglein, A., Photochemistry of semiconductor colloids. Preparation of extremely small ZnO particles, fluorescence phenomena and size quantization effects. *Chemical Physics Letters* **1985,** *122* (5), 507-510.

13. Brus, L. E., A simple model for the ionization potential, electron affinity, and aqueous redox potentials of small semiconductor crystallites. *The Journal of chemical physics* **1983,** *79* (11), 5566-5571.

14. Brus, L. E., Electron–electron and electron-hole interactions in small

semiconductor crystallites: The size dependence of the lowest excited electronic state. *The Journal of chemical physics* **1984,** *80* (9), 4403-4409.

15. Rossetti, R.; Hull, R.; Gibson, J.; Brus, L. E., Excited electronic states and optical spectra of ZnS and CdS crystallites in the≅ 15 to 50 Å size range: Evolution from molecular to bulk semiconducting properties. *The Journal of chemical physics* **1985,** *82* (1), 552-559.

16. Rossetti, R.; Hull, R.; Gibson, J.; Brus, L., Hybrid electronic properties between the molecular and solid state limits: lead sulfide and silver halide crystallites. *The Journal of chemical physics* **1985,** *83* (3), 1406-1410.

17. Chestnoy, N.; Hull, R.; Brus, L., Higher excited electronic states in clusters of ZnSe, CdSe, and ZnS: Spin-orbit, vibronic, and relaxation phenomena. *The Journal of chemical physics* **1986,** *85* (4), 2237-2242.

18. Colvin, V.; Goldstein, A.; Alivisatos, A., Semiconductor nanocrystals covalently bound to metal surfaces with self-assembled monolayers. *Journal of the American Chemical Society* **1992,** *114* (13), 5221-5230.

19. Murray, C.; Norris, D. J.; Bawendi, M. G., Synthesis and characterization of nearly monodisperse CdE (E= sulfur, selenium, tellurium) semiconductor nanocrystallites. *Journal of the American Chemical Society* **1993,** *115* (19), 8706-8715.

20. Hines, M. A.; Guyot-Sionnest, P., Synthesis and characterization of strongly luminescing ZnS-capped CdSe nanocrystals. *The Journal of Physical Chemistry* **1996,** *100* (2), 468-471.

21. Talapin, D. V.; Mekis, I.; Götzinger, S.; Kornowski, A.; Benson, O.; Weller, H., CdSe/CdS/ZnS and CdSe/ZnSe/ZnS Core− Shell− Shell Nanocrystals. *The Journal of Physical Chemistry B* **2004,** *108* (49), 18826-18831.

22. Nirmal, M.; Dabbousi, B. O.; Bawendi, M. G.; Macklin, J.; Trautman, J.; Harris, T.; Brus, L. E., Fluorescence intermittency in single cadmium selenide nanocrystals. *Nature* **1996,** *383* (6603), 802-804.

23. Murray, C.; Kagan, C.; Bawendi, M., Self-organization of CdSe nanocrystallites into three-dimensional quantum dot superlattices. *Science* **1995,** *270* (5240), 1335-1338.

24. Boles, M. A.; Engel, M.; Talapin, D. V., Self-assembly of colloidal nanocrystals: From intricate structures to functional materials. *Chemical reviews* **2016,** *116* (18), 11220-11289.

25. Ye, X.; Millan, J. A.; Engel, M.; Chen, J.; Diroll, B. T.; Glotzer, S. C.; Murray, C. B., Shape alloys of nanorods and nanospheres from self-assembly. *Nano letters* **2013,** *13* (10), 4980-4988.

26. Bruchez Jr, M.; Moronne, M.; Gin, P.; Weiss, S.; Alivisatos, A. P., Semiconductor nanocrystals as fluorescent biological labels. *science* **1998,** *281* (5385), 2013-2016.

27. Chan, W. C.; Nie, S., Quantum dot bioconjugates for ultrasensitive nonisotopic detection. *Science* **1998,** *281* (5385), 2016-2018.

28. Dubertret, B.; Skourides, P.; Norris, D. J.; Noireaux, V.; Brivanlou, A. H.; Libchaber, A., In vivo imaging of quantum dots encapsulated in phospholipid micelles. *Science* **2002,** *298* (5599), 1759-1762.

29. Norris, D. J.; Yao, N.; Charnock, F. T.; Kennedy, T. A., High-quality manganese-doped ZnSe nanocrystals. *Nano Letters* **2001,** *1* (1), 3-7.

30. Ekimov, A.; Kudryavtsev, I.; Ivanov, M.; Efros, A. L., Spectra and decay kinetics of radiative recombination in CdS microcrystals. *Journal of Luminescence* **1990,** *46* (2), 83-95.

31. Norris, D. J.; Efros, A. L.; Erwin, S. C., Doped nanocrystals. *Science* **2008,** *319* (5871), 1776-1779.

32. Schimpf, A. M.; Knowles, K. E.; Carroll, G. M.; Gamelin, D. R., Electronic doping and redox-potential tuning in colloidal semiconductor nanocrystals. *Accounts of chemical research* **2015,** *48* (7), 1929-1937.

33. Knowles, K. E.; Hartstein, K. H.; Kilburn, T. B.; Marchioro, A.; Nelson, H. D.; Whitham, P. J.; Gamelin, D. R., Luminescent colloidal semiconductor nanocrystals containing copper: synthesis, photophysics, and applications. *Chemical reviews* **2016,** *116* (18), 10820-10851.

34. Peng, X.; Manna, L.; Yang, W.; Wickham, J.; Scher, E.; Kadavanich, A.; Alivisatos, A. P., Shape control of CdSe nanocrystals. *Nature* **2000,** *404* (6773), 59-61.

35. Qu, L.; Peng, Z. A.; Peng, X., Alternative routes toward high quality CdSe nanocrystals. *Nano letters* **2001,** *1* (6), 333-337.

36. Peng, Z. A.; Peng, X., Formation of high-quality CdTe, CdSe, and CdS nanocrystals using CdO as precursor. *Journal of the American Chemical Society* **2001,** *123* (1), 183-184.

37. Battaglia, D.; Peng, X., Formation of high quality InP and InAs nanocrystals in a noncoordinating solvent. *Nano Letters* **2002,** *2* (9), 1027-1030.

38. Yu, W. W.; Peng, X., Formation of high-quality CdS and other II–VI semiconductor nanocrystals in noncoordinating solvents: tunable reactivity of monomers. *Angewandte Chemie International Edition* **2002,** *41* (13), 2368-2371.

39. Peng, X., Green chemical approaches toward high-quality semiconductor nanocrystals. *Chemistry–A European Journal* **2002,** *8* (2), 334-339.

40. Konstantatos, G., *Colloidal quantum dot optoelectronics and photovoltaics*. Cambridge University Press: 2013.

41. Protesescu, L.; Yakunin, S.; Bodnarchuk, M. I.; Krieg, F.; Caputo, R.; Hendon, C. H.; Yang, R. X.; Walsh, A.; Kovalenko, M. V., Nanocrystals of cesium lead halide perovskites (CsPbX3, X= Cl, Br, and I): novel optoelectronic materials showing bright emission with wide color gamut. *Nano letters* **2015,** *15* (6), 3692-3696.

42. Rabouw, F. T.; de Mello Donega, C., Excited-state dynamics in colloidal semiconductor nanocrystals. *Photoactive Semiconductor Nanocrystal Quantum Dots: Fundamentals and Applications* **2017**, 1-30.

43. Razavy, M., *Quantum theory of tunneling*. World Scientific: 2013.

44. Lifshitz, I. M.; Slyozov, V. V., The kinetics of precipitation from supersaturated solid solutions. *Journal of physics and chemistry of solids* **1961,** *19* (1-2), 35-50.

45. Wagner, C., Theorie der alterung von niederschlägen durch umlösen (Ostwald-reifung). *Zeitschrift für Elektrochemie, Berichte der Bunsengesellschaft für physikalische Chemie* **1961,** *65* (7-8), 581-591.

46. Park, J.; Joo, J.; Kwon, S. G.; Jang, Y.; Hyeon, T., Synthesis of monodisperse spherical nanocrystals. *Angewandte Chemie International Edition* **2007,** *46* (25), 4630-

4660.

47. LaMer, V. K.; Dinegar, R. H., Theory, production and mechanism of formation of monodispersed hydrosols. *Journal of the american chemical society* **1950,** *72* (11), 4847-4854.

48. Mullin, J. W., *Crystallization*. Elsevier: 2001.

49. Kwon, S. G.; Piao, Y.; Park, J.; Angappane, S.; Jo, Y.; Hwang, N.-M.; Park, J.-G.; Hyeon, T., Kinetics of monodisperse iron oxide nanocrystal formation by "heating-up" process. *Journal of the American Chemical Society* **2007,** *129* (41), 12571-12584.

50. Thanh, N. T.; Maclean, N.; Mahiddine, S., Mechanisms of nucleation and growth of nanoparticles in solution. *Chemical reviews* **2014,** *114* (15), 7610-7630.

51. Sugimoto, T., Preparation of monodispersed colloidal particles. *Advances in Colloid and Interface Science* **1987,** *28*, 65-108.

52. Wen, T.; Brush, L. N.; Krishnan, K. M., A generalized diffusion model for growth of nanoparticles synthesized by colloidal methods. *Journal of colloid and interface science* **2014,** *419*, 79-85.

53. Murray, C. B.; Kagan, C. R.; Bawendi, M. G., Synthesis and characterization of monodisperse nanocrystals and close-packed nanocrystal assemblies. *Annual review of materials science* **2000,** *30* (1), 545-610.

54. Murray, C. B. Synthesis and characterization of II-IV quantum dots and their assembly into 3D quantum dot superlattices. Massachusetts Institute of Technology, 1995.

55. Zlateva, G.; Zhelev, Z.; Bakalova, R.; Kanno, I., Precise size control and synchronized synthesis of six colors of CdSe quantum dots in a slow-increasing temperature gradient. *Inorganic chemistry* **2007,** *46* (16), 6212-6214.

56. Deng, Z.; Cao, L.; Tang, F.; Zou, B., A new route to zinc-blende CdSe nanocrystals: mechanism and synthesis. *The Journal of Physical Chemistry B* **2005,** *109* (35), 16671-16675.

57. Zhu, C.-N.; Jiang, P.; Zhang, Z.-L.; Zhu, D.-L.; Tian, Z.-Q.; Pang, D.-W., Ag2Se quantum dots with tunable emission in the second near-infrared window. *ACS applied*

materials & interfaces **2013,** *5* (4), 1186-1189.

58. Jiang, P.; Tian, Z.-Q.; Zhu, C.-N.; Zhang, Z.-L.; Pang, D.-W., Emission-tunable near-infrared Ag2S quantum dots. *Chemistry of Materials* **2012,** *24* (1), 3-5.

59. Lu, Y.; Yang, Y.; Guan, L.; Wang, D.; Zhao, J.; Yang, J.; Wei, Z.; Wang, F.; Yang, Z.; Li, X., Luminescent modulation of zinc sulphide nano-particles by thermal injection method. *Journal of Luminescence* **2020,** *226*, 117332.

60. Reiss, P., ZnSe based colloidal nanocrystals: synthesis, shape control, core/shell, alloy and doped systems. *New Journal of Chemistry* **2007,** *31* (11), 1843-1852.

61. Wang, X.; Ma, X.; Feng, X.; Zheng, Y., Controlled synthesis and characterization of ZnSe quantum dots. *Journal of Nanoscience and Nanotechnology* **2010,** *10* (11), 7812-7815.

62. Li, H.; Chen, D.; Li, L.; Tang, F.; Zhang, L.; Ren, J., Size-and shape-controlled synthesis of PbSe and PbS nanocrystals via a facile method. *CrystEngComm* **2010,** *12* (4), 1127-1133.

63. Acharya, K. P.; Khon, E.; O'Conner, T.; Nemitz, I.; Klinkova, A.; Khnayzer, R. S.; Anzenbacher, P.; Zamkov, M., Heteroepitaxial growth of colloidal nanocrystals onto substrate films via hot-injection routes. *ACS nano* **2011,** *5* (6), 4953-4964.

64. Hines, M. A.; Scholes, G. D., Colloidal PbS nanocrystals with size-tunable near-infrared emission: observation of post-synthesis self-narrowing of the particle size distribution. *Advanced Materials* **2003,** *15* (21), 1844-1849.

65. Murray, C. B.; Sun, S.; Gaschler, W.; Doyle, H.; Betley, T. A.; Kagan, C. R., Colloidal synthesis of nanocrystals and nanocrystal superlattices. *IBM Journal of Research and Development* **2001,** *45* (1), 47-56.

66. Song, W.-S.; Lee, H.-S.; Lee, J. C.; Jang, D. S.; Choi, Y.; Choi, M.; Yang, H., Amine-derived synthetic approach to color-tunable InP/ZnS quantum dots with high fluorescent qualities. *Journal of nanoparticle research* **2013,** *15*, 1-10.

67. Tietze, R.; Panzer, R.; Starzynski, T.; Guhrenz, C.; Frenzel, F.; Würth, C.; Resch-Genger, U.; Weigand, J. J.; Eychmüller, A., Synthesis of NIR-Emitting InAs-Based Core/Shell Quantum Dots with the Use of Tripyrazolylarsane as Arsenic Precursor.

Particle & Particle Systems Characterization **2018,** *35* (9), 1800175.

68. Nguyen, D.-C.; Ito, S.; Fukatsu, K.; Tanimoto, K., Making nanoparticle ink for compound solar cells. *SPIE Newsroom* **2013**.

69. Pradhan, N.; Efrima, S., Single-precursor, one-pot versatile synthesis under near ambient conditions of tunable, single and dual band fluorescing metal sulfide nanoparticles. *Journal of the American Chemical Society* **2003,** *125* (8), 2050-2051.

70. Van Embden, J.; Chesman, A. S.; Jasieniak, J. J., The heat-up synthesis of colloidal nanocrystals. *Chemistry of Materials* **2015,** *27* (7), 2246-2285.

71. Kwon, S. G.; Hyeon, T., Formation mechanisms of uniform nanocrystals via hot-injection and heat-up methods. *Small* **2011,** *7* (19), 2685-2702.

72. Nguyen, T.-D., From formation mechanisms to synthetic methods toward shape-controlled oxide nanoparticles. *Nanoscale* **2013,** *5* (20), 9455-9482.

73. Tao, A. R.; Habas, S.; Yang, P., Shape control of colloidal metal nanocrystals. *small* **2008,** *4* (3), 310-325.

74. Yang, Y. A.; Wu, H.; Williams, K. R.; Cao, Y. C., Synthesis of CdSe and CdTe nanocrystals without precursor injection. *Angewandte Chemie International Edition* **2005,** *44* (41), 6712-6715.

75. Cao, Y. C.; Wang, J., One-pot synthesis of high-quality zinc-blende CdS nanocrystals. *Journal of the American Chemical Society* **2004,** *126* (44), 14336-14337.

76. Zhao, T.; Oh, N.; Jishkariani, D.; Zhang, M.; Wang, H.; Li, N.; Lee, J. D.; Zeng, C.; Muduli, M.; Choi, H.-J., General synthetic route to high-quality colloidal III–V semiconductor quantum dots based on pnictogen chlorides. *Journal of the American Chemical Society* **2019,** *141* (38), 15145-15152.

77. Paredes, I. J.; Sahu, A., *Synthesis and Structure of Colloidal Quantum Dots*. American Chemical Society: 2023.

78. Reiss, P.; Carriere, M.; Lincheneau, C.; Vaure, L.; Tamang, S., Synthesis of semiconductor nanocrystals, focusing on nontoxic and earth-abundant materials. *Chemical reviews* **2016,** *116* (18), 10731-10819.

79. Beygi, H.; Sajjadi, S. A.; Babakhani, A.; Young, J. F.; van Veggel, F. C., Surface

chemistry of as-synthesized and air-oxidized PbS quantum dots. *Applied Surface Science* **2018,** *457*, 1-10.

80. Zherebetskyy, D.; Scheele, M.; Zhang, Y.; Bronstein, N.; Thompson, C.; Britt, D.; Salmeron, M.; Alivisatos, P.; Wang, L.-W., Hydroxylation of the surface of PbS nanocrystals passivated with oleic acid. *Science* **2014,** *344* (6190), 1380-1384.

81. Dong, C.; Liu, S.; Barange, N.; Lee, J.; Pardue, T.; Yi, X.; Yin, S.; So, F., Long-wavelength lead sulfide quantum dots sensing up to 2600 nm for short-wavelength infrared photodetectors. *ACS applied materials & interfaces* **2019,** *11* (47), 44451-44457.

82. Mamiyev, Z.; Balayeva, N. O., PbS nanostructures: A review of recent advances. *Materials Today Sustainability* **2023**, 100305.

83. Wells, H. L., Über die cäsium-und kalium-bleihalogenide. *Zeitschrift für anorganische Chemie* **1893,** *3* (1), 195-210.

84. Møller, C. K., A phase transition in cæsium plumbochloride. *Nature* **1957,** *180* (4593), 981-982.

85. Møller, C. K., Crystal structure and photoconductivity of caesium plumbohalides. *Nature* **1958,** *182* (4647), 1436-1436.

86. Mizusaki, J.; Arai, K.; Fueki, K., Ionic conduction of the perovskite-type halides. *Solid State Ionics* **1983,** *11* (3), 203-211.

87. Radhakrishna, S., Polarised luminescence from lead centers in cesium halides. *Journal of luminescence* **1976,** *12*, 409-411.

88. Nikl, M.; Polak, K.; Nitsch, K.; Pazzi, G.; Fabeni, P.; Gurioli, M., Optical properties of Pb2+-based aggregated phase in NaCl and CsCl alkali halide hosts. *Radiation effects and defects in solids* **1995,** *135* (1-4), 289-293.

89. Nikl, M.; Nitsch, K.; Polák, K.; Mihókova, E.; Zazubovich, S.; Pazzi, G.; Fabeni, P.; Salvini, L.; Aceves, R.; Barbosa-Flores, M., Quantum size effect in the excitonic luminescence of CsPbX3-like quantum dots in CsX (X= Cl, Br) single crystal host. *Journal of luminescence* **1997,** *72*, 377-379.

90. Aceves, R.; Babin, V.; Flores, M. B.; Fabeni, P.; Maaroos, A.; Nikl, M.; Nitsch, K.;

Pazzi, G.; Salas, R. P.; Sildos, I., Spectroscopy of CsPbBr3 quantum dots in CsBr: Pb crystals. *Journal of luminescence* **2001,** *93* (1), 27-41.

91. Kondo, S.; Sakai, T.; Tanaka, H.; Saito, T., Amorphization-induced strong localization of electronic states in CsPbBr 3 and CsPbCl 3 studied by optical absorption measurements. *Physical Review B* **1998,** *58* (17), 11401.

92. Kondo, S.; Takahashi, K.; Nakanish, T.; Saito, T.; Asada, H.; Nakagawa, H., High intensity photoluminescence of microcrystalline CsPbBr3 films: Evidence for enhanced stimulated emission at room temperature. *Current Applied Physics* **2007,** *7* (1), 1-5.

93. Kondo, S.; Saito, T.; Asada, H.; Nakagawa, H., Stimulated emission from microcrystalline CsPbBr3 films: Edge emission versus surface emission. *Materials Science and Engineering: B* **2007,** *137* (1-3), 156-161.

94. Weber, D., CH3NH3PbX3, ein Pb (II)-system mit kubischer perowskitstruktur/CH3NH3PbX3, a Pb (II)-system with cubic perovskite structure. *Zeitschrift für Naturforschung B* **1978,** *33* (12), 1443-1445.

95. Papavassiliou, G. C.; Pagona, G.; Karousis, N.; Mousdis, G. A.; Koutselas, I.; Vassilakopoulou, A., Nanocrystalline/microcrystalline materials based on lead-halide units. *Journal of Materials Chemistry* **2012,** *22* (17), 8271-8280.

96. Papavassiliou, G. C.; Pagona, G.; Mousdis, G. A.; Karousis, N., Enhanced phosphorescence from nanocrystalline/microcrystalline materials based on (CH3NH3)(1-naphthylmethyl ammonium) 2Pb2Cl7 and similar compounds. *Chemical Physics Letters* **2013,** *570*, 80-84.

97. Schmidt, L. C.; Pertegás, A.; González-Carrero, S.; Malinkiewicz, O.; Agouram, S.; Minguez Espallargas, G.; Bolink, H. J.; Galian, R. E.; Pérez-Prieto, J., Nontemplate synthesis of CH3NH3PbBr3 perovskite nanoparticles. *Journal of the American Chemical Society* **2014,** *136* (3), 850-853.

98. Protesescu, L.; Yakunin, S.; Kumar, S.; Bär, J.; Bertolotti, F.; Masciocchi, N.; Guagliardi, A.; Grotevent, M.; Shorubalko, I.; Bodnarchuk, M. I., Dismantling the "red wall" of colloidal perovskites: highly luminescent formamidinium and formamidinium–cesium lead iodide nanocrystals. *ACS nano* **2017,** *11* (3), 3119-3134.

99. Aygüler, M. F.; Weber, M. D.; Puscher, B. M.; Medina, D. D.; Docampo, P.; Costa, R. D., Light-emitting electrochemical cells based on hybrid lead halide perovskite nanoparticles. *The Journal of Physical Chemistry C* **2015,** *119* (21), 12047-12054.

100. Weidman, M. C.; Seitz, M.; Stranks, S. D.; Tisdale, W. A., Highly tunable colloidal perovskite nanoplatelets through variable cation, metal, and halide composition. *ACS nano* **2016,** *10* (8), 7830-7839.

101. Protesescu, L.; Yakunin, S.; Bodnarchuk, M. I.; Bertolotti, F.; Masciocchi, N.; Guagliardi, A.; Kovalenko, M. V., Monodisperse formamidinium lead bromide nanocrystals with bright and stable green photoluminescence. *Journal of the American Chemical Society* **2016,** *138* (43), 14202-14205.

102. Bertolotti, F.; Protesescu, L.; Kovalenko, M. V.; Yakunin, S.; Cervellino, A.; Billinge, S. J.; Terban, M. W.; Pedersen, J. S.; Masciocchi, N.; Guagliardi, A., Coherent nanotwins and dynamic disorder in cesium lead halide perovskite nanocrystals. *ACS nano* **2017,** *11* (4), 3819-3831.

103. Stoumpos, C. C.; Kanatzidis, M. G., The renaissance of halide perovskites and their evolution as emerging semiconductors. *Accounts of chemical research* **2015,** *48* (10), 2791-2802.

104. Stoumpos, C. C.; Malliakas, C. D.; Kanatzidis, M. G., Semiconducting tin and lead iodide perovskites with organic cations: phase transitions, high mobilities, and near-infrared photoluminescent properties. *Inorganic chemistry* **2013,** *52* (15), 9019-9038.

105. Saidaminov, M. I.; Mohammed, O. F.; Bakr, O. M., Low-dimensional-networked metal halide perovskites: the next big thing. *ACS Energy Letters* **2017,** *2* (4), 889-896.

106. Goldschmidt, V. M., Die gesetze der krystallochemie. *Naturwissenschaften* **1926,** *14* (21), 477-485.

107. Correa-Baena, J.-P.; Saliba, M.; Buonassisi, T.; Grätzel, M.; Abate, A.; Tress, W.; Hagfeldt, A., Promises and challenges of perovskite solar cells. *Science* **2017,** *358* (6364), 739-744.

108. Travis, W.; Glover, E.; Bronstein, H.; Scanlon, D.; Palgrave, R., On the application of the tolerance factor to inorganic and hybrid halide perovskites: a revised system. *Chemical science* **2016,** *7* (7), 4548-4556.

109. Li, C.; Lu, X.; Ding, W.; Feng, L.; Gao, Y.; Guo, Z., Formability of abx3 (x= f, cl, br, i) halide perovskites. *Acta Crystallographica Section B: Structural Science* **2008,** *64* (6), 702-707.

110. Huang, H.; Bodnarchuk, M. I.; Kershaw, S. V.; Kovalenko, M. V.; Rogach, A. L., Lead halide perovskite nanocrystals in the research spotlight: stability and defect tolerance. *ACS energy letters* **2017,** *2* (9), 2071-2083.

111. Motta, C.; El-Mellouhi, F.; Kais, S.; Tabet, N.; Alharbi, F.; Sanvito, S., Revealing the role of organic cations in hybrid halide perovskite CH3NH3PbI3. *Nature communications* **2015,** *6* (1), 7026.

112. Yin, W.-J.; Yang, J.-H.; Kang, J.; Yan, Y.; Wei, S.-H., Halide perovskite materials for solar cells: a theoretical review. *Journal of Materials Chemistry A* **2015,** *3* (17), 8926-8942.

113. Tao, S.; Schmidt, I.; Brocks, G.; Jiang, J.; Tranca, I.; Meerholz, K.; Olthof, S., Absolute energy level positions in tin-and lead-based halide perovskites. *Nature communications* **2019,** *10* (1), 2560.

114. Wang, Y.; Gould, T.; Dobson, J. F.; Zhang, H.; Yang, H.; Yao, X.; Zhao, H., Density functional theory analysis of structural and electronic properties of orthorhombic perovskite CH 3 NH 3 PbI 3. *Physical Chemistry Chemical Physics* **2014,** *16* (4), 1424-1429.

115. Sutherland, B. R.; Sargent, E. H., Perovskite photonic sources. *Nature Photonics* **2016,** *10* (5), 295-302.

116. Ning, C.-Z.; Dou, L.; Yang, P., Bandgap engineering in semiconductor alloy nanomaterials with widely tunable compositions. *Nature Reviews Materials* **2017,** *2* (12), 1-14.

117. Akkerman, Q. A.; D'Innocenzo, V.; Accornero, S.; Scarpellini, A.; Petrozza, A.; Prato, M.; Manna, L., Tuning the optical properties of cesium lead halide perovskite

nanocrystals by anion exchange reactions. *Journal of the American Chemical Society* **2015,** *137* (32), 10276-10281.

118.Dai, Z.; Ou, Q.; Wang, C.; Si, G.; Shabbir, B.; Zheng, C.; Wang, Z.; Zhang, Y.; Huang, Y.; Dong, Y., Capillary-bridge mediated assembly of aligned perovskite quantum dots for high-performance photodetectors. *Journal of Materials Chemistry C* **2019,** *7* (20), 5954-5961.

119.Perovskite-Silicon, F.-T., Development of High Efficiency Four-Terminal Perovskite-Silicon Tandems. *Ann Arbor* **2017,** *1001*, 48106-41346.

120. De Wolf, S.; Holovsky, J.; Moon, S.-J.; Loper, P.; Niesen, B.; Ledinsky, M.; Haug, F.-J.; Yum, J.-H.; Ballif, C., Organometallic halide perovskites: sharp optical absorption edge and its relation to photovoltaic performance. *The journal of physical chemistry letters* **2014,** *5* (6), 1035-1039.

121. Gualdrón-Reyes, A. F.; Masi, S.; Mora-Seró, I., Progress in halide-perovskite nanocrystals with near-unity photoluminescence quantum yield. *Trends in Chemistry* **2021,** *3* (6), 499-511.

122. Rainò, G.; Yazdani, N.; Boehme, S. C.; Kober-Czerny, M.; Zhu, C.; Krieg, F.; Rossell, M. D.; Erni, R.; Wood, V.; Infante, I., Ultra-narrow room-temperature emission from single CsPbBr3 perovskite quantum dots. *Nature communications* **2022,** *13* (1), 2587.

123. Su, Y.; Chen, X.; Ji, W.; Zeng, Q.; Ren, Z.; Su, Z.; Liu, L., Highly controllable and efficient synthesis of mixed-halide CsPbX3 (X= Cl, Br, I) perovskite QDs toward the tunability of entire visible light. *ACS applied materials & interfaces* **2017,** *9* (38), 33020-33028.

124. Queisser, H. J.; Haller, E. E., Defects in semiconductors: some fatal, some vital. *Science* **1998,** *281* (5379), 945-950.

125. Kang, J.; Wang, L.-W., High defect tolerance in lead halide perovskite CsPbBr3. *The journal of physical chemistry letters* **2017,** *8* (2), 489-493.

126. Guo, Y.; Wang, Q.; Saidi, W. A., Structural stabilities and electronic properties of high-angle grain boundaries in perovskite cesium lead halides. *The Journal of*

Physical Chemistry C **2017,** *121* (3), 1715-1722.

127. ten Brinck, S.; Infante, I., Surface termination, morphology, and bright photoluminescence of cesium lead halide perovskite nanocrystals. *ACS Energy Letters* **2016,** *1* (6), 1266-1272.

128. Brandt, R. E.; Stevanović, V.; Ginley, D. S.; Buonassisi, T., Identifying defect-tolerant semiconductors with high minority-carrier lifetimes: beyond hybrid lead halide perovskites. *Mrs Communications* **2015,** *5* (2), 265-275.

129. Akkerman, Q. A.; Rainò, G.; Kovalenko, M. V.; Manna, L., Genesis, challenges and opportunities for colloidal lead halide perovskite nanocrystals. *Nature materials* **2018,** *17* (5), 394-405.

130. Kovalenko, M. V.; Protesescu, L.; Bodnarchuk, M. I., Properties and potential optoelectronic applications of lead halide perovskite nanocrystals. *Science* **2017,** *358* (6364), 745-750.

131. Zhu, H.; Miyata, K.; Fu, Y.; Wang, J.; Joshi, P. P.; Niesner, D.; Williams, K. W.; Jin, S.; Zhu, X.-Y., Screening in crystalline liquids protects energetic carriers in hybrid perovskites. *Science* **2016,** *353* (6306), 1409-1413.

132. Bakulin, A. A.; Selig, O.; Bakker, H. J.; Rezus, Y. L.; Müller, C.; Glaser, T.; Lovrincic, R.; Sun, Z.; Chen, Z.; Walsh, A., Real-time observation of organic cation reorientation in methylammonium lead iodide perovskites. *The journal of physical chemistry letters* **2015,** *6* (18), 3663-3669.

133. Walsh, A.; Zunger, A., Instilling defect tolerance in new compounds. *Nature materials* **2017,** *16* (10), 964-967.

134. Shi, J.; Zhang, H.; Li, Y.; Jasieniak, J. J.; Li, Y.; Wu, H.; Luo, Y.; Li, D.; Meng, Q., Identification of high-temperature exciton states and their phase-dependent trapping behaviour in lead halide perovskites. *Energy & Environmental Science* **2018,** *11* (6), 1460-1469.

135. Lim, J.; Kober-Czerny, M.; Lin, Y.-H.; Ball, J. M.; Sakai, N.; Duijnstee, E. A.; Hong, M. J.; Labram, J. G.; Wenger, B.; Snaith, H. J., Long-range charge carrier mobility in metal halide perovskite thin-films and single crystals via transient photo-

conductivity. *Nature Communications* **2022,** *13* (1), 4201.

136. Dong, Q.; Fang, Y.; Shao, Y.; Mulligan, P.; Qiu, J.; Cao, L.; Huang, J., Electron-hole diffusion lengths> 175 μm in solution-grown CH3NH3PbI3 single crystals. *Science* **2015,** *347* (6225), 967-970.

137. Xing, G.; Mathews, N.; Sun, S.; Lim, S. S.; Lam, Y. M.; Grätzel, M.; Mhaisalkar, S.; Sum, T. C., Long-range balanced electron-and hole-transport lengths in organic-inorganic CH3NH3PbI3. *Science* **2013,** *342* (6156), 344-347.

138. Shamsi, J.; Urban, A. S.; Imran, M.; De Trizio, L.; Manna, L., Metal halide perovskite nanocrystals: synthesis, post-synthesis modifications, and their optical properties. *Chemical reviews* **2019,** *119* (5), 3296-3348.

139. Dey, A.; Ye, J.; De, A.; Debroye, E.; Ha, S. K.; Bladt, E.; Kshirsagar, A. S.; Wang, Z.; Yin, J.; Wang, Y., State of the art and prospects for halide perovskite nanocrystals. *ACS nano* **2021,** *15* (7), 10775-10981.

140. Huang, H.; Zhao, F.; Liu, L.; Zhang, F.; Wu, X.-g.; Shi, L.; Zou, B.; Pei, Q.; Zhong, H., Emulsion synthesis of size-tunable CH3NH3PbBr3 quantum dots: an alternative route toward efficient light-emitting diodes. *ACS applied materials & interfaces* **2015,** *7* (51), 28128-28133.

141. Li, Y.; Huang, H.; Xiong, Y.; Kershaw, S. V.; Rogach, A. L., Revealing the formation mechanism of CsPbBr3 perovskite nanocrystals produced via a slowed-down microwave-assisted synthesis. *Angewandte Chemie International Edition* **2018,** *57* (20), 5833-5837.

142. Yu, J.; Liu, G.; Chen, C.; Li, Y.; Xu, M.; Wang, T.; Zhao, G.; Zhang, L., Perovskite CsPbBr 3 crystals: growth and applications. *Journal of Materials Chemistry C* **2020,** *8* (19), 6326-6341.

143. Blancon, J.-C.; Even, J.; Stoumpos, C. C.; Kanatzidis, M. G.; Mohite, A. D., Semiconductor physics of organic–inorganic 2D halide perovskites. *Nature nanotechnology* **2020,** *15* (12), 969-985.

144. Chen, W.; Hao, J.; Hu, W.; Zang, Z.; Tang, X.; Fang, L.; Niu, T.; Zhou, M., Enhanced stability and tunable photoluminescence in perovskite CsPbX3/ZnS quantum

dot heterostructure. *Small* **2017,** *13* (21), 1604085.

145. Roman, B. J.; Otto, J.; Galik, C.; Downing, R.; Sheldon, M., Au exchange or Au deposition: dual reaction pathways in Au–CsPbBr3 heterostructure nanoparticles. *Nano letters* **2017,** *17* (9), 5561-5566.

146. Liu, Y.; Yang, Y.; Chen, P.; Shan, Y.; Li, Y.; Shi, J.; Hou, J.; Zhang, N.; Zhao, G.; Xu, J., Nano Ball-Milling Using Titania Nanoparticles to Anchor Cesium Lead Bromine Nanocrystals and Energy Transfer Characteristics in TiO2@ CsPbBr3 Architecture. *Small* **2020,** *16* (40), 2004126.

147. Yang, Y.; Li, Q.; Liu, Y.; Cong, R.; Sun, Y.; Hou, J.; Ge, M.; Shi, J.; Zhang, F.; Zhao, G., Magenta-emitting cesium lead halide nanocrystals encapsulated in dimethicone for white light-emitting diodes. *ACS Applied Nano Materials* **2020,** *3* (5), 4886-4892.

148. He, X.; Yu, C.; Yu, M.; Lin, J.; Li, Q.; Fang, Y.; Liu, Z.; Xue, Y.; Huang, Y.; Tang, C., Synthesis of perovskite CsPbBr3 quantum dots/porous boron nitride nanofiber composites with improved stability and their reversible optical response to ammonia. *Inorganic Chemistry* **2019,** *59* (2), 1234-1241.

149. Xu, X.; Wang, X., Perovskite nano-heterojunctions: synthesis, structures, properties, challenges, and prospects. *Small Structures* **2020,** *1* (1), 2000009.

150. Li, Y.; Ding, T.; Luo, X.; Chen, Z.; Liu, X.; Lu, X.; Wu, K., Biexciton Auger recombination in mono-dispersed, quantum-confined CsPbBr 3 perovskite nanocrystals obeys universal volume-scaling. *Nano Research* **2019,** *12*, 619-623.

151. Shi, Z.; Muhammad, S.; Deng, L.; Liu, Z.; Bi, L.; Zhang, L.; Zhang, L.; Zhou, P.; Chen, H.; Lu, H., Magnetic-brightening and control of dark exciton in CsPbBr3 perovskite. *Science China Materials* **2020,** (8), 1503-1509.

152. Mondal, N.; De, A.; Das, S.; Paul, S.; Samanta, A., Ultrafast carrier dynamics of metal halide perovskite nanocrystals and perovskite-composites. *Nanoscale* **2019,** *11* (20), 9796-9818.

153. Ross, R. T.; Nozik, A. J., Efficiency of hot-carrier solar energy converters. *Journal of Applied Physics* **1982,** *53* (5), 3813-3818.

154. Sarkar, S.; Ravi, V. K.; Banerjee, S.; Yettapu, G. R.; Markad, G. B.; Nag, A.; Mandal, P., Terahertz spectroscopic probe of hot electron and hole transfer from colloidal CsPbBr3 perovskite nanocrystals. *Nano letters* **2017,** *17* (9), 5402-5407.

155. Li, M.; Bhaumik, S.; Goh, T. W.; Kumar, M. S.; Yantara, N.; Grätzel, M.; Mhaisalkar, S.; Mathews, N.; Sum, T. C., Slow cooling and highly efficient extraction of hot carriers in colloidal perovskite nanocrystals. *Nature communications* **2017,** *8* (1), 14350.

156. Wang, S.; Bi, C.; Portniagin, A.; Yuan, J.; Ning, J.; Xiao, X.; Zhang, X.; Li, Y. Y.; Kershaw, S. V.; Tian, J., CsPbI3/PbSe heterostructured nanocrystals for high-efficiency solar cells. *ACS Energy Letters* **2020,** *5* (7), 2401-2410.

157. Gong, M.; Alamri, M.; Ewing, D.; Sadeghi, S. M.; Wu, J. Z., Localized surface plasmon resonance enhanced light absorption in AuCu/CsPbCl3 core/shell nanocrystals. *Advanced Materials* **2020,** *32* (26), 2002163.

158. Wan, Q.; Zheng, W.; Zou, C.; Carulli, F.; Zhang, C.; Song, H.; Liu, M.; Zhang, Q.; Lin, L. Y.; Kong, L., Ultrathin Light-Emitting Diodes with External Efficiency over 26% Based on Resurfaced Perovskite Nanocrystals. *ACS Energy Letters* **2023,** *8* (2), 927-934.

159. Das, R.; Patra, A.; Dutta, S. K.; Shyamal, S.; Pradhan, N., Facets-Directed Epitaxially Grown Lead Halide Perovskite-Sulfobromide Nanocrystal Heterostructures and Their Improved Photocatalytic Activity. *Journal of the American Chemical Society* **2022,** *144* (40), 18629-18641.

Chapter 2 Characterization techniques and principles

2.1 Photoluminescence spectrum (PL)

The fluorescence data presented in the paper, including intensity-dependent fluorescence, transient fluorescence, and fluorescence quenching, were recorded using the fluorescence system from TOKYO INSTRUMENT, INC. The experimental setup, including digital images and schematic diagrams of the instrument structure.

A pulsed diode laser at 473 nm wavelength (with a pulse width of 90 ps, a repetition rate of up to 100 MHz, and a peak power of 4 mW) was employed as the excitation light source. The excitation intensity was adjusted using a tunable circular neutral density filter. Fluorescence detection was carried out using a photomultiplier tube (PMT) and a Time-Correlated Single Photon Counting (TCSPC) module.

2.2 Time-resolved photoluminescence spectrum (TRPL)

Transient fluorescence spectra, also known as Time-Resolved Photoluminescence spectra (TRPL), can be employed to characterize the excited state lifetime of perovskite materials. The excited state lifetime refers to the time required for excitons/free carriers generated after light or electron excitation in perovskite to recombine through various channels. It represents a time-averaged statistical concept and can be precisely studied

using TRPL techniques.

2.3 Photoluminescence quantum yield (PLQY)

Photoluminescence Quantum Yield (PLQY) measurement is a method used to determine the efficiency of light emission (energy) concerning the absorbed light in a material, indicating the material's luminescent efficiency. In this thesis, we employed the Absolute PLQY measurement system from Hamamatsu Corporation, Japan, utilizing the integrating sphere method. The PLQY of the halide perovskite nanocrystals we synthesized was measured at an excitation power of 0.1 mW.

2.4 Ultraviolet-visible near-infrared absorption spectrum (UV-Vis-NIR)

Ultraviolet-visible-near-infrared (UV-Vis-NIR) spectroscopy stands as a widely employed technique for measuring material absorption or reflectance spectra. Its measurement range spans from 200 nanometers to 2000 nanometers. According to the formula $\frac{\hbar c}{\lambda} = E_1 - E_0$ (where $\hbar$ is the Planck constant, c is the speed of light in a vacuum), absorption occurs when the energy of an electron transitioning from the system's lower energy level (E_0) to the higher energy level (E_1) equals the energy of the incident photons. Thus, the study of absorption spectra provides insights into the structures, motions, and interactions of atoms, molecules, and many other substances with electromagnetic fields or particles. In semiconductor material research, absorption spectra often exhibit broad and indistinct peaks, stemming from factors like the overlap

of electronic transitions and material heterogeneity. Therefore, the analysis of semiconductor absorption spectra often necessitates specialized methods. For instance, Tauc plots are commonly utilized to determine the bandgap of semiconductors[1]. Additionally, the use of the Elliott formula allows the separation of excitonic contributions and contributions from continuous band-to-band absorption, yielding information on bandgaps and exciton binding energies[2]. Furthermore, derivative absorption spectra are extensively used for analyzing the complex absorption bands of materials[3-4]. By calculating the derivative of the absorption curve with respect to wavelength, this method enables the resolution of fine structures in electronic signals, eliminating linear background functions and segregating overlapping transition absorptions[4]. Particularly in quantum-constrained systems, the minima in the second derivative of the derivative absorption spectrum are considered directly related to electronic state levels[5-6].In this paper, we delve into the study of band edges and high-energy electronic states of perovskite nanocrystal heterostructures through the analysis of absorption and derivative absorption spectra. These spectra were measured using a UV-Vis-NIR spectrophotometer (JASCO, V-670), ensuring precision and reliability in the experimental approach.

2.5 Fourier transform infrared spectroscopy (FT-IR)

Fourier Transform Infrared Spectroscopy (FTIR) is a technique that utilizes the absorption of infrared light due to molecular vibrations and rotations to identify

molecular composition, structure, or quantitatively determine their content. Furthermore, FTIR is used to analyze chemical interactions between molecules by examining changes in characteristic peaks related to molecular vibrations and rotations. Typically, an FTIR system comprises an infrared light source, a spectrometer, a detector, and Fast Fourier Transform (FFT) algorithms. FTIR sampling methods include transmission, diffuse reflection, specular reflection, and attenuated total reflection (ATR). Among these methods, ATR mode is widely used in FTIR spectroscopy as it allows for rapid and easy measurement of various sample types, including liquids, solids, powders, semi-solids, and pastes, offering excellent sensitivity. In this thesis, we employed the ATR mode to measure the FTIR spectra of perovskite nanocrystal heterostructures (Nicolet 6700 FTIR), enabling the analysis of interactions between ligands and nanocrystals.

2.6 X-ray diffraction (XRD)

X-ray Diffraction (XRD) is a technique employed to scrutinize the atomic or molecular structure of materials, unraveling essential details about their composition, lattice parameters, orientation, and crystal phases. This method capitalizes on the intriguing interplay between monochromatic X-rays and the crystalline sample. When a beam of X-rays is directed at the sample, the sample disperses the incident X-rays following Bragg's law:

$$n\lambda = 2dsin\theta \quad (2\text{-}1)$$

Here,λsignifies the wavelength of the incident X-rays, n denotes the order of

diffraction peaks, d represents the spacing between lattice planes, and θ stands for the angle of the incident X-rays. Constructive interference occurs when the difference in the paths of X-rays scattered on adjacent crystal planes equals an integral multiple of the wavelength. The resulting interplanar spacing (d) provides valuable insights into the material's crystal structure. Among the array of XRD methodologies, X-ray powder diffraction emerges as a potent tool, especially for analyzing samples comprising numerous crystalline or non-crystalline particles exhibiting random orientation. Hence, in this study, the Rigaku TTR-III powder X-ray diffraction system was harnessed to discern the crystalline phases of all the samples. Quantum dot solutions were meticulously deposited onto glass substrates and allowed to air dry at room temperature. This meticulous procedure was repeated some times to ensure the formation of a suitably thick liquid film for analysis.

2.7 X-Ray photoelectron spectrum (XPS)

X-ray Photoelectron Spectroscopy (XPS) stands as a surface analysis technique, providing crucial information about a material's elemental composition and electronic states. When subjected to a beam of X-rays, electrons escape from the atoms near the sample surface (within 0-10 nanometers). Through XPS measurements, both qualitative and quantitative analyses of elements become possible. Analyzing XPS spectra yields valuable insights into a material's chemical bonds, coordination, binding energy, and surface morphology. The binding energy of elements can be determined by the following equation:

$$E_B = h\upsilon - E_k - \phi \qquad (2\text{-}2)$$

Here, E_B represents the binding energy of the element, $h\upsilon$ denotes the energy of the incident X-rays, E_k is the kinetic energy of the photoelectron, and ϕ stands for the work function. In this study, all XPS data for nano perovskite heterojunctions were recorded using an X-ray photoelectron spectrometer (JPS-9200, JEOL Corporation, Japan).

2.8 Grazing incidence wide angle X-ray scattering and small angle X-ray scattering (GI-WAXs and GI-SAXs)

As shown in Figure 2-1, Grazing Incidence Wide Angle X-ray Scattering (GI-WAXs) and Grazing Incidence Small Angle X-ray Scattering (GI-SAXs) operate on the fundamental principles of XRD and adhere to Bragg's diffraction formula[7]. However, GI-WAXs and GI-SAXs offer more comprehensive material structural information than XRD. In addition to characterizing the material's structure, they provide details about the arrangement of nanostructures, average distances between nanocrystals, and other essential information.

In both GI-WAXs and GI-SAXs, X-rays are incident at a grazing angle onto the sample surface, and the scattered X-rays are collected in the reflection direction. The incident angle is typically chosen slightly larger than the critical angle of the material to ensure sufficient X-ray scattering and enhance the signal intensity. This setup is particularly crucial for weakly scattering samples like organic films and ultra-thin

quantum dot films to achieve a good signal-to-noise ratio. Both GI-WAXs and GI-SAXs typically require high-intensity synchrotron radiation as the light source.

For GIWAXS, the distance between the detector and the sample is relatively short (typical value: 20 cm), with a detection length scale ranging from ~0.01 nm to ~1 nm, mainly used for analyzing the sample's crystalline structure. In GISAXS, the detector is positioned farther from the sample (typical value: 2 meters), and measurements are made in the scale range of 1 nm to 100 nm, primarily used for analyzing the arrangement of material nanostructures.

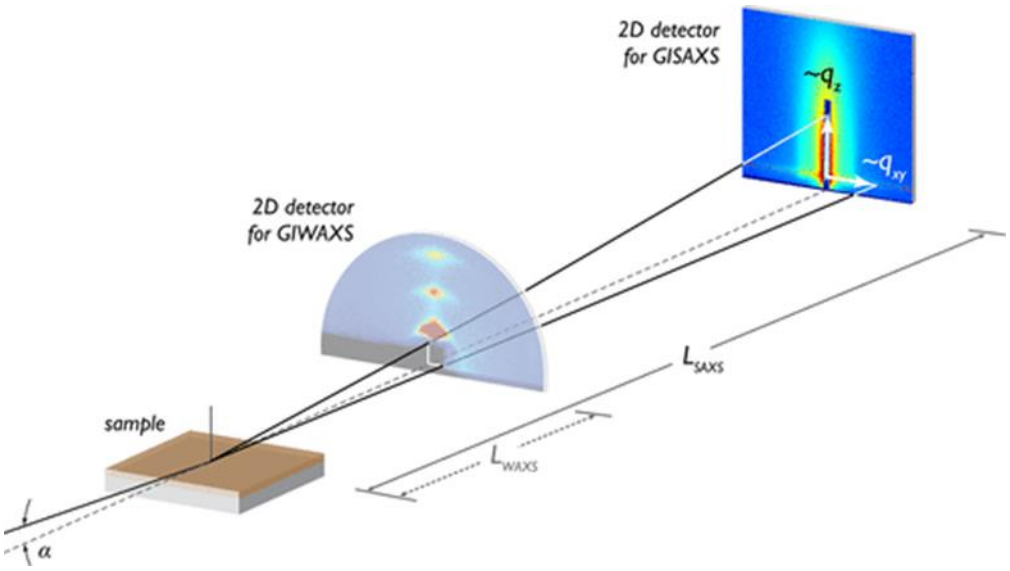

Figure 2-1. Schematic for grazing incidence small-angle X-ray scattering (GISAXS), with a relative comparison to GIWAXS[7].

2.9 Transient absorption spectrum (TAS)

Femtosecond Transient Absorption (TA) spectroscopy is a widely used femtosecond time-resolved pump-probe technique. This method utilizes a pump pulse laser to excite the sample and induce changes in its chemical or physical properties,

often resulting in the generation of new absorption species, namely transient components. Subsequently, another probe pulse is employed to detect the changes in the sample's absorbance after excitation, known as transient absorption. By varying the delay between the pump and probe light, different time-resolved spectra of the sample can be obtained before and after optical excitation. Through analysis, spectral and kinetic information corresponding to the generation and decay of transient components can be derived.

Femtosecond time-resolved spectroscopy captures a significant portion of information about electronic excited states, making it widely applicable in studies involving energy transfer, charge transfer, dynamic coupling of electronic and nuclear states, and conformational relaxation, among other phenomena. This section briefly outlines the fundamental principles of TA technique and its applications in investigating charge carrier transfer dynamics.

2.9.1 Experimental Setup of TA Spectroscopy

Figure 2-2 provides a simplified schematic of the femtosecond time-resolved Laser-Induced Transient Absorption (TA) measurement system employed in this study. The system utilizes a solid-state Ti-doped sapphire regenerative amplifier femtosecond laser system (CPA-2010, Clark-MXR Inc.) equipped with a regenerative amplifier. The laser operates at a fundamental wavelength of 775 nanometers, delivering pulses lasting 120 femtoseconds at a rate of 1 kHz.

This optical setup is divided into two main paths: the pump path and the detection

path. Initially, the fundamental light passes through an optical wedge, generating both detection light and the light needed to create the pump pulse through total internal reflection within the wedge.

In the pump path, the fundamental light is delayed and then frequency-tuned using an Optical Parametric Amplifier (OPA) to generate the specific pump light required for the experiment. After filtering out unwanted scattered light, the pump light is appropriately attenuated and focused onto the sample for excitation. To prevent interference with the detection light, the excitation light passing through the sample is selectively blocked.

In the detection path, the delayed fundamental light is focused onto a sapphire crystal, generating a broad-spectrum supercontinuum white light. This white light, serving as the detection light, undergoes polarization adjustments and focal length tuning through optical components like a half-wave plate, a variable aperture, and a convex lens. An achromatic lens then collects the white light, and a filter removes any remaining 780-nanometer fundamental light.

The collected white light is reflected from both surfaces of the optical wedge, producing two nearly identical spectra: the signal light and the reference light. Both beams focus on the sample, overlapping with the pump light within it. Subsequently, these two beams of white light, after passing through the sample, are collected by optical fibers and directed to a spectrometer equipped with a CCD for spectral analysis. The shutter and optical splitter in the setup ensure synchronized control of the laser and detector, enabling precise data acquisition.

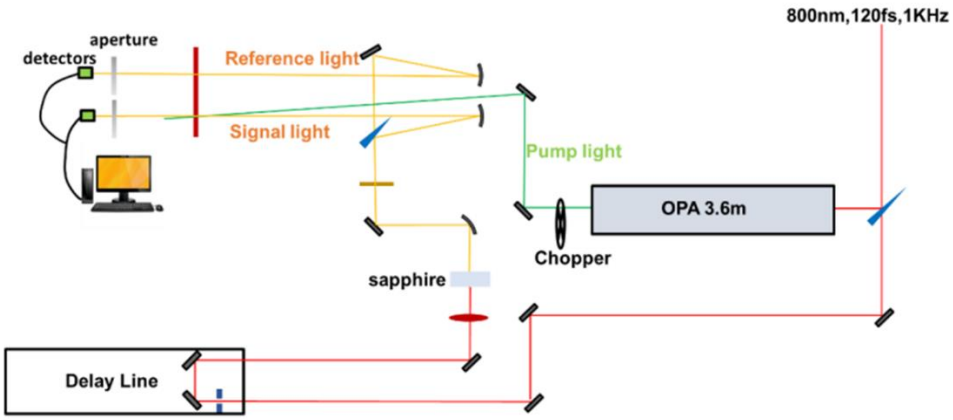

Figure 2-2. The optical path diagram of our femtosecond TA spectroscopy measurement system.

2.9.2 Basic principles of TA Spectroscopy

The absorption of light by samples can be described using either transmittance (T) or optical density (OD):

$$T = \frac{I}{I_0} \times 100\% \tag{2-3}$$

$$OD = lg\frac{I_0}{I} = \varepsilon lc \tag{2-4}$$

In here, I_0 and I represent the intensity of the white light before and after passing through the sample, respectively. ε, l, and c represent the molar absorptivity, sample thickness, and sample concentration, respectively. In the TA experiment, the observed final signal is the difference in the optical density (ΔOD) of the sample for the detecting light and the reference light. It can be expressed as the difference in optical density when the sample is exposed to the pump light ($OD_{pump-on}$) and when it is not ($OD_{pump-off}$), i.e.,

$$\Delta OD = OD_{pump-on} - OD_{pump-off} \tag{2-5}$$

Assuming the sample's absorption in the ground state is $OD_{pump-off} = \varepsilon lc$, the sample's absorption under the pump light can be calculated as $OD_{pump-on} = \varepsilon l(c - c^*) + \varepsilon^* lc^*$, where a portion of the sample (c^*) is excited to the excited state. Consequently, $\Delta OD = (\varepsilon - \varepsilon^*)lc^*$. It is evident that ΔOD is directly proportional to the concentration of the transient component c^*. Thus, changes in the transient spectrum can be observed to deduce variations in the transient component.

In this formula, the molar extinction coefficient ε is a function of wavelength, and the concentration c is a function of time. $\Delta OD(\lambda, t)$ represents a function varying with both wavelength and time, making the TA spectrum a two-dimensional matrix.

From a spectroscopic perspective, the transient component's spectrum reflects two aspects: $\varepsilon^*(\lambda)$ and $\varepsilon(\lambda)$. $\varepsilon^*(\lambda)$ is the molar absorptivity when the sample is in the excited state, known as excited-state absorption, while $\varepsilon(\lambda)$ represents the molar absorptivity when the sample is in the ground state. The negative signal is termed ground-state bleach (GSB), usually attributed to forbidden transitions in the ground state. Simultaneously, the positive signal is called photoinduced absorption, typically attributed to enhanced absorption in the excited state. If the excitation radiation occurs when the sample is excited, the original $\Delta OD(\lambda, t)$ needs to be rewritten as $\Delta OD(\lambda, t) = (\varepsilon^*(\lambda) - \varepsilon(\lambda) - \varepsilon^*_{se}(\lambda)lc^*(t))$. The transient component's spectrum is a superposition of excited-state absorption, ground-state bleach, and stimulated emission. Furthermore, time-resolved kinetics of $\Delta OD(\lambda)$ are obtained in time-resolved absorption spectroscopy by controlling the relative time delay between the pump light and the probing light passing through the sample.

In practical experiments, TA spectroscopy measurements and analyses are more intricate. A deep understanding of material properties, coupled with scientific measurement techniques and data analysis methods, is essential.

2.10 Transmission electron microscopy (TEM)

Microscopes have significantly enhanced humanity's capacity to observe minute entities. According to the Rayleigh Criterion, the resolution (dn) of a microscope is defined as $0.61 \sin \lambda\alpha$, where λ is the wavelength, n is the refractive index between the lens and the object medium, and α is half the aperture angle. It is evident that shorter wavelengths lead to higher microscope resolution[8]. In the era of optical microscopy, to achieve higher resolution, ultraviolet light with shorter wavelengths than visible light and a refractive index (n) of 1.66 for bromobenzene were employed, yet the resolution remained around 200 nm. Quantum mechanics, acknowledging the wave-particle duality, indicates that high-energy electron beams behave both as particles and waves, with shorter wavelengths corresponding to higher energy. Considering relativistic effects, for instance, a 100 keV electron beam can have a wavelength of 0.037 Å, and a 300 keV electron beam can reach 0.019 Å. In principle, transmission electron microscopy (TEM) can achieve resolutions far superior to optical microscopy, as depicted in Figure 2-3 b. After over 80 years of development, modern TEM has achieved resolutions as fine as 1.9 Å, and the latest TEMs, equipped with aberration correctors, can reach resolutions of 50 pm. Today, TEM has evolved into a versatile

experimental platform capable of observing atomic structures, deducing crystal structures through selected-area electron diffraction, and determining the chemical composition based on X-ray energy dispersive spectroscopy and electron energy loss spectroscopy[9]. Since its invention, TEM has continually driven breakthroughs in materials science[10]. For instance, in 1956, researchers at the University of Cambridge, including Hirsch, Whelan, and Howie, captured the diffraction contrast image of dislocation for the first time, sparking a research surge in metal dislocations and defects. In 1982, Israeli scientist Schetman, utilizing selected-area diffraction, discovered quasicrystals, earning the Nobel Prize in 2011. The advancement of high-resolution TEM also facilitated the discovery of C_{60} and carbon nanotubes, ushering in a new era in nanotechnology.

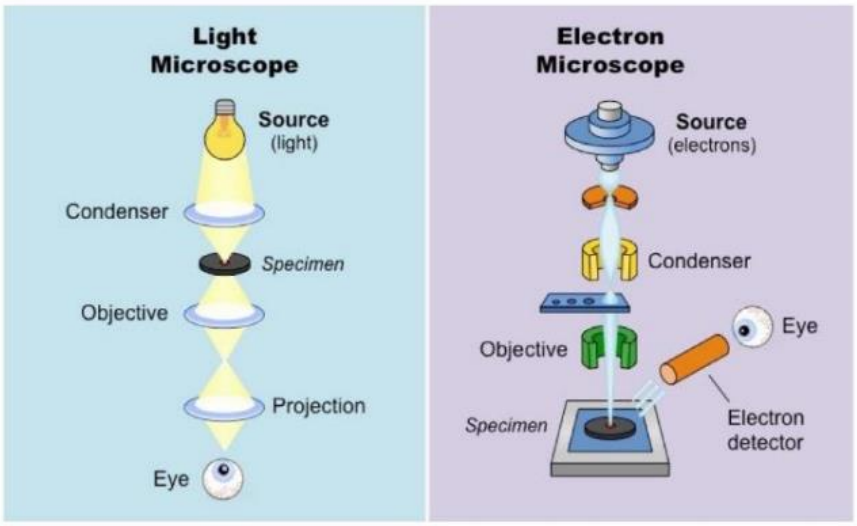

Figure 2-3. Schematic of a Light Microscope Versus a Transmission Electron Microscope (TEM)[11].

2.10.1 Transmission Electron Microscope Basic Structure and Imaging Principles

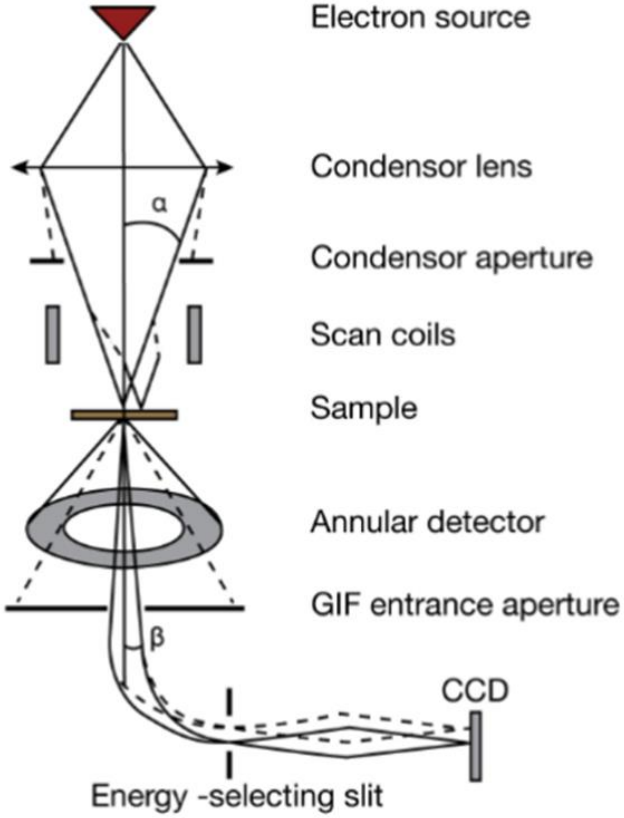

Figure 2-4. Schematic diagram of a STEM instrument[11].

The principle of transmission electron microscope (TEM) imaging, as illustrated in Figure 2-4, can be analogized to an optical microscope. In this process, an electron beam is emitted from the electron gun, undergoes acceleration in the acceleration tube, and is then filtered by a monochromator. The focused electron beam is brought to the front focal point of the objective lens magnetic field, where it is directed onto the sample in parallel beam mode. Consequently, the outgoing electron beam carries structural

information from the specimen and is imaged by the magnetic field behind the objective lens. Due to interference from the objective lens spherical aberration, the image requires correction through an objective lens spherical aberration corrector. The corrected image is finally magnified and projected onto a fluorescent screen or a CCD camera through a projection lens. The electron gun, typically located at the top, is the device responsible for generating electrons and can be categorized into thermionic emission and field emission types. The thermionic emission gun often employs a tungsten filament or lanthanum hexaboride (LaB_6). The field emission gun utilizes tunneling effect, allowing electrons from the metal interior to be emitted from the metal surface under the influence of a strong electric field. To focus the cathode field, the metal is shaped into a sharp form with a curvature radius less than 100 nm. If this sharp emitter operates at room temperature, it is a cold cathode, characterized by low energy dispersion (0.3 ~ 0.5 eV) but with high emission noise, necessitating periodic treatment of adsorbed molecules at the tip. If the emitter operates while heated, it is a hot cathode or a Schottky-type emitter, exhibiting larger energy dispersion (0.6 ~ 0.8 eV) but with low emission noise and no ion adsorption issues. Compared to thermionic emission guns, field emission guns offer 100 times higher brightness, have a very small light source size, excellent coherence, and enhance the information resolution of the TEM.

The condenser lens, objective lens, projection lens, and spherical aberration corrector are essentially magnetic lenses. These magnetic lenses can be likened to optical lenses. According to electromagnetic principles, a strong magnetic field is generated when a large current passes through a coil. To enhance excitation and narrow

the magnetic field range, an outer coil is covered with a soft magnetic material iron shell containing a circular slit. This way, the magnetic induction lines pass through the soft magnetic material until they interact with the electron beam at the slit. In the objective lens, it may be necessary to add a conical convex polepiece to further strengthen the concentrated magnetic field. A magnetic lens is always a converging lens, and its focal length (f) can be adjusted by controlling the current size.

To ensure stable electron emission and prevent scattering by air molecules while avoiding sample contamination, a mechanical pump, oil diffusion pump, and sputter ion pump are necessary for maintaining high vacuum in the electron microscope. To maintain stable electron emission and prevent discharge in the acceleration tube, an ion pump is employed to extract the chamber, achieving ultra-high vacuum (10^{-5} Pa). An intermediate chamber is placed between the acceleration tube and the lens barrel to achieve a gradient vacuum[12]. The power supply system primarily provides stable acceleration voltage and magnetic lens current. To minimize chromatic aberration, the acceleration voltage is stabilized at 10^{-6} /min. The objective lens is the most important lens, and its current is stabilized at $1\sim2\times10^{-6}$ /min.

2.10.2 Principle of aberration and spherical aberration correction

In optical systems, the combination of convex and concave lenses, along with changes in the shape of refractive surfaces, could be employed to eliminate aberrations. According to the Rayleigh Criterion, the resolution limit in optical microscopes can

reach half the wavelength of light. However, in electron optics, eliminating aberrations is considerably more challenging. For magnetic lenses, the determining factor affecting resolution is not the Rayleigh Criterion but rather various aberrations. As an example, consider that the electron wavelength at 100 kV is only $1/10^5$ of the wavelength of light. Despite this, the resolution of a transmission electron microscope (TEM) only improves by a factor of 103. This discrepancy is due to the presence of aberrations. Over time, researchers have identified several magnetic lens aberrations, which have limited the improvement in the resolution of TEMs. Because the wavelength of high-energy electron beams is much smaller than the characteristic dimensions of magnetic lenses, the geometric path of the electron beam in a magnetic field can be approximately described using geometric optics. For simplicity, let's illustrate these aberrations in magnetic lenses by drawing an analogy to the refraction of light in a glass lens. Figure 2-5 depicts four common aberrations in electron microscopes: spherical aberration, chromatic aberration, astigmatism, and coma.

Spherical aberration occurs due to stronger refraction of the electron beam by the edge portion of the lens. As illustrated in Figure 2-5 (a)[13], rays close to the optical axis converge closer to the lens than rays farther from the axis. This results in an unfocused point at the focal position, forming a blurry circular spot instead of a clear point. By translating a plane perpendicular to the optical axis near the focus, a position with the smallest diameter of the diffuse circle, representing the optimal focus point, can be determined. The expression for spherical aberration coefficient (c_s) is given by:

$$\delta = c_s \alpha^3 \qquad (2\text{-}6)$$

In here, δ is the minimum radius of the diffuse circle, $c_s$is the spherical aberration coefficient, and α is the semi-aperture angle. Blocking the electron beam near the lens edge with a small aperture can effectively reduce spherical aberration. However, reducing the semi-aperture angle α also decreases the resolution. Therefore, both parameters must be chosen judiciously to achieve optimal resolution. The spherical aberration coefficient c_s in modern transmission electron microscopes (TEMs) is generally around 1 mm. Since magnetic lenses cannot diverge, spherical aberration cannot be eliminated by a combination of convex and concave lenses, as in optical systems. For a long time, spherical aberration was the primary factor affecting the resolution of transmission electron microscopes. Chromatic aberration arises due to different velocities of the electron beam [13]. As shown in Figure 2-5 (b), in a magnetic lens, electrons with shorter wavelengths have higher speeds, resulting in a longer focal length in the magnetic field, while electrons with longer wavelengths have lower speeds and a shorter focal length. Causes of chromatic aberration include variations in the initial velocity of the electron beam during emission, different scattering energies when passing through the sample, and fluctuations in acceleration voltage and excitation current. Modern TEMs can control chromatic aberration within an acceptable range by adding a monochromator. Astigmatism [13]occurs due to the lack of strict axial symmetry in the magnetic field. When manufacturing magnetic lenses, it is challenging to create a perfectly round shape for enhancing the magnetic field. Tiny non-circularities in the shape of the magnet can cause electrons to deviate from their normal trajectories as they pass through. As shown in Figure 2-5 (c), the focusing capabilities in two directions

orthogonal to each other are not the same. This asymmetry leads to the enlargement of sharp points into blurred spots, resulting in decreased resolution. In modern TEMs, astigmatism can be corrected by using an astigmatism corrector. This corrector improves the magnetic field distribution by adding eight symmetrically distributed small screws between the lens polepieces. Coma [13] is a type of off-axis image aberration. As depicted in Figure 2-5 (d), a bundle of slanting parallel rays, after refraction by the lens, does not converge to a single point on the focal plane. Instead, it forms an asymmetric diffuse light spot. The shape of this diffuse spot resembles a comet, with a bright and distinct head and a broad, faint tail. Modern TEMs can eliminate coma through a coma-free device.

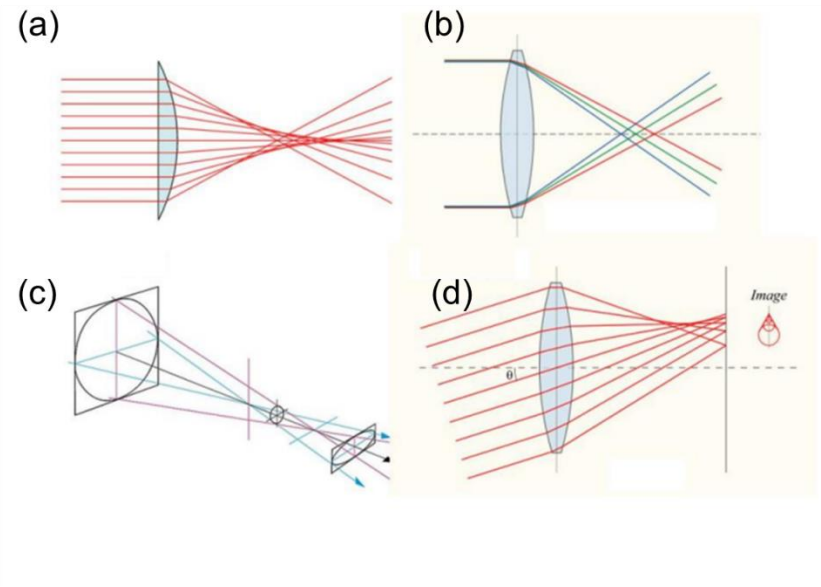

Figure 2-5. Schematic diagrams of spherical aberration, chromatic aberration, aberration and coma[13]

2.10.3 Formation of lattice stripe phase

When only the transmitted beam and a strong diffracted beam are involved in imaging, interference between the two electron beams produces one-dimensional lattice fringe patterns. In practical operations, a condenser aperture on the back focal plane can be used to select the desired imaging electron beam. The schematic diagram is illustrated in Figure 2-6 (a). The imaging conditions for lattice fringe patterns are not strictly restricted; as long as two columns of electron waves interfere to form an image, it is not necessary to align with the crystal zone axis. These patterns can be observed under a wide range of defocus conditions and different sample thicknesses, making them easy to obtain. In the observed Si nanowires, as shown in Figure 2-6 (b)[14], and in the case of tiny second-phase precipitation, most of the images are lattice fringe patterns. These images are useful for observing the size and morphology of the objects, distinguishing between amorphous and crystalline regions. However, they do not provide information related to the crystal structure of the sample and cannot be simulated or calculated. The lattice fringe spacing d_m is related to the reciprocal vector of the diffracting crystal plane as follows:

$$d_m = \frac{1}{g_m} = \frac{1}{g_2 - g_1} \tag{2-7}$$

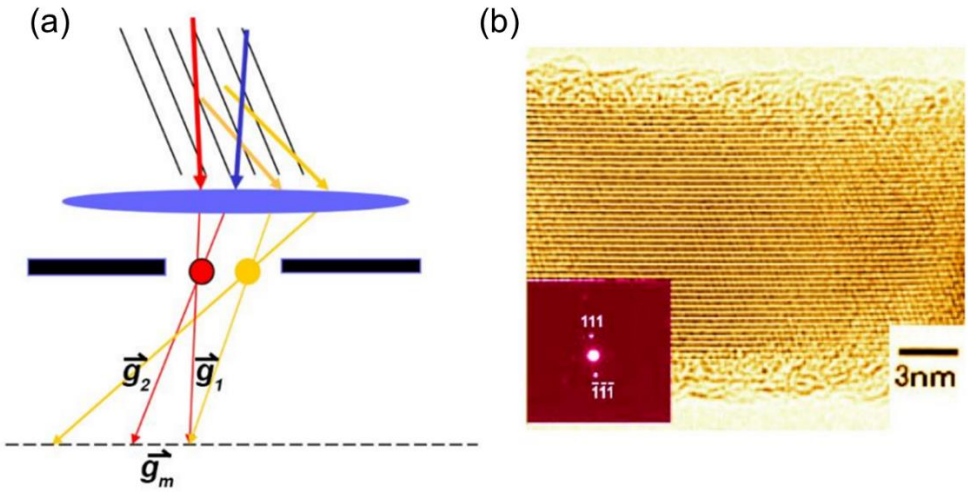

Figure 2-6. (a) Schematic diagram of the formation process of 1D lattice fringes; (b) 1D lattice fringes of Si nanowires[14].

2.10.4 Formation of two-dimensional lattice phase

When the transmitted beam and two or more strong diffracted beams participate in imaging, interference between multiple electron beams produces two-dimensional lattice images (Figure 2-7 a). This is the most common form of high-resolution images that we encounter. In most literature, two-dimensional lattice images are prevalent. In this case, a crystal zone axis is parallel to the incident electron beam, and the corresponding diffraction pattern represents the diffraction spectrum of the unit cell (Figure 2-7 b). For example, the two-dimensional lattice image of Au along the crystal zone axis direction is shown[15]. Two-dimensional lattice images can be obtained under different defocus conditions and sample thicknesses, making them widely used in materials science research to gather information about defects, grain boundaries, phase boundaries, precipitation, and crystallization. It is essential to note that the patterns of two-dimensional lattice images change with defocus, sample thickness, and aperture

size. They do not directly specify the positions of individual atoms. Under uncertain imaging conditions, structural information about the crystal cannot be determined, and computational simulations are often employed for further analysis.

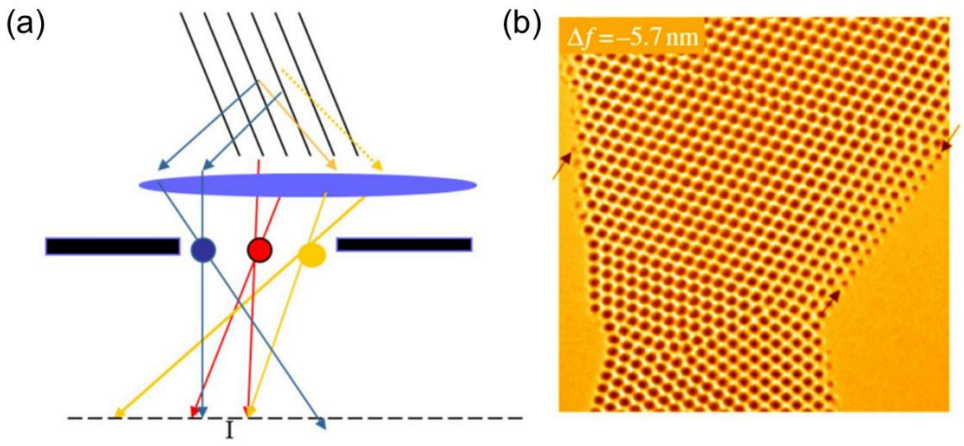

Figure 2-7. (a) Schematic diagram of the formation process of a two-dimensional lattice image; (b) two-dimensional lattice image of Au along the crystallographic band axis (110) direction[15].

2.11 Bibliography

1. Tauc, J., Optical properties and electronic structure of amorphous Ge and Si. *Materials research bulletin* **1968,** *3* (1), 37-46.

2. Yang, Y.; Ostrowski, D. P.; France, R. M.; Zhu, K.; Van De Lagemaat, J.; Luther, J. M.; Beard, M. C., Observation of a hot-phonon bottleneck in lead-iodide perovskites. *Nature Photonics* **2016,** *10* (1), 53-59.

3. Talsky, G.; Mayring, L.; Kreuzer, H., High-resolution, higher-order UV/VIS derivative spectrophotometry. *Angewandte Chemie International Edition in English* **1978,** *17* (11), 785-799.

4. Talsky, G., Derivative spectrophotometry: low and higher order. VCH Verlaggesellschaft GmbH. Weinheim, 228p: 1994.

5. De, A.; Das, S.; Samanta, A., Hot hole transfer dynamics from CsPbBr3 perovskite nanocrystals. *ACS Energy Letters* **2020,** *5* (7), 2246-2252.

6. Moreels, I.; Hens, Z., On the Interpretation of Colloidal Quantum-Dot Absorption Spectra. *Small* **2008,** *4* (11), 1866-1868.

7. Rivnay, J.; Mannsfeld, S. C.; Miller, C. E.; Salleo, A.; Toney, M. F., Quantitative determination of organic semiconductor microstructure from the molecular to device scale. *Chemical reviews* **2012,** *112* (10), 5488-5519.

8. *电子显微分析*. 清华大学出版社: 2006.

9. *显微传：清晰的纳米世界*. 清华大学出版社：2015.

10. 郭可信， 金相学史话 (6)： 电子显微镜在材料科学中的应用． *材料科学与工程* **2002,** *20* (1), 5-10.

11. Paredes, I. J.; Sahu, A., *Synthesis and Structure of Colloidal Quantum Dots*. American Chemical Society: 2023.

12. *分析电子显微学导论*. 高等教育出版社：2015.

13. 董辉．量子点太阳能电池的原位透射电子显微学研究．东南大学，2018.

14. Qi, J.; White, J. M.; Belcher, A. M.; Masumoto, Y., Optical spectroscopy of silicon nanowires. *Chemical physics letters* **2003,** *372* (5-6), 763-766.

15. Dahmen, U.; Erni, R.; Radmilovic, V.; Ksielowski, C.; Rossell, M.-D.; Denes, P., Background, status and future of the transmission electron aberration-corrected microscope project. *Philosophical Transactions of the Royal Society A: Mathematical, Physical and Engineering Sciences* **2009,** *367* (1903), 3795-3808.

Chapter 3 In-situ room-temperature synthesis of all colloidal quantum dot $CsPbBr_3$-PbS heterostructures

3.1 Introduction

Quantum dots (QDs), celebrated for their tunable bandgaps and confined excitons, are a focal point in optoelectronics[1]. Their unique properties have catalyzed progress in a diverse array of applications, including solar cells, light-emitting diodes (LEDs), detectors, and optical imaging[2-5]. Nevertheless, in scenarios demanding fast inter-quantum charge transfer or a broad spectral response, ranging from visible to infrared, single-material QDs may encounter their limits[6-10]. Addressing this, researchers have engineered QD heterostructures, marrying two or more materials to synergize their individual strengths. These heterostructures greatly broaden the utility of QD systems. Their varied spectroscopic characteristics of the QD heterostructures enable a wider range of optical responses, while facilitating internal charge transfers within the heterostructure. This interaction imbues one QD with the power to enhance another, harnessing the advantages of both types. The result is a composite system that expands the scope and improves the ability for optoelectronic applications[11-13]

Recently, perovskite and chalcogenide QDs are becoming two shining stars in optoelectronic research area. The allure of perovskite lies in their facile high photoluminescence quantum yields (PLQY), direct bandgap, high light absorption in

the visible and ultraviolet (UV) regions, and excellent defect tolerance[14-16]. In contrast, chalcogenide QDs, particularly PbS QDs, captivate scientists with their wide tunable bandgap, high infrared absorption, and exceptional environmental stability[17]. The combination of these two materials holds great promise in generating numerous favorable properties for optoelectronic applications. In the past few years, notable progress has been made in the exploration of different heterostructure forms and applications composed of perovskites and PbS. In 2015, Ning and co-workers demonstrated the successful creation of a heterostructure between PbS QDs and $MAPbI_3$ perovskite film matrix with minimal lattice mismatch, marking an important milestone[18]. Through further optimization, similar structures were incorporated into near-infrared LEDs, achieving an impressive external quantum efficiency (EQE) of 8.1%[19]. Concurrently, efficient and stable solar cells and photodetectors based on the combination of two-dimensional (2D) PbS nanosheet and perovskite film or nanosheet were developed[20-21]. Yet, the development of perovskite and PbS heterostructures based on an all colloidal QDs (all-CQDs) approach and their applications still remain largely unexplored. Previously, Zhang et. al pioneered the development of the heterostructures by directly blending $CsPbBr_3$ QDs and sulfur source, which opened up the possibilities[22]. Nonetheless, the synthesis of these QD heterostructures using the hot injection method (HI) requires injection temperatures as high as 150°C and a vacuum environment. Such stringent synthesis conditions increase manufacturing costs and pose challenges for industrial-scale applications. Furthermore, from the perspective of reaction kinetics, developing a controllable method, along with identifying strategies to

enhance the integration of the two components for swift and efficient charge transfer, are significant challenges that need to be addressed to unlock their potential in the applications.

In this study, we introduce an in-situ synthesis strategy for all-CQD $CsPbBr_3$-PbS heterostructures at room temperature and first-ever demonstrate their potential in shortwave infrared imaging. The synthesis of all-CQD $CsPbBr_3$-PbS heterostructures is realized by introducing Cs-DOPA (diisooctylphosphinic acid) into the TOPO-$PbBr_2$ (trioctylphosphine oxide) system, sparking a burst nucleation and slow maturation process, followed by the integration of $(TMS)_2S$ (trimethylsulfonium sulfide) to trigger in-situ heterostructure formation. Various analyses including transmission electron microscopy (TEM), X-ray diffraction (XRD), and X-ray photoelectron spectroscopy (XPS) were utilized to confirm the successful formation of all-CQD $CsPbBr_3$-PbS heterostructures. Using time-resolved photoluminescence spectra (TRPL) and transient absorption spectroscopy (TAS), we demonstrate that ultrafast interdot carrier injection initiation time (<1 ps) from the perovskite QDs to the PbS QDs occurs in the heterostructures. Furthermore, our all-CQD $CsPbBr_3$-PbS heterostructures demonstrated tunable and enduring dual emission in both the visible and infrared spectra under ambient conditions, even withstanding over 180 hours of continuous solar illumination. The fluorescence properties of all-CQD $CsPbBr_3$-PbS heterostructures can be conveniently tuned by adjusting the Pb/S molar ratio from 1:1 to 1:30 (for CsPbBr3: 505-471 nm; for PbS: 950-1156 nm). Utilizing our low-cost processing all-CQD heterostructures, we made the first attempt to explore its application in short-

wave infrared imaging (SWIR: wavelength range from 1000 to 2000 nm)[23] and attained a higher resolution compared to pure PbS QDs at a low response threshold of 18 mW/cm^2 (under 365 nm Excitation), which coming within reach of the International Electrotechnical Commission's (IEC) safety threshold (10 mW/cm^2).Our research sheds light on an innovative route to construct controllable and low-cost processing QD heterostructures capable of ultrafast charge transfer, thereby paving the way for their future applications.

3.2 Experimental methods

Chemicals: Cesium bromide (CsBr, 99%), Lead bromide ($PbBr_2$, 99.99%), hexane (≥99%), diisooctylphosphinic acid (DOPA, 90%), and trioctylphosphine oxide (TOPO, 90%) were purchased from Sigma Aldrich. Lecithin (>97% from soy) was purchased from Carl Roth. n-octane, chlorobenzene (99%), and ethyl acetate were purchased from Wako. TMS_2S (trimethylsulfonium sulfide). All chemicals were used as received without further purification.

Preparation of Cs-DOPA Solution: A Cs-DOPA solution with a concentration of 0.02 M was prepared as follows: Cs_2CO_3 (100 mg) was mixed with DOPA (1 mL) and octane (2 mL) at a temperature of 120°C. The resulting mixture was then diluted with hexane (27 mL).

Preparation of $PbBr_2$-TOPO Solution: A $PbBr_2$-TOPO solution with a

concentration of 0.04 M was prepared as follows: $PbBr_2$ (1 mmol) and TOPO (5 mmol) were dissolved in octane (5 mL) at a temperature of 120°C. The resulting solution was then diluted with hexane (20 mL).

Preparation of Lecithin Solution: A stock solution of lecithin with a concentration of approximately 0.13 M was prepared by dissolving 0.5 gram of lecithin in hexane (10 mL).

Synthesis of $CsPbBr_3$ QDs: $CsPbBr_3$ QDs were synthesized using an improved amine-free method. In brief, 40 μL of Cs-DOPA solution was mixed thoroughly with 3 mL of chlorobenzene under continuous stirring. Then, 80 μL of $PbBr_2$-TOPO solution was injected, and the reaction mixture was allowed to stir for 30 minutes to obtain the experimental group of $CsPbBr_3$ QDs. For the control group, the reaction time was extended to 60 minutes. Subsequently, lecithin was added at a Cs-DOPA/lecithin volume ratio of 1:1, and the mixture was transferred to a refrigerator without any further changes.

Synthesis of PbS QDs: PbS QDs were synthesized using a room temperature method. In brief, 80 μL of $PbBr_2$-TOPO solution was mixed thoroughly with 3 mL of chlorobenzene under continuous stirring, Then, 80 μL of $(TMS)_2S$ solution was injected, the solution immediately turns brown, accompanied by yellow fluorescence. After undergoing continuous stirring for 60 minutes, the yellow fluorescence diminishes, and

a black PbS QDs solution is obtained. It is important to emphasize that for the PbS used in near-infrared imaging, the reaction was conducted at a Pb/S molar ratio of 1:30. This ratio was chosen to ensure comparability in near-infrared imaging capabilities.

Synthesis of $CsPbBr_3$-PbS Heterostructures: The experimental group of $CsPbBr_3$ QDs obtained after 30 minutes of reaction was subjected to continuous stirring. Different Pb/S molar ratios (1:1, 1:3, 1:5, 1:10, 1:30) of $(TMS)_2S$ were added, and the reaction was allowed to proceed for another 30 minutes. Then, lecithin was added at a Cs-DOPA/lecithin volume ratio of 1:1, and the mixture was left undisturbed in the refrigerator for 30 seconds without any further changes.

Purification of QDs and Heterostructures: The quantum dot solution was mixed with ethyl acetate in a 1:1 volume ratio. The mixture was centrifuged at 9300 rpm for 5 minutes and 20 seconds, and the supernatant was discarded. To the precipitate, 2 mL of chlorobenzene was added, followed by thorough agitation. The resulting mixture was transferred to the refrigerator for further testing.

Characterization: The morphologies of $CsPbBr_3$ QDs and $CsPbBr_3$-PbS nanoparticles were obtained using high-resolution transmission electron microscopy (HRTEM, JEM-2100F, Akishima, Japan). The UV-vis absorption spectra for all samples were measured by a spectrophotometer (HITACHI, U-3900H, Tokyo, Japan). The phase identification was performed on an X-ray diffraction (XRD, TTR-III, Rigaku

Corporation, Tokyo, Japan). The photoluminescence quantum yield (PLQY) of the QD solution was obtained with an integrating sphere of an Absolute PL Quantum Yield Spectrometer system (C11347, Hamamatsu Photonics, Hamamatsu, Japan), and the excitation power was 0.1 mW Vis. Time-resolved PL (TRPL), PL are all recorded with the PL system from TOKYO INSTRUMENT, INC. A 375 nm pulsed diode laser was used as the excitation source. An adjustable neutral density filter was adopted to adjust the excitation intensity. The PL detection was used with a PMT together with a TCSPC module. NIR (TRPL)spectra were characterized by a NIR PL lifetime spectrometer (C12132, Hamamatsu Photonics, Hamamatsu, Japan). X-ray photoelectron spectroscopy (XPS) data were accumulated on a photoelectron spectrometer, S4 JPS-590MX (JEOL, Ltd., Japan). Transient absorption (TA) measurements were carried out using a femtosecond (fs) TA setup. The pump and probe pulses were delivered by a titanium/sapphire laser (CPA-2010, Clark-MXR Inc., Dexter, MI, USA) with a pulse width of 150 fs, a wavelength of 775 nm, and a repetition rate of 1000 HZ. The laser light was split into two parts; one part was incident on a sapphire plate to produce white light for the probe beam. The other part was used as a pump pulse (wavelength can be tuned from 290 nm to 3 μm) converted from an optical parametric amplifier (a TOAPS from Quantronix, Hamden, CT, USA). The pump light was used to excite the sample. To collect the transmitted probe light through the samples, a silicon photodiode was employed. In this study, pump light with wavelengths of 470 nm and 600 nm was utilized to excite all the samples. The structural stability testing was performed by subjecting the samples to continuous illumination from a xenon lamp that simulated

solar light conditions (SAN-EI ELECTRIC, 150W XES-40S2-CE, Japan). SWIR imaging was achieved using a visible near-infrared dual-mode camera (FLIR C3-X, Sweden), which enabled the visualization of both visible and near-infrared wavelengths. In brief, both PbS QDs and heterostructures synthesized at a Pb/S molar ratio of 1:30 were mixed with an equal volume of chlorobenzene solution containing PMMA. These mixtures were then used to prepare "UEC" patterns. The patterns were air-dried at room temperature and then placed within the detection range of the fixed excitation light and the infrared camera. This setup allowed for a direct comparison of their near-infrared imaging capabilities.

Calculating the PLQY of the nanocomposite

In detail, we initially prepared solutions of different Pb/S with same concentration and obtained the PLQY of $CsPbBr_3$ within these heterostructures under excitation at 465 nm. Subsequently, using a spectrometer capable (HAMAMATSU C11367) of simultaneously detecting both visible and infrared fluorescence signals, we acquired the fluorescence spectra under identical testing conditions. We have calculated the fluorescence peak areas of $CsPbBr_3$ and PbS within the heterostructure through integration (A_{CsPbBr_3}, A_{PbS}). In this context, we can calculate the PLQY of PbS within heterojunction ($PLQY_{PbS\ in\ Hetero.}$) and the entire heterostructure ($PLQY_{\ Hetero.}$) by using the following equation:

$$PLQY_{PbS\ in\ Hetero.} = \frac{PLQY_{CsPbBr_3\ in\ Hetero.} \times A_{PbS}}{A_{CsPbBr_3}}$$

$$PLQY_{Hetero.} = PLQY_{PbS\ in\ Hetero.} + PLQY_{CsPbBr_3\ in\ Hetero.}$$

Calculating the carrier transfer efficiency (η_{trans})

The Photoluminescence Quantum Yield of PbS quantum dots ($PLQY_{PbS}$) and the carrier transfer efficiency (η_{trans}) within the heterostructure can be calculated using the following equations according the previous papers[18, 24]

$$PL_{PbS}=\left(A_{PbS}+\eta_{trans}A_{pero}\right)\times PLQY_{PbS\ in\ Hetero.}\times I_{ex.}$$

I_{ex} represents the power density of the excitation light, PL_{PbS} signifies the fluorescence intensity of PbS, $A_{pero.}$, and A_{PbS} represent the absorbance values extracted from the absorption spectra of perovskite and PbS at the excitation wavelength, respectively. $PLQY_{PbS\ in\ Hetero.}$ denotes the PLQY of PbS within the heterostructure, and $\eta_{trans.}$ represents the transfer efficiency from $CsPbBr_3$ to PbS.

3.3 Results and discussions

3.3.1 Synthesis all colloidal quantum dot $CsPbBr_3$-PbS heterostructures

To accomplish the in-situ synthesis of all-CQD $CsPbBr_3$-PbS heterostructures, we necessitate the introduced sulfur source to instigate the reconfiguration of surface atoms in $CsPbBr_3$ QDs, further deplete Pb atoms from the $CsPbBr_3$ QD surface, and simultaneously in-situ form PbS on $CsPbBr_3$ QDs. Crucially, this procedure mandates an effective interaction between the sulfur source and the lead atoms of the $CsPbBr_3$ QD surface. This interaction fosters the heterogeneous nucleation of PbS on $CsPbBr_3$ QDs, superseding the creation of isolated PbS QDs through homogeneous nucleation. Consequently, our experimental emphasis rests on ensuring the surface accessibility of $CsPbBr_3$ QDs and the reactivity of the sulfur source. As shown in Figure 3-1, we first

crafted high-yield (92%) $CsPbBr_3$ QDs using an optimized amine-free method[25].Importantly, prior to the introduction of capped ligands, this method can keep a fine balance between preserving surface reactivity and ensuring slow growth rates[25], and by maintaining a static ligand environment, it minimizes halide vacancies and ensures stability in the quantum dot structure[26], thus providing a sustained reaction window and favorable conditions for the in-situ growth of PbS. Building upon this, we evaluated several sulfur sources (TOPO-S, N,N-diphenylthiourea, and $(TMS)_2S$) for their potential in in-situ growth on $CsPbBr_3$ QDs[27](Figure 3-2, 3-3). Finally, the realized all-CQD $CsPbBr_3$-PbS heterostructures owe their formation to $(TMS)_2S$, its high reactivity as a sulfur source than the others.

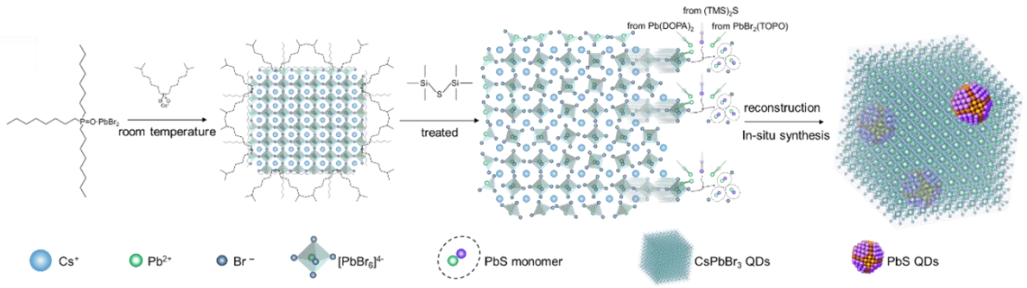

Figure 3-1. Schematic diagram illustrating the formation of the all-CQD $CsPbBr_3$-PbS heterostructures. In the synthesis of all-CQD $CsPbBr_3$-PbS heterostructures at different Pb/S molar ratios, $CsPbBr_3$ QDs first treated by $(TMS)_2S$ and followed by reconstruction process, simultaneously, PbS monomers formed, and finally in-situ synthesis all-CQD $CsPbBr_3$-PbS heterostructures.

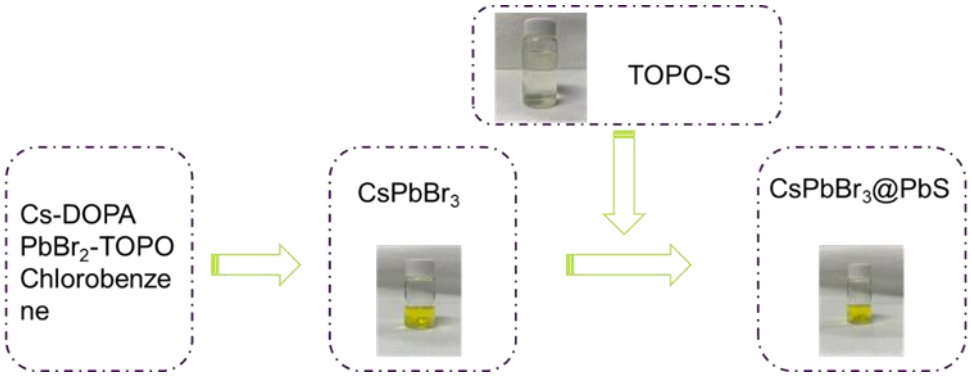

Figure 3-2. Experimental procedure utilizing TOPO-S as a sulfur source. TOPO-S was prepared by thoroughly dissolving 2 mmol TOPO and 2 mmol S in 5 ml of octane (diluted to 20 ml with hexane). However, the addition of TOPO-S to the $CsPbBr_3$ quantum dot solution did not result in the formation of $CsPbBr_3$-PbS heterostructures due to the significantly low reactivity of TOPO-S.

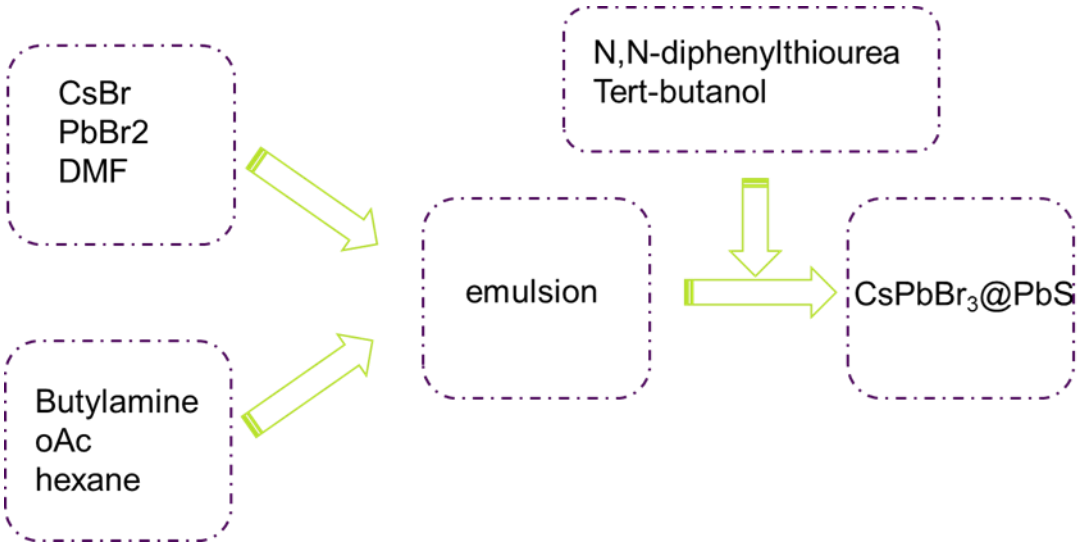

Figure 3-3. Experimental procedure utilizing N,N-diphenylthiourea as a sulfur source. The microemulsion method was employed based on a previously reported literature [27]. However, the formation of $CsPbBr_3$-PbS heterostructures was not achieved using this approach due to the strong detrimental effects of butylamine on the QDs.

In Figure 3-4 (a-c), we confirmed the formation of the heterostructures by TEM images. The pristine $CsPbBr_3$ QDs featured a uniform size distribution around 8.1 nm (Figure 3-4 a, c), exhibiting a consistent color contrast. In contrast, the QDs underwent

a remarkable transformation upon the incorporation of sulfur at a Pb/S molar ratio of 1:1. As revealed by the TEM images in Figure 3-4 b, the newly appeared black dots dispersed uniformly on the $CsPbBr_3$ QDs are indicative of the in-situ formation of PbS QDs onto $CsPbBr_3$ QDs. Here, we posit that the alteration in $CsPbBr_3$ QDs' size (9.4 nm, Figure 3-4 e) within the heterostructure arises from the reconstruction process of $CsPbBr_3$ QDs. The high-resolution TEM (HRTEM) images distinctly illustrate the all-CQD $CsPbBr_3$-PbS heterostructure, where the interplanar distances of 4.13 Å and 2.93 Å (Figure 3-4 c) correspond to the (110) and (200) crystal planes of $CsPbBr_3$ and PbS QDs, respectively. The energy dispersive spectrometer (EDS) analysis further verified the domain distribution and elemental composition of the heterostructures as shown in Figure 3-5.

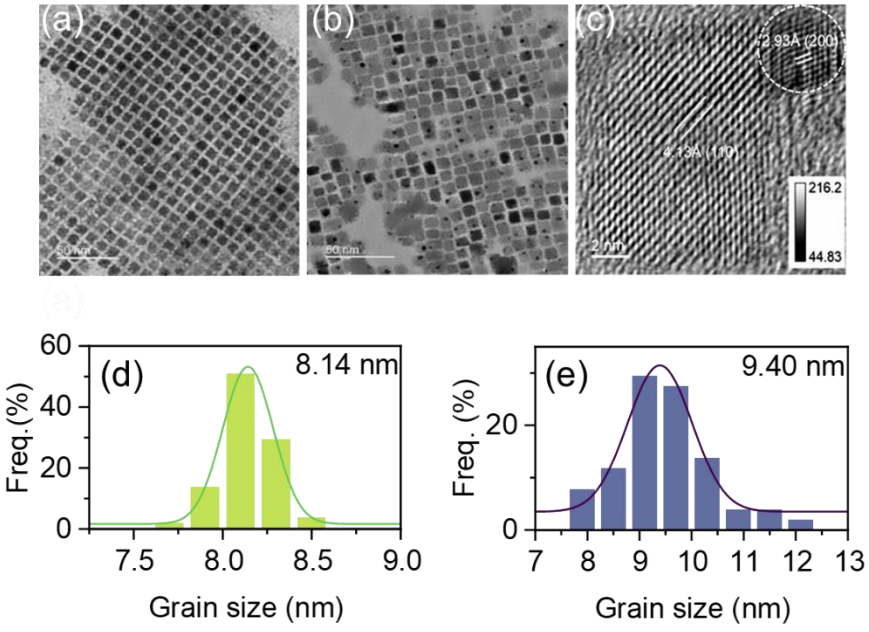

Figure 3-4. (a) The TEM image of $CsPbBr_3$ QDs reveal a uniform size distribution. (b) The TEM image of all-CQD $CsPbBr_3$-PbS heterostructures (Pb/S 1:1 heterostructures). (c) High-resolution TEM (HRTEM) of all-CQD $CsPbBr_3$-PbS

heterostructures (Pb/S 1:1 heterostructures). (d) The size distribution plot of $CsPbBr_3$ QDs reveal an average size of 8.14 nm. (e) The size distribution plot of all-CQD $CsPbBr_3$-PbS heterostructures (Pb/S 1:1 heterostructures) reveal an average size of 9.40 nm.

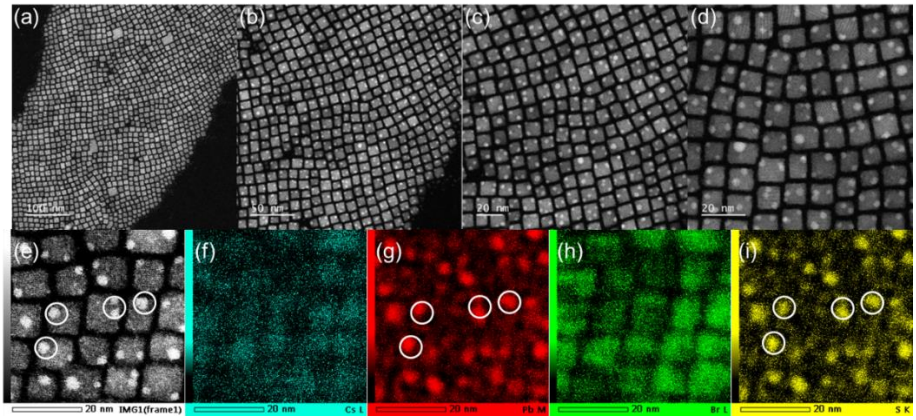

Figure 3-5. Energy-dispersive X-ray spectroscopy (EDS) of Pb/S 1:1 heterostructure. Clear signals for Cs, Pb, Br, and S elements were observed, with noticeable enrichment of S in the PbS components, substantiates the existence of the heterojunction.

The formation of a heterostructure suggests an inclination towards in-situ heteroepitaxial growth of PbS on the $CsPbBr_3$ surface rather than a homogenous growth in individual PbS QDs in our methods. Except of the synthesis methods, this in-situ heteroepitaxial growth also benefits from the minimal lattice strain caused by the matching of the (200) and (220) crystal facets of both $CsPbBr_3$ and PbS QDs (Figure 3-6). Relative to their pure counterparts, we observe within the all-CQD $CsPbBr_3$-PbS that the $CsPbBr_3$ component manifests a slight low-angle shift in the (200) and (220) crystal planes (from 30.43 to 30.25, and from 43.61 to 43.47 respectively). In contrast, the PbS component exhibits a minor high-angle shift (from 29.50 to 29.71, and from 42.45 to 42.59) (Figure 3-7). Observed shifts in peak positions reveal lattice expansion

(tensile strain) in $CsPbBr_3$ QDs and lattice contraction (compressive strain) in PbS QDs, evidence of their adjustment in the heteroepitaxial environment, thus affirming successful heterostructure formation. Additionally, the absence of characteristic diffraction peaks related to metallic lead at 31.3°[28] solidify that the hetero-anchoring occurs solely between pure $CsPbBr_3$ and PbS QDs, with no involvement of metallic lead.

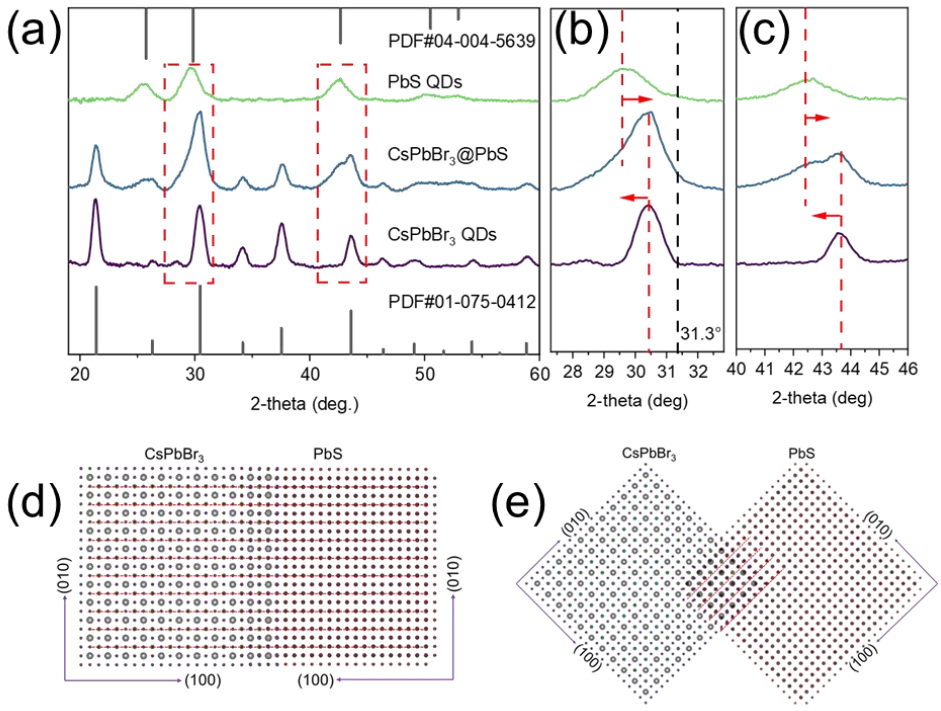

Figure 3-6. (a-c) X-ray diffraction (XRD) patterns of all-CQD $CsPbBr_3$-PbS heterostructures, PbS and $CsPbBr_3$ QDs. (d-e) Schematic diagram illustrating the epitaxial growth of heterostructure nanoparticles. To illustrate the epitaxial growth of heterostructures.

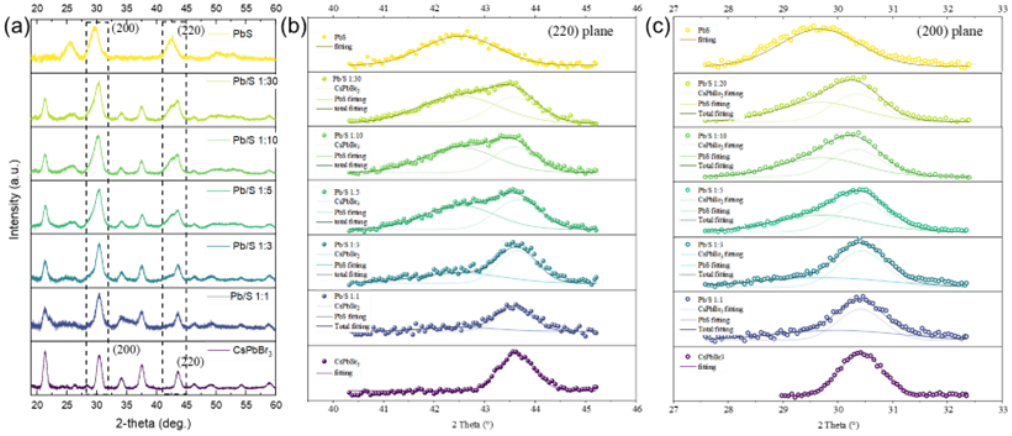

Figure 3-7. (a) X-ray diffraction (XRD) patterns of all samples, with dashed boxes highlighting the (200) and (220) crystal planes of PbS and $CsPbBr_3$ QDs, respectively.

Based on the heterostructure growth mechanism in our method, the concentration of sulfur serves as a critical factor in the evolution of the heterostructure. Therefore, by adeptly adjusting the Pb/S molar ratio from 1:1 to 1:30, we can meticulously govern the size and optical spectra of the two QDs contained within the heterostructure. The variations brought about by different Pb/S ratios were initially identified through XRD, which revealed a gradual increase in the PbS QDs mass percentage (ω%). As shown in Figure 3-7 a, clear diffraction peaks were observed for $CsPbBr_3$ QDs at 21.38°, 30.41°, 37.47°, and 43.56°, corresponding to the (110), (200), (211), and (220) crystal planes of cubic-phase (PDF#01-075-0412). With the increase in Pb/S ratio, new diffraction peaks appeared at 25.71°, 29.78°, and 42.61°, corresponding to the (111), (200), and (220) crystal planes of PbS QDs (PDF#04-004-5639). By analyzing the gradually broadening diffraction peaks corresponding to the (200) and (220) crystal planes of $CsPbBr_3$ as the Pb/S ratio increase, we conducted fitting and calculations to determine the mass fraction of $CsPbBr_3$ and PbS QDs in the all-CQD heterostructures at different

Pb/S ratios (Figure 3-8). The results revealed a progressive increase in the mass fraction of PbS, denoted as ω(PbS). The broadening of the diffraction peaks from crystal planes can be attributed to two main factors: (1) the refinement of $CsPbBr_3$ QDs, (2) the microstrain in the all-CQD $CsPbBr_3$-PbS heterostructures.

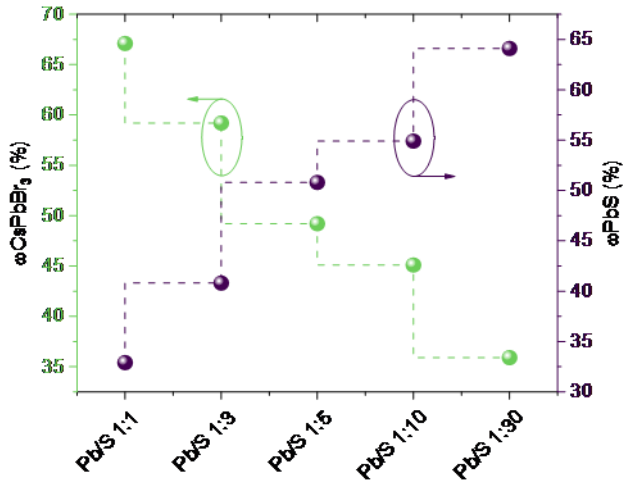

Figure 3-8. Calculated values of ω(PbS) and ω($CsPbBr_3$) for different Pb/S heterostructure nanoparticles using the adiabatic method.

Furthermore, samples with different Pb/S ratios exhibited distinct Cs 3d, Pb 4f, Br 3d, and S 2p signal peaks in XPS and showed stronger Pb-S bonds with increasing Pb/S. XPS not only provides clear signals of Cs 3d, Pb 4f, Br 3d, and S 2p (Figure S9-12), but also distinguishes between the Pb-Br bonds in $CsPbBr_3$ QDs and the Pb-S bonds in PbS QDs. This distinction arises from the different electronegativities of Br^- and S^{2-}. The Pb 4f binding energies are observed at 137.83 eV and 143.61 eV for Pb-Br bonds[29-30], while for Pb-S bonds, they appear at 137.42 eV and 142.29 eV[31-32] (Figure 3-9 a-c). As illustrated in Figure 3-9 d, the peak separation energy of Pb 4f, reveals an overall decreasing trend with increasing Pb/S ratio. This trend suggests the presence of stronger

Pb-S bonds[33].

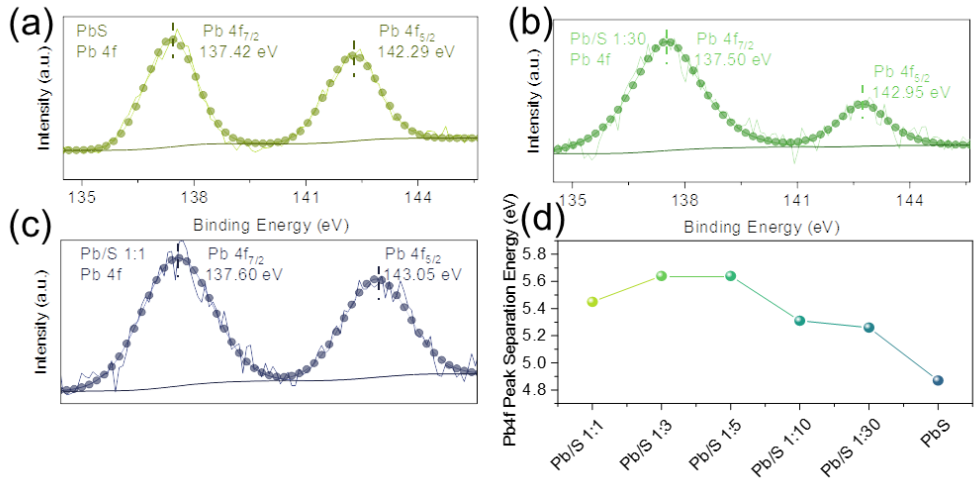

Figure 3-9. (a-c) X-ray photoelectron spectroscopy (XPS) spectra of Pb 4f for different samples. The binding energy of the orbitals gradually shifts to lower energy from $CsPbBr_3$ QDs to PbS QDs. (d) Peak separation energy extracted from the XPS spectra of Pb 4f in different samples.

3.3.2 Optical properties of all colloidal quantum dot $CsPbBr_3$-PbS heterostructures

Figure 3-10 showcases the spectral characteristics of the heterostructures, where different Pb/S molar ratios have been introduced. In these spectral measurements, we standardized the concentration of all samples by maintaining the sulfur concentration at 0.00106 mol/L. As we increased the sulfur input, the resulting heterostructure solutions displayed deeper colors and notably blue shift in fluorescence color (Figure 3-10 a-b). The observed phenomena can be directly substantiated by the absorption spectroscopy (ABS) and photoluminescence (PL) spectroscopy (Figure 3-10 c-d). The pristine $CsPbBr_3$ QDs displayed a photoluminescence wavelength (PLW) of 495 nm. As the Pb/S molar ratio increased, we first observed a red-shift at Pb/S 1:1

heterostructure, followed by a progressive blue-shift in the exciton absorption and fluorescence peaks originating from $CsPbBr_3$ QDs counterpart in the heterostructure. The peak position of exciton absorption, PLW of these samples are compiled and illustrated in Figure 3-10 e-f.

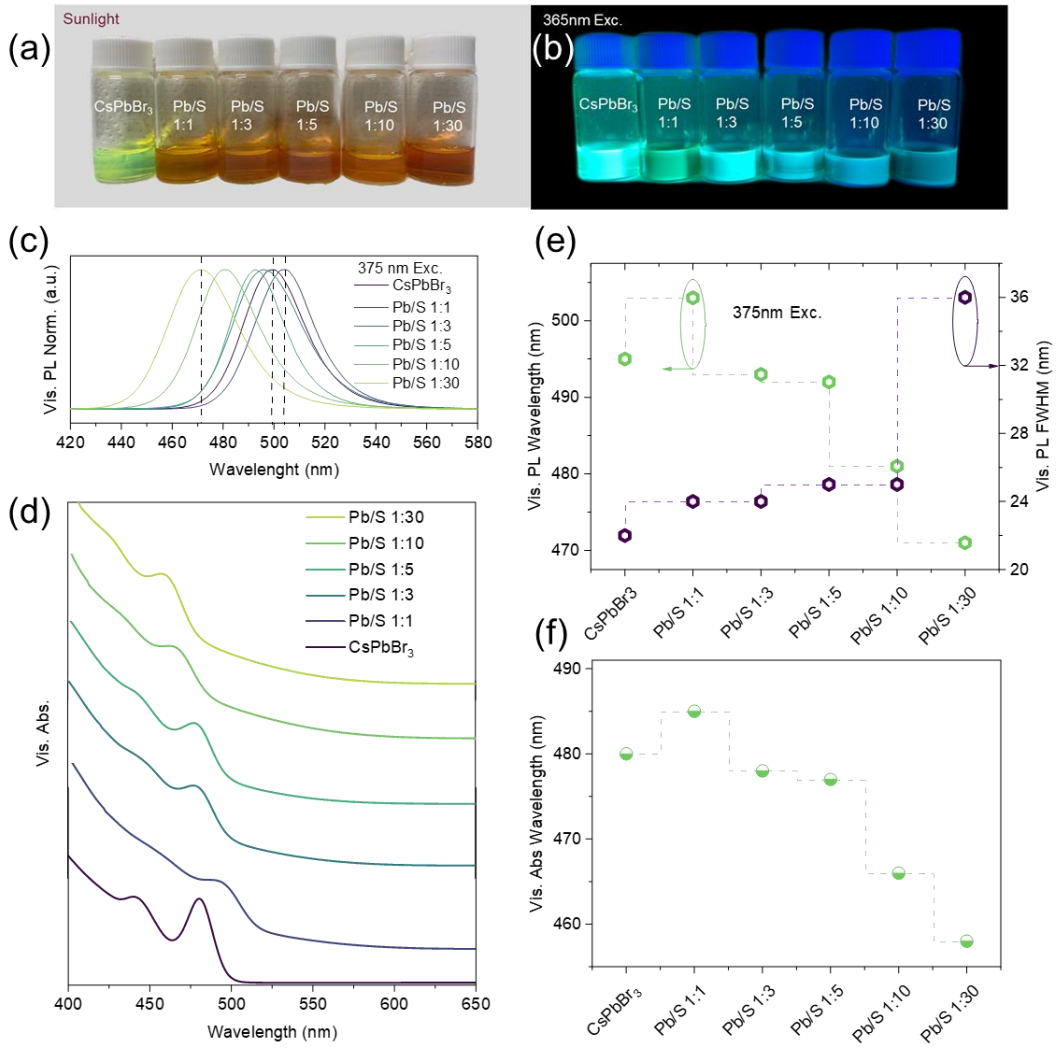

Figure 3-10. (a-b) Photographic images of pure $CsPbBr_3$ QDs and all-CQD $CsPbBr_3$-PbS prepared with different Pb/S ratio from 1:1 to 1:30 under sunlight (a) and 365 nm excitation (b). (c-d) The photoluminescence spectra in the visible region for different samples (c) and corresponding absorption spectra (d). (e) Photoluminescence peak positions and full width at half maximum (FWHM) of different samples in the visible

region. (f) Absorption peak positions of different samples in the visible region.

The observed spectral changes in peak position may potentially result from a competitive interplay between the red-shift instigated by surface reconstruction during initial heterostructure formation, and the ensuing blue-shift triggered by surface etching of the reformed $CsPbBr_3$ QDs (Figure S15-19, and Note S3), and we emphasize that the realization of this blue shift requires a 10-day period of quiescence without any external energy input (Figure S19).

To gain a better understanding of the fluorescence shift of all-CQD heterostructures with different Pb/S molar ratios, we provide a schematic illustration as depicted in Figure 3-1. It is worth emphasizing that, during the preparation process of all-CQD heterostructures, $CsPbBr_3$ QDs first treated by $(TMS)_2S$ and followed by reconstruction process, which leads to the momentary quenching and subsequent restoration of fluorescence (as indicated by the red dashed line in Figure 3-11). Similar processes have been reported in QDs treated with thiols [34].

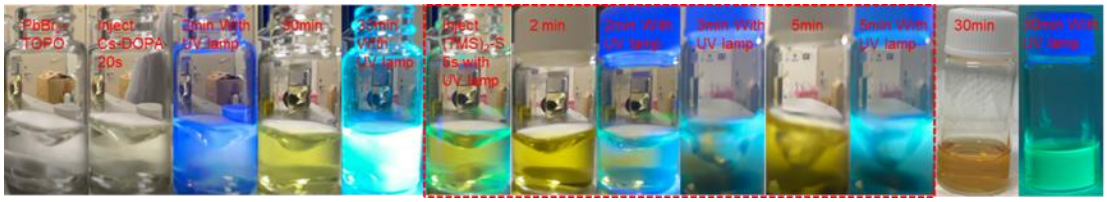

Figure 3-11. Photographs at different time points during the synthesis of all-CQD $CsPbBr_3$-PbS heterostructures. The images within the red box depict the process of treating by $(TMS)_2S$ and reconstruction of $CsPbBr_3$ QDs after the addition of $(TMS)_2S$.

Furthermore, in order to confirm the validity of this process, we devised a confirmatory experiment: lecithin was selected for ligand exchange to stabilize

$CsPbBr_3$ QDs due to its unique brush-like structure, which allows for a dense and stable binding with the QDs[35]. After treatment, the QDs were combined with a sulfur source at a Pb/S ratio of 1:1. We predicted that due to the presence of lecithin, only a small fraction of binding sites on the surface of $CsPbBr_3$ would be available for $(TMS)_2S$ to bind. Additionally, due to the limited binding sites and the stabilizing effect of lecithin, the luminescence quenching process would be suppressed, resulting in the absence of fluorescence quenching. As shown in Figure 3-12, the prediction was confirmed well. The fluorescence redshift of Pb/S 1:1 heterostructures can be primarily attributed to the torn $CsPbBr_3$ QDs, $Pb(DOPA)_2$, and $PbBr_2$·TOPO, which provide Pb^{2+} for the formation of PbS QDs, result in a decrease in the precursor concentration for the reconstruction of $CsPbBr_3$ QDs. According to classical nucleation and growth theory, this decrease will lead to larger $CsPbBr_3$ QDs and fluorescence redshift[36].

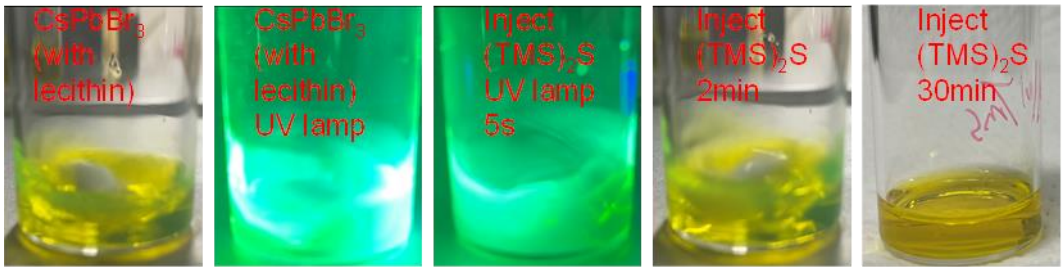

Figure 3-12. Experimental images depicting the validation of $CsPbBr_3$ QDs after the introduction of $(TMS)_2S$ following lecithin ligand exchange. Due to the remarkably high binding density and affinity of lecithin, $(TMS)_2S$ lacks sufficient binding sites, resulting in the absence of significant fluorescence quenching.

However, in the case of Pb/S 1:30 heterostructures, it will result in the generation of smaller $CsPbBr_3$ QDs (as depicted in Figure 3-13). This is attributed to the excessive sulfur source, which further etching the reconstructed $CsPbBr_3$ QDs, leading to the

formation of PbS QDs. This situation has been corroborated by TEM images, as shown in Figure 3-14, which reveal $CsPbBr_3$ QDs with an approximate size of 6 nm. Moreover, the observed fluorescence blue shift depicted in Figure 3-15 serves as additional evidence, solidifying this situation. We also emphasize that the realization of this blue shift requires a 10-day period of quiescence without any external energy input.

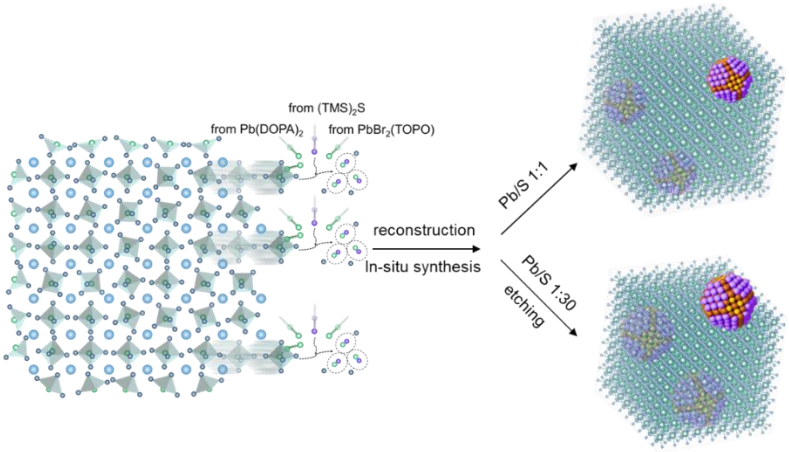

Figure 3-13. Schematic diagram illustrating the formation of the all-CQD $CsPbBr_3$-PbS heterostructures with Pb/S 1:1 heterostructure and 1:30.

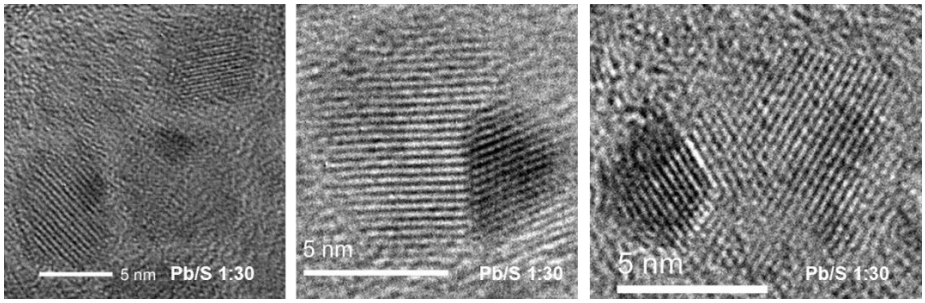

Figure 3-14. TEM images of Pb/S 1:30 heterostructures. The images illustrate a smaller size distribution due to the etching effect of $(TMS)_2S$.

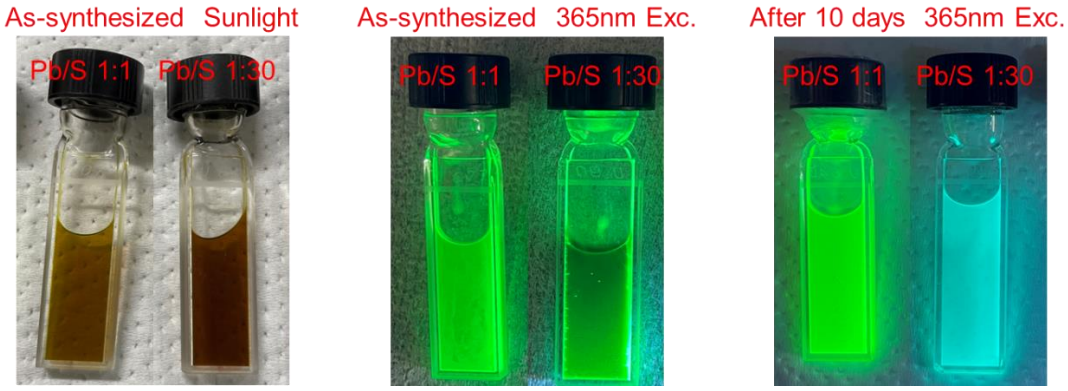

Figure 3-15. Images of the synthesized all-CQD $CsPbBr_3$-PbS heterostructures (Pb/S 1:1 heterostructure, 1:30) at different time points after being transferred to the refrigerator.

Based on the aforementioned researches, it is reasonable to assert that the same chemical reaction process occurred in experiments with different Pb/S ratios, but to varying extents due to differences in reactant concentrations and the fluorescence of reaction products. In other words, a reversible reaction exists in this system. Based on the above analysis, taking Pb/S 1:1 heterostructure as an example, we propose the following reaction process:

Step1. $Cs(DOPA)+1.5\ PbBr_2(TOPO)\rightarrow CsPbBr_3+0.5\ Pb(DOPA)_2$

Step2. $0.5Pb(DOPA)_2+0.5\ (TMS)_2S\rightarrow 0.5\ PbS$

$2.5\ PbBr_2\cdot TOPO+2.5\ (TMS)_2S\rightarrow 2.5\ PbS+5\ TMSBr$

Step3. $CsPbBr_3+(TMS)_2S\rightleftharpoons PbS+CsBr+2\ TMSBr$

Step 2 and Step 3 can be considered as simultaneous processes. As the Pb/S ratio increases, the reaction in Step 3 will shift in the forward. The recombined $CsPbBr_3$ QDs are etched by an excess of $(TMS)_2S$, ultimately leading to a blueshift in fluorescence.

We also observed that enhancing the quantity of the sulfur source effectively modulated the fluorescence and absorption characteristics originating from PbS QDs in

the near-infrared region (NIR) of the heterostructures, as depicted in Figure 3-16 a-b. This augmentation resulted in a redshift of the absorption peak and fluorescence peak of PbS QDs within the heterostructures (Figure 3-16 c-d). By utilizing the function models that relate absorbance spectra to QDs size , we discerned an increase in the size of PbS QDs from 2.9 nm to 3.4 nm as we adjusted the Pb/S ratio from 1:1 to 1:30 (Figure 3-16 e)[37]. This size variation further alters the type I alignment of quantum energy levels in the two types of QDs within the heterostructure, thereby impacting charge transfer[38].

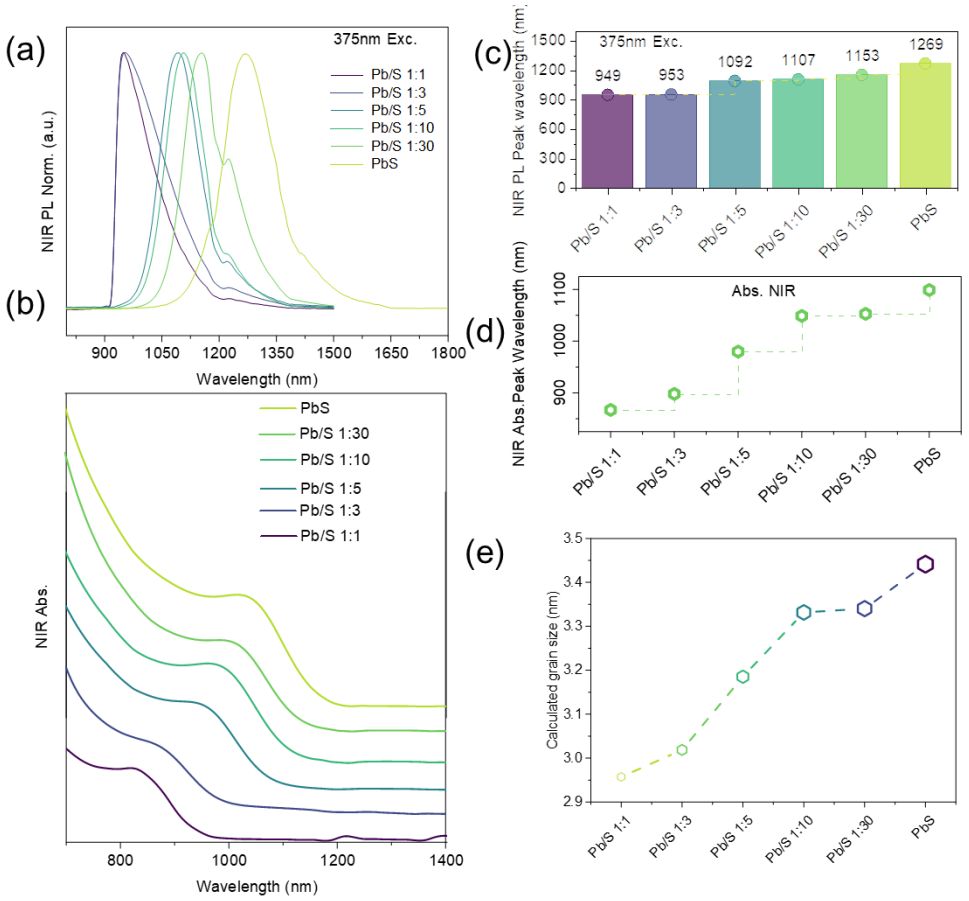

Figure 3-16. The photoluminescence spectra in the near-infrared region for different samples (a) and corresponding absorption spectra (b), (c) Photoluminescence peak positions of different samples in the near infrared region. (d) Absorption peak positions

of different samples in the near infrared region. (e) Theoretical size of PbS QDs in different samples obtained by fitting the absorption spectra data[39]

As illustrated in Figure 3-17 a-c, the observed gradual decrease in fluorescence and photoluminescence quantum yield (PLQY) in the visible region and the corresponding incremental increase in the infrared region substantiate this efficient interdot carrier transfer within the heterostructures. The same conclusion can be drawn regarding the gradual increase in PbS' PLQY with the rising Pb/S ratio, observed in both solution and thin films (Figure 3-17 d-e). However, as depicted in Figure 3-18, this interdot carrier transfer process is inhibited when the Pb/S ratio is excessively high (Pb/S 1:40). Therefore, Pb/S 1:30 is considered the optimal ratio for achieving interdot carrier transfer, with a transfer efficiency reaching 71.56% (Table 3-1).

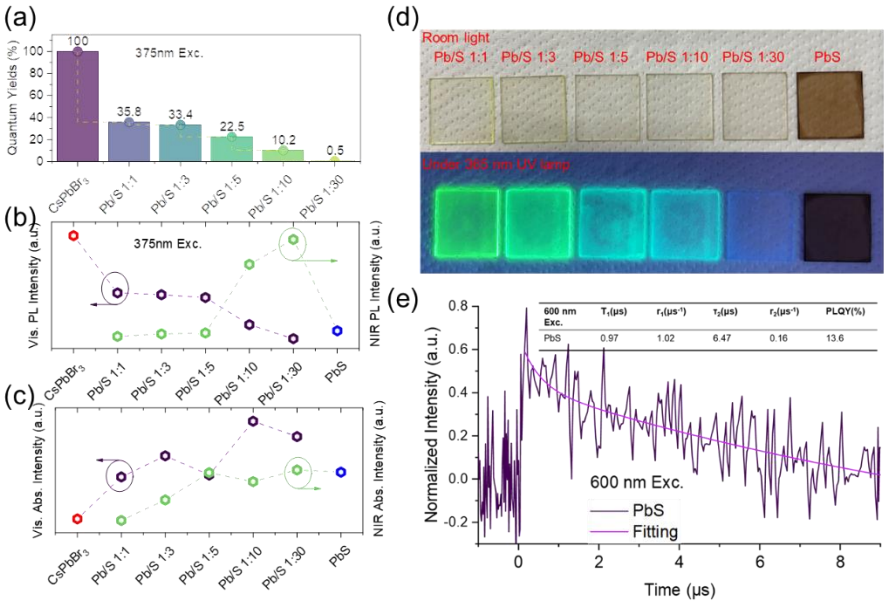

Figure 3-17. (a) Photoluminescence quantum yield for different samples. (b) Photoluminescence intensity trends in the visible and near-infrared region for all samples under 375 nm excitation. (c) Absorption intensity trends in the visible and near-infrared region for all samples. (d) Imagines of different Pb/S and PbS QDs films on

glass (Top: under room light; Bottom: under 365nm UV lamp). (e) The PLQY of PbS thin films obtained through TRPL fitting, based on the literature already reported[40].

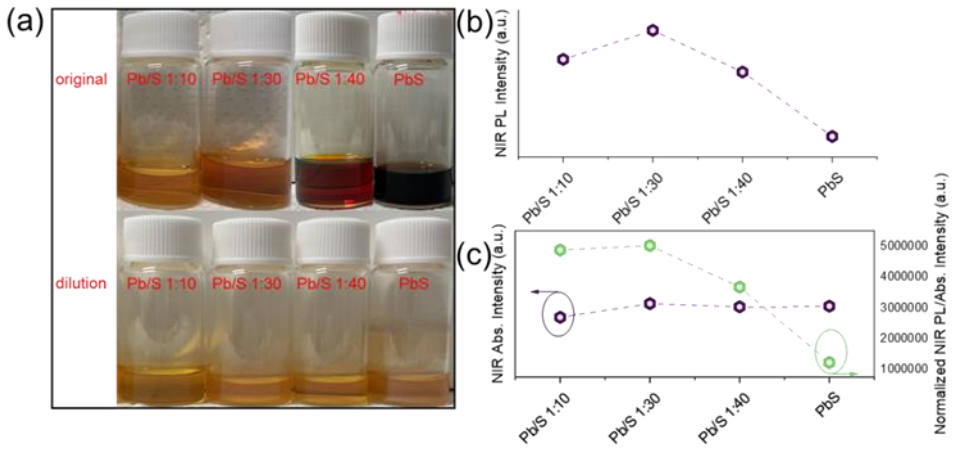

Figure 3-18. (a) Images of the original solution and the dilution solution of Pb/S 1:10, 1:30, 1:40, and PbS QDs. (b) NIR PL intensity of all samples. (c) NIR Abs. intensity of all samples (left); The normalized NIR intensity by using PL/Abs intensity of all samples (right). As Pb/S ratios increased from 1:1 to 1:30, there was a gradual enhancement in the fluorescence emission of PbS. However, when the Pb/S ratio reached 1:40, the fluorescence of PbS displayed a declining trend. This phenomenon might be attributed to an excessive amount of sulfur (S) source binding with lead (Pb), leading to a reduction in $CsPbBr_3$ concentration, thereby constraining the process of charge carrier transfer. Therefore, in this work, we consider a Pb/S ratio of 1:30 to be the optimal proportion.

Table 3-1. The statistical data for the calculated charge carrier transfer efficiency (η_{trans}) in different Pb/S samples.

	Concentration	$I_{ex.}$	PL_{PbS}	A_{PbS}	$A_{pero.}$	$PLQY_{PbS}$	$\eta_{Trans.}$
	mol/L	Counts	Counts				%
PbS 1:1	0.00106	3011395668	131987	0.022	0.138	0.025	21.88
PbS 1:3	0.00106	3011395668	477937	0.059	0.160	0.052	24.92
PbS 1:5	0.00106	3011395668	1756475	0.108	0.140	0.112	33.62
PbS 1:10	0.00106	3011395668	3259940	0.092	0.196	0.156	58.48
PbS 1:30	0.00106	3011395668	5502883	0.113	0.180	0.225	71.56

Here, we dismissed the possibility that the fluorescence augmentation in the infrared region resulted from absorption changes caused by the increased sulfur source. This is because, even after the introduction of a substantial amount of sulfur, the change in absorption in the infrared region was minimal, whereas the enhancement in fluorescence was indeed significant (Figure 3-17 c). Furthermore, ns TA data of samples at varying Pb/S ratios, when exciting only the PbS counterpart, rules out the possibility that the enhanced NIR emission is caused by defect variations (Figure 3-19, Table 3-2).

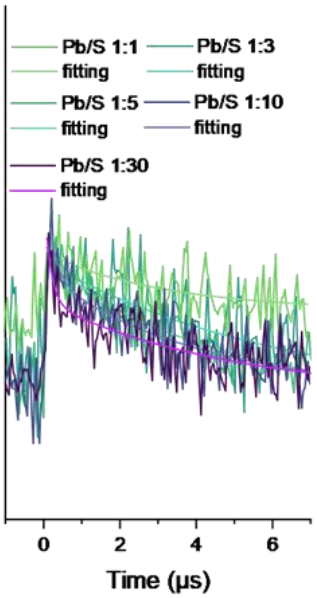

Figure 3-19. ns TA decay of various Pb/S samples excited at 600 nm. The results rule out the possibility that the enhanced NIR emission is caused by defect variations

Table 3-2. The photoexcited carrier lifetimes obtained from the ns TA decays in various Pb/S samples when the samples were excited with 600 nm, where the excitation light can only be absorbed by PbS in the heterostructure.

600 nm Exc.	τ_1(μs)	A_1(%)	τ_2(μs)	A_2(%)	$\tau_{ave.}$(%)
PbS 1:1	0.25	0.13	6.27	0.87	6.23
PbS 1:3	0.49	0.12	4.87	0.87	4.80
PbS 1:5	0.25	0.18	4.26	0.82	4.20
PbS 1:10	0.21	0.50	4.06	0.49	3.87
PbS 1:30	0.55	0.80	4.84	0.20	3.47

3.3.3 Carrier transfer of all colloidal quantum dot $CsPbBr_3$-PbS heterostructures

To delve deeper into the interdot carrier transfer within our heterostructures, we employed ultrafast transient absorption spectroscopy (TAS) to independently monitor carrier populations within each component of the heterostructure when exposed to light. In the TA spectra near the bandgap energy, a reduced absorption (ground state bleach (GSB)) generally corresponds to the presence of excitons and the center of the reduced absorption indicates the exciton transition energy[12]. As shown in Figure 3-20, we employed pump wavelengths of 470 nm and 600 nm to selectively excite the heterostructure, enabling us to study the carrier transfer dynamics. Specifically, the 470 nm pump simultaneously excited the $CsPbBr_3$ QDs and PbS QDs, triggering a carrier transfer from $CsPbBr_3$ QDs to PbS QDs. In contrast, the 600 nm pump only excited PbS QDs, enabling the study of their intrinsic carrier dynamics in isolation. Comparing measurements from both pumps allowed us to more accurately discern charge transfer within the heterostructure, whilst eliminating interference from property disparities between the two types of QDs within the heterostructure.

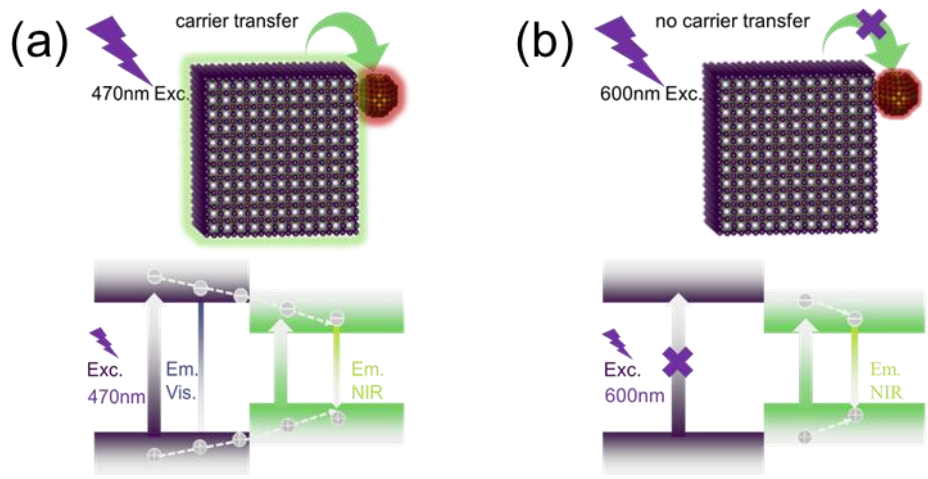

Figure 3-20. (a) Schematic diagram of band alignment and carrier transfer of all-CQD $CsPbBr_3$-PbS heterostructures at 470 nm pump (upper plane) and 600 nm pump (bottom plane).

TAS spectra for Pb/S 1:30 heterostructures, PbS, and $CsPbBr_3$ QDs in the visible and near-infrared regions are shown in Figure 3-21. We gently remind that the TAS measurements were performed immediately after the synthesis of the all-CQD $CsPbBr_3$-PbS heterostructures and PbS, $CsPbBr_3$ QDs.

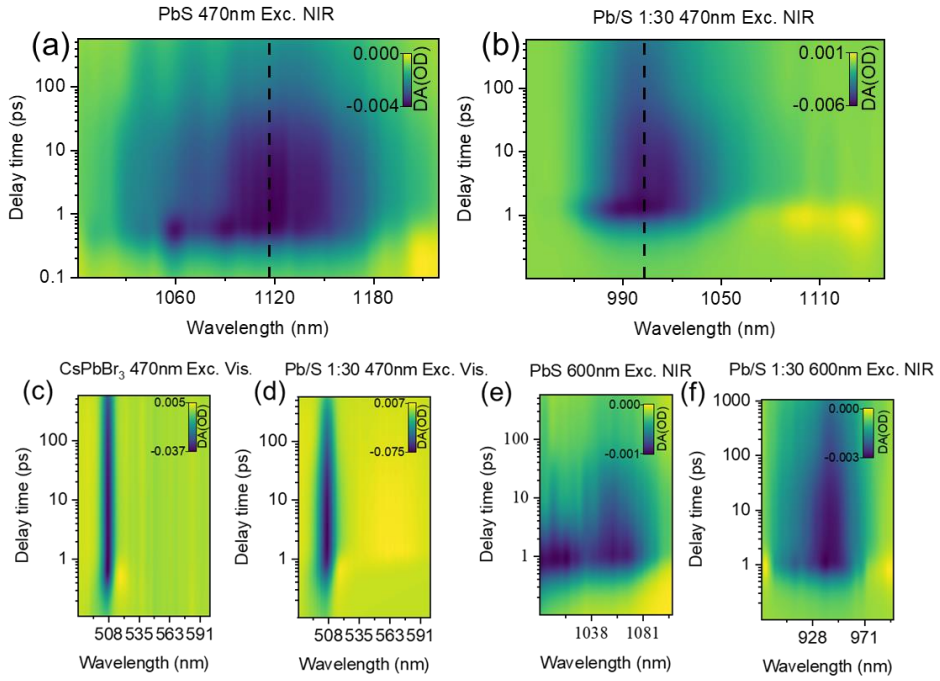

Figure 3-21. Transient absorption spectra (TAS) in the NIR region under 470 nm pump

for PbS QDs (a) and Pb/S 1:30 heterostructures (b), pump light intensity: 6.72 μJ/cm^2. (c-d) Transient absorption spectra (TAS) in the visible region under 470 nm pump for $CsPbBr_3$ QDs (c) and Pb/S 1:30 heterostructures (d), pump light intensity: 6.03 μJ/cm^2. It is crucial to emphasize that the absence of a significant blue shift in Pb/S 1:30 heterostructures is due to the immediate execution of the TAS measurements after sample synthesis, without undergoing a 10-day waiting period, as done in the fluorescence tests. (e-f) Transient absorption spectra (TAS) in the near infrared region under 600 nm pump for PbS QDs (e) and Pb/S 1:30 heterostructures (f), pump light intensity: 12.30 μJ/cm^2.

We extracted the TAS curves of these samples at 1ps, as illustrated in Figure 3-22. The GSB observed in different samples accompanied by certain peak shifts, primarily attributed to the quantum dot size effect, consistent with the conclusions drawn from the steady-state spectroscopy earlier. As depicted in Figure 3-23 (470nm Exc. probe at visible), compared to $CsPbBr_3$ QDs (fuego solid line), the extracted carrier kinetic traces from the TAS clearly reveal a rapid decay segment for the heterostructure (Pb/S ratio is 1:30, indigo solid line). By fitting the decay curve with exponential function, we obtain the fast time component τ_1 of 0.52 ps for Pb/S 1:30 heterostructures, whereas the corresponding τ_1 for $CsPbBr_3$ QDs is 8.08 ps. We attribute the remarkably rapid decay period in the heterostructure (Pb/S 1:30 heterostructures) to the existence of a carrier transfer from $CsPbBr_3$ to PbS. The other two slow decay periods could be possibly caused by the intrinsic carrier recombination (Figure 3-23 a, Table 3-3 for detailed results).

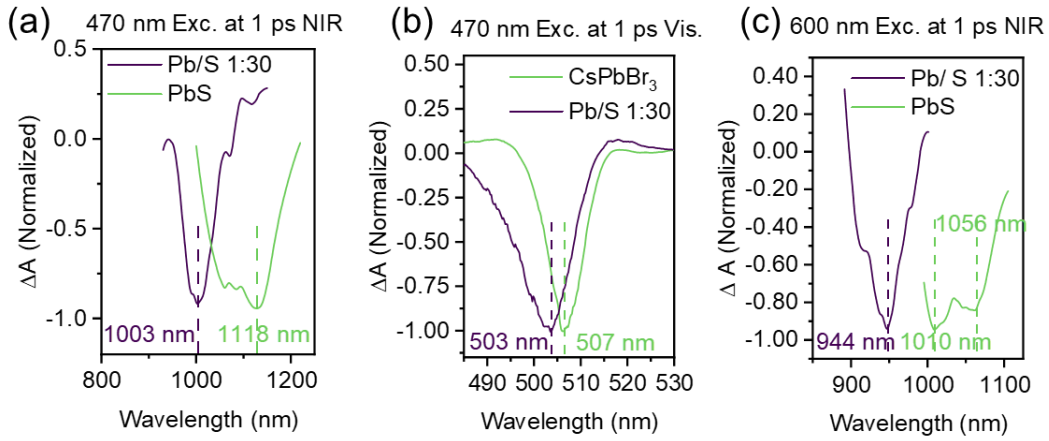

Figure 3-22. (a) TAS spectra of Pb/S 1:30 heterostructures (indigo solid line) and PbS QDs (fuego solid line) at 1 ps, pump light: 470 nm, pump light intensity: 6.72 μJ/cm^2. Both exhibit distinct ground-state bleach signals (GSB), the slight shift in peak position is attributed to the quantum size effect. (b) TAS spectra of Pb/S 1:30 heterostructures (indigo solid line) and $CsPbBr_3$ QDs (fuego solid line) at 1 ps, pump light: 470 nm, pump light intensity: 6.03 μJ/cm^2. They All exhibit distinct ground-state bleach signals (GSB). The slight shift in peak position is attributed to the quantum size effect. (c) TAS spectra of Pb/S 1:30 heterostructures (indigo solid line) and PbS QDs (fuego solid line) at 1 ps, pump light: 600 nm, pump light intensity: 12.30 μJ/cm^2.

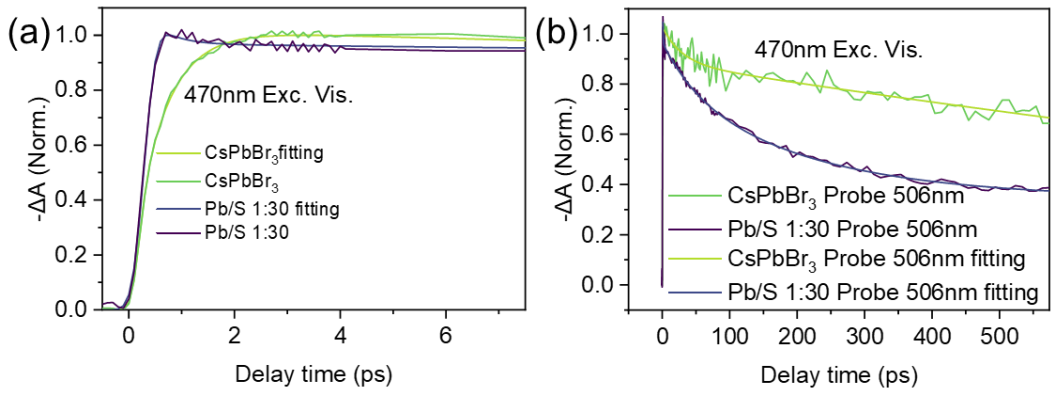

Figure 3-23. (a) Decay kinetic curves extracted for $CsPbBr_3$ QDs (fuego solid line), pump light: 470 nm, probe light: 508 nm, pump light intensity: 6.03 μJ/cm^2; Pb/S 1:30 heterostructures (indigo solid line), pump light: 470 nm, probe light: 503 nm, pump light intensity: 6.03 μJ/cm^2. (b) Kinetics curves extracted for $CsPbBr_3$ QDs (fuego solid line), pump light: 470 nm, probe light: 508 nm, pump light intensity: 6.03 μJ/cm^2; Pb/S

1:30 heterostructures (indigo solid line) pump light: 470 nm, probe light: 503 nm, pump light intensity: 6.03 μJ/cm^2.

Table 3-3. The data obtained through three-exponential function fitting under 470nm pump, visible probe

Vis. (470 nm Exc.)	A_1(%)	T_1(ps)	A_2(%)	T_2(ps)
$CsPbBr_3$	9.27	8.08	90.73	Inf.(>1ns)
Pb/S 1:30	47.46	0.52	52.55	Inf.(>1ns)

Furthermore, more compelling evidence comes from the comparison of the rising kinetic traces of Pb/S 1:30 heterostructures and PbS QDs (470nm Exc. probe at NIR). As depicted in Figure 3-24 a (upper plane), comparing with the approximately 0.30 ps rise time of PbS QDs (fuego solid line), Pb/S 1:30 heterostructures exhibit a slower rise time of about 0.55ps (indigo solid line), which unequivocally demonstrates the carrier injection from $CsPbBr_3$ to PbS QDs. Combining with Figure 3e, we can deduce that the interdot carrier transfer has already occurred within 1 ps. This expedient transfer will significantly enhance the carrier population on PbS QDs, consequently elevating the luminescence intensity. Furthermore, the extremely fast transfer time can be attributed to two reasons: (1) the excellent alignment of energy levels between $CsPbBr_3$ and PbS QDs[38]; (2) the tight coupling of the two components in our in-situ synthesis of heterostructures. It should be noted that, the decay kinetic traces probed at NIR also revealed the slower decay time component (τ_1 = 0.95 ps) for Pb/S 1:30 heterostructures

compared to PbS QDs (Figure 3-24 b, Table 3-4), which indicates the continuous carrier injection from $CsPbBr_3$ QDs to PbS QDs in the heterostructures. The identical rising kinetics for heterostructures (Pb/S ratio is 1:30) and PbS QDs, as shown in Figure 3-24 a (bottom plane, 600nm Exc. probe at NIR), excludes any interference arising from the differences in PbS QDs.

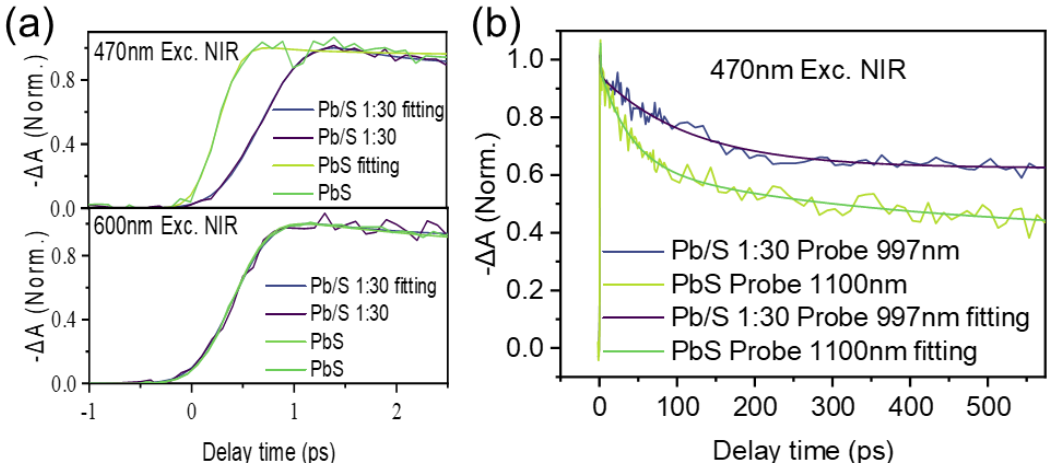

Figure 3-24. (a) Rising kinetic curves extracted for PbS QDs (fuego solid line), pump light: 470 nm, probe light: 1056 nm, pump light intensity: 6.03 μJ/cm^2; Pb/S 1:30 heterostructures (indigo solid line) pump light: 470 nm, probe light: 940 nm, pump light intensity: 6.03 μJ/cm^2 (upper plane), where Pb/S 1:30 heterostructures display a slower rising process. Rising kinetic curves extracted for PbS QDs (fuego solid line), pump light: 600 nm, probe light: 940 nm, pump light intensity: 12.30 μJ/cm^2; Pb/S 1:30 heterostructures (indigo solid line), pump light: 600 nm, probe light: 1050 nm, pump light intensity: 12.30 μJ/cm^2 (bottom plane). (b) Kinetics curves extracted for PbS QDs (fuego solid line), pump light: 470 nm, probe light: 1056 nm, pump light intensity: 6.03 μJ/cm^2; Pb/S 1:30 heterostructures (indigo solid line) pump light: 470 nm, probe light: 940 nm, pump light intensity: 6.03 μJ/cm^2.

Table 3-4. The data obtained through three-exponential function fitting under 470nm pump, NIR probe

NIR (470 nm Exc.)	A_1(%)	T_1(ps)	A_2(%)	T_2(ps)
PbS	54.96	0.32	45.03	Inf.(>1ns)
Pb/S 1:30	41.82	0.95	58.18	Inf.(>1ns)

As additional evidence, we emphasize that the TRPL spectra also illustrate the efficient carrier transfer from $CsPbBr_3$ to PbS QDs (Figure 3-25). 2D contour plots of time-resolved fluorescence spectra illustrate the absence of additional defects introduced during the formation of the heterostructures, as evidenced by their remarkable energy uniformity (Figure 3-25 a-f). We conducted fluorescence lifetime measurements on pure PbS, $CsPbBr_3$ QDs, and the all-CQD heterostructures in both the NIR and vis. regions. By employing dual-component exponential decay fitting, we obtained average lifetimes that indicate a gradual increase in NIR region and a decrease in vis region with an increasing Pb/S ratio (Figure 3-25 g-i). The observed variations in fluorescence lifetimes are attributed to the effective carriers transfer between $CsPbBr_3$ and PbS QDs. The conclusions drawn from the extracted fluorescence lifetimes in the 2D contour plot support the same findings. The slight redshift observed in almost all samples can be attributed to unavoidable testing errors caused by instrument noise resulting from the lower excitation photon energy (Figure 3-25 j).

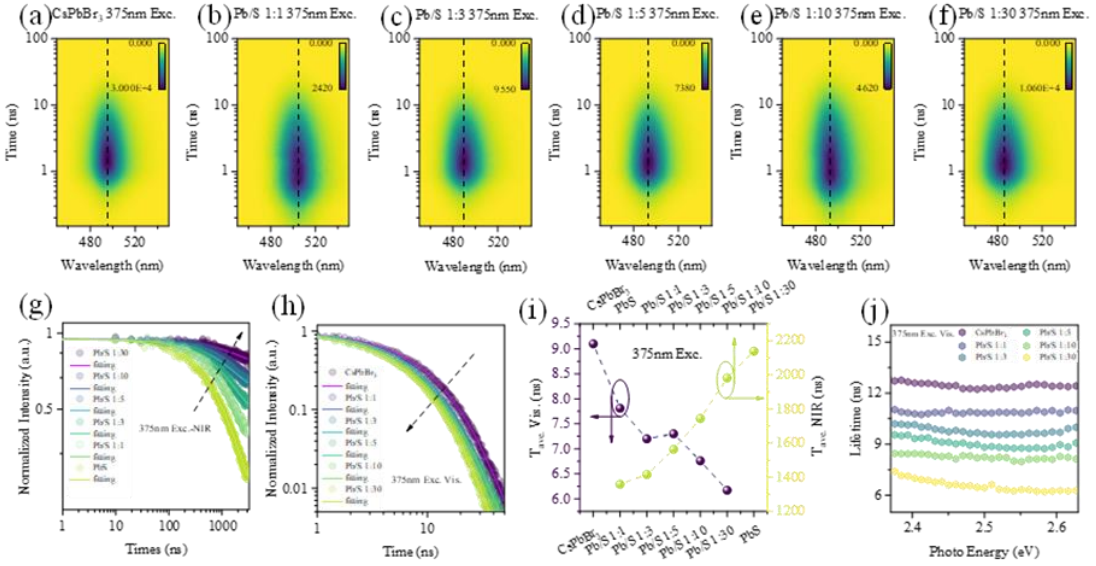

Figure 3-25. (a-f) 2D contour plots of time-resolved photoluminescence spectra under 375 nm excitation for different samples, demonstrating excellent energy homogeneity. (g) Fluorescence lifetimes in the near-infrared region under 375 nm excitation. (h) Fluorescence lifetimes in the visible region under 375 nm excitation. (i) Average lifetime obtained from the biexponential fit. (j) Fluorescence lifetimes in the visible region for all samples at different photon energies, extracted from the two-dimensional contour plots of time-resolved photoluminescence spectra.

The successful construction of all-CQD heterostructures and their efficient carrier transfer have enhanced the optical response of PbS QDs in the ultraviolet-visible (UV-Vis) range and the fluorescence in the NIR region, opening up possibilities for their application in high-performance short-wavelength infrared (SWIR) imaging. The SWIR technology based on chalcogenide QDs has been already reported[23, 41-43].In general, this technology primarily relies on expensive infrared lasers as light sources[44]. Here, we made the first attempt to explore SWIR imaging using low-cost processing all colloidal quantum dot $CsPbBr_3$-PbS heterostructures with ultra-violet light source. In order to explore this potential application, we first examined the structural stability of

our heterostructures. As shown in Figure 3-26, under continuous irradiation from AM 1.5G solar light for 180 hours, the absorption in the visible region for the Pb/S 1:30 heterostructures exhibited almost no decrease. The Pb/S 1:1 heterostructure showed an initial reduction of 9%, while $CsPbBr_3$ QDs exhibited an initial reduction of 16%. In the NIR region, the absorption of the Pb/S 1:30 heterostructures still almost no decrease. In addition, the fluorescence measurements demonstrated the same trend as the abs. spectrum. (Figure 3-27). These results highlight the remarkable structural stability of the all-CQD $CsPbBr_3$-PbS heterostructures, greatly enhancing its prospects for application. The stability of the heterostructure improves with the increasing PbS component, possibly from the thermodynamically favorable microscopic structure at lower Pb/S ratios[45-46]

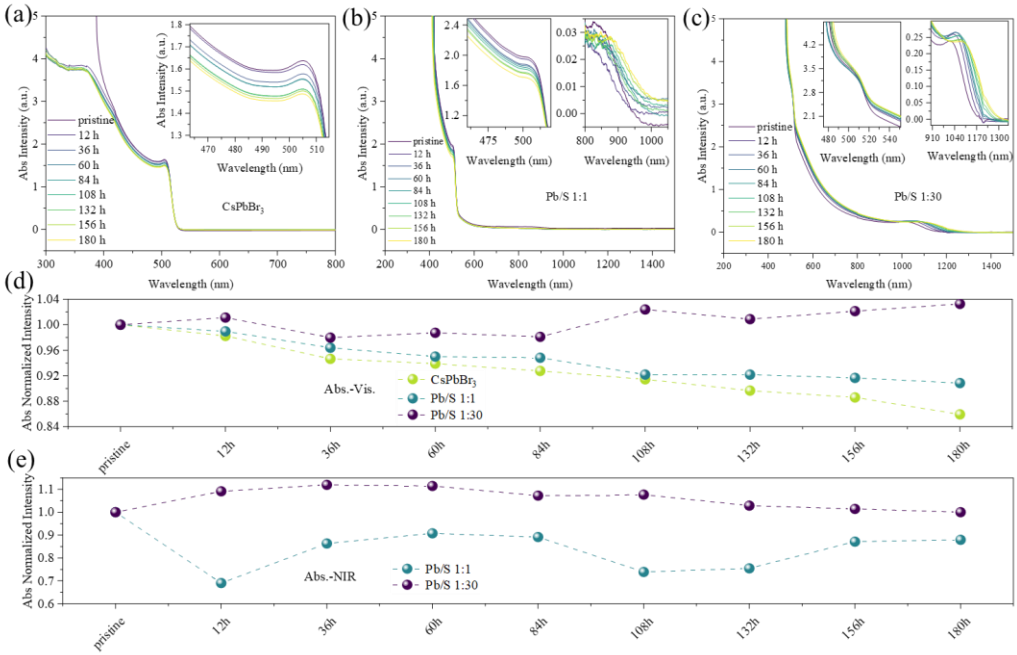

Figure 3-26. Structural stability testing represented by absorption spectra. (a) $CsPbBr_3$ (b) Pb/S 1:1 heterostructure (c) Pb/S 1:30 heterostructure. The inset shows magnified absorption in the visible and NIR regions. (d) Comparison of absorbance in the visible

region extracted from (a), (b), and (c). (e) Comparison of absorbance in the visible region extracted from (b) and (c). Both in the visible and near-infrared regions, the absorbance of heterostructure nanoparticles demonstrates excellent stability, highlighting the structural stability of these nanoparticles.

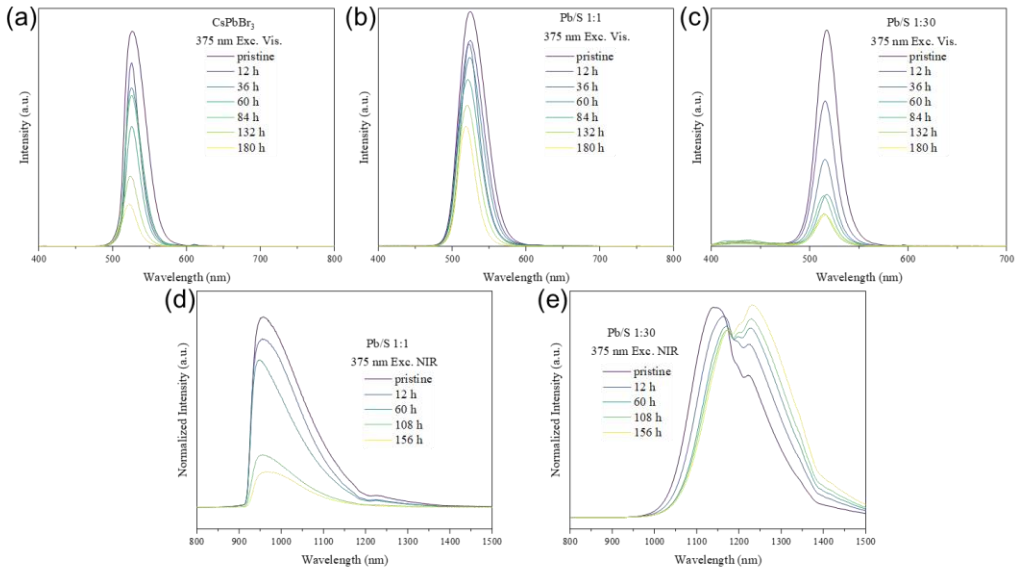

Figure 3-27. Structural stability represented by fluorescence spectra. (a-c) Changes in fluorescence intensity in the visible region: (a) $CsPbBr_3$ (b) Pb/S 1:1 heterostructure (c) Pb/S 1:30 heterostructures (d-e) Changes in fluorescence intensity in the infrared region: (d) Pb/S 1:1 heterostructure (e) Pb/S 1:30 heterostructures. We gently emphasize that the lack of a significant blue shift in the visible fluorescence of Pb/S 1:30 heterostructures over time can be attributed to the possible occurrence of quantum dot fusion and growth induced by the high-energy input from standard solar light. This fusion and growth process might counterbalance the etching effect caused by the excessive supply of sulfur sources.

3.3.4 SWIR imaging of colloidal quantum dot $CsPbBr_3$-PbS heterostructures

As shown in Figure 3-28, a simple SWIR imaging system was constructed. In order to evaluate the SWIR imaging performance, the “Panda” pattern was created by mixing the $CsPbBr_3$ QDs with polymethyl methacrylate (PMMA) (Figure 3-28 a) and "UEC" patterns were created by mixing all-CQD $CsPbBr_3$-PbS heterostructures (Figure 3-28 c), PbS QDs (Figure 3-28 e) with PMMA, respectively. In the visible imaging mode, the "Panda" pattern exhibited a bright visible fluorescence under 365 nm excitation (Figure 3-28 b). On the other hand, the "UEC" pattern made of all-CQD $CsPbBr_3$-PbS heterostructures only displayed weak fluorescence pattern due to efficient charge carrier transfer (Figure 3-28 d). Conversely, the "UEC" pattern made of PbS QDs showed no fluorescence (Figure 3-28 f). However, in the NIR imaging mode (probe range 800-1400 nm), with an excitation power density of approximately 18 mW/cm^2, the all-CQD heterostructures exhibited an NIR imaging pattern of "UEC" with rich details, high clarity, and excellent resolutions (resolution limit is ~ 3.44 μm) as shown in Figure 3-28 i, which demonstrates the enormous potential of all-CQD heterostructures in the field of SWIR imaging. In contrast, pure PbS QDs only showed a blurry pattern outline (Figure 3-28 j), while pure $CsPbBr_3$ QDs displayed a blank background-like pattern (Figure 3-28 g, h). As demonstrated by our engineered SWIR system, our all-CQD $CsPbBr_3$-PbS heterostructures exhibiting superior imaging capabilities due to the efficient carrier transfer. This advancement is poised to catalyze the development of

SWIR devices and other electronic equipment based on all-CQD $CsPbBr_3$-PbS heterostructure.

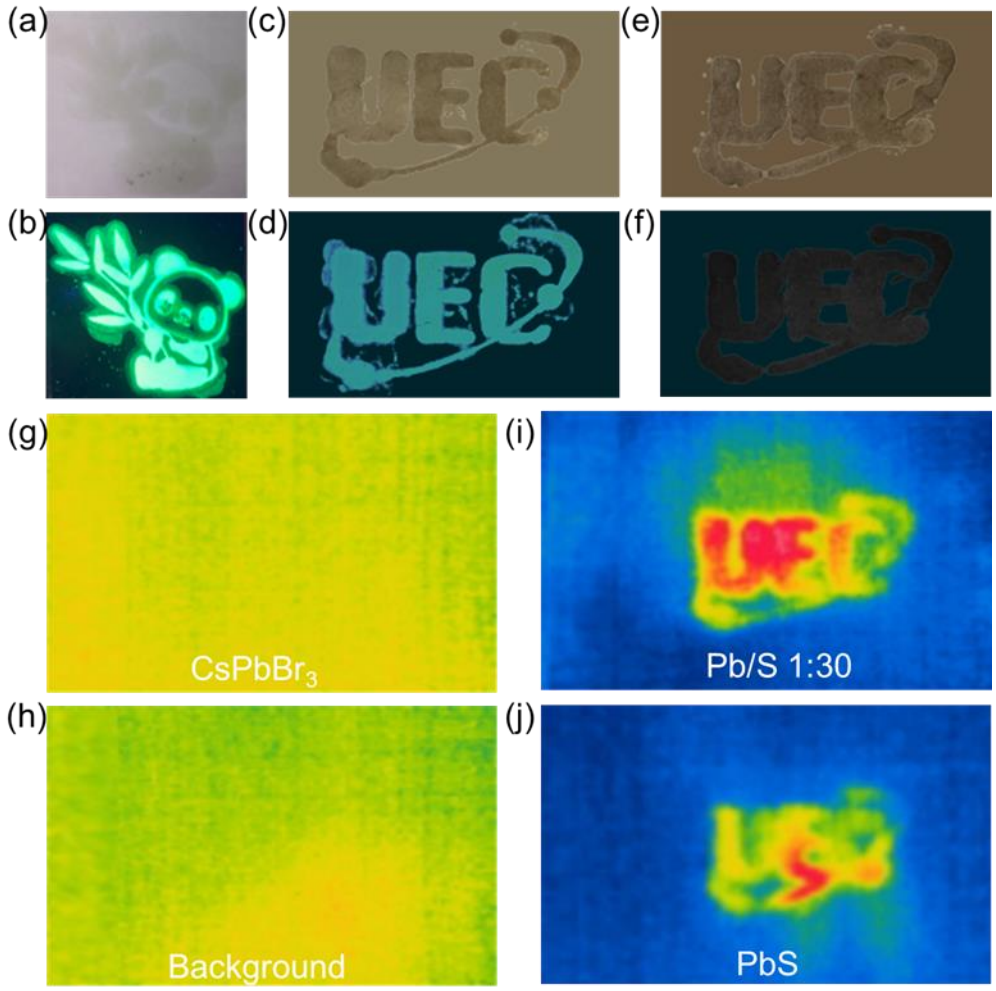

Figure 3-28. The fabricated SWIR imaging system. (a) Visible image of the "Panda" pattern made of $CsPbBr_3$ QDs under sunlight. (b) Visible imaging mode of the "Panda" pattern made of $CsPbBr_3$ QDs under 365 nm excitation. (c) Visible image of the "UEC" pattern made of Pb/S 1:30 heterostructures under sunlight. (d) Visible imaging mode of the "UEC" pattern made of Pb/S 1:30 heterostructures heterostructures under 365 nm excitation. (e) Visible image of the "UEC" pattern made of PbS QDs under sunlight. (f) Visible imaging mode of the "UEC" pattern made of PbS QDs under 365 nm excitation. (g) NIR imaging mode of the "Panda" pattern made of $CsPbBr_3$ QDs under 365 nm excitation. The image shows no discernible features, appearing similar to a blank background. (h) NIR imaging mode of the blank background. (i) NIR imaging mode of

the "UEC" pattern made of Pb/S 1:30 heterostructures under 365 nm excitation. (j) NIR imaging mode of the "UEC" pattern made of PbS QDs under 365 nm excitation.

3.4 Summary

In summary, we have developed an uncomplicated and reproducible room-temperature in-situ synthesis approach for controllable and low-cost processing all-colloidal CQD $CsPbBr_3$-PbS nanocrystal heterostructures, deriving from thoughtful considerations of the conditions for in-situ heterostructure synthesis. The size and spectral characteristics of the dual QD components incorporated in our heterostructure are observed to be highly tunable, modulated by varying the Pb/S ratio. Employing ultrafast transient absorption spectroscopy (TAS), we unveiled the carrier transfer dynamics within our heterostructures, demonstrating a swift carrier injection initiation time (<1ps) from $CsPbBr_3$ to PbS QDs. Furthermore, we made the first attempt to utilize all-CQD $CsPbBr_3$-PbS heterostructures in short-wave infrared (SWIR) imaging; which displayed an outstanding imaging quality and resolution surpassing those of pure PbS QDs under an excitation of 365 nm with a power density of 18 mW/cm^2. The insights garnered from our study offer a valuable, repeatable methodology for the synthesis of all-CQD heterostructures, opening up avenues for advancements in applications.

3.5 Bibliography

1. García de Arquer, F. P.; Talapin, D. V.; Klimov, V. I.; Arakawa, Y.; Bayer, M.; Sargent, E. H., Semiconductor quantum dots: Technological progress and future challenges. *Science* **2021,** *373* (6555), eaaz8541.

2. Sargent, E. H., Colloidal quantum dot solar cells. *Nature photonics* **2012,** *6* (3),

133-135.

3. Dai, X.; Zhang, Z.; Jin, Y.; Niu, Y.; Cao, H.; Liang, X.; Chen, L.; Wang, J.; Peng, X., Solution-processed, high-performance light-emitting diodes based on quantum dots. *Nature* **2014,** *515* (7525), 96-99.

4. Keuleyan, S.; Lhuillier, E.; Brajuskovic, V.; Guyot-Sionnest, P., Mid-infrared HgTe colloidal quantum dot photodetectors. *Nature Photonics* **2011,** *5* (8), 489-493.

5. Medintz, I. L.; Uyeda, H. T.; Goldman, E. R.; Mattoussi, H., Quantum dot bioconjugates for imaging, labelling and sensing. *Nature materials* **2005,** *4* (6), 435-446.

6. Rajender, G.; Kumar, J.; Giri, P., Interfacial charge transfer in oxygen deficient TiO2-graphene quantum dot hybrid and its influence on the enhanced visible light photocatalysis. *Applied Catalysis B: Environmental* **2018,** *224*, 960-972.

7. Ye, M. Y.; Zhao, Z. H.; Hu, Z. F.; Liu, L. Q.; Ji, H. M.; Shen, Z. R.; Ma, T. Y., 0D/2D heterojunctions of vanadate quantum dots/graphitic carbon nitride nanosheets for enhanced visible-light-driven photocatalysis. *Angewandte Chemie International Edition* **2017,** *56* (29), 8407-8411.

8. Dong, H.; Xu, F.; Sun, Z.; Wu, X.; Zhang, Q.; Zhai, Y.; Tan, X. D.; He, L.; Xu, T.; Zhang, Z., In situ interface engineering for probing the limit of quantum dot photovoltaic devices. *Nature nanotechnology* **2019,** *14* (10), 950-956.

9. Chen, X.; Lin, X.; Zhou, L.; Sun, X.; Li, R.; Chen, M.; Yang, Y.; Hou, W.; Wu, L.; Cao, W., Blue light-emitting diodes based on colloidal quantum dots with reduced surface-bulk coupling. *Nature Communications* **2023,** *14* (1), 284.

10. Kim, T.; Kim, K.-H.; Kim, S.; Choi, S.-M.; Jang, H.; Seo, H.-K.; Lee, H.; Chung, D.-Y.; Jang, E., Efficient and stable blue quantum dot light-emitting diode. *Nature* **2020,** *586* (7829), 385-389.

11. Milliron, D. J.; Hughes, S. M.; Cui, Y.; Manna, L.; Li, J.; Wang, L.-W.; Paul Alivisatos, A., Colloidal nanocrystal heterostructures with linear and branched topology. *Nature* **2004,** *430* (6996), 190-195.

12. Zhao, Q.; Hazarika, A.; Chen, X.; Harvey, S. P.; Larson, B. W.; Teeter, G. R.; Liu,

J.; Song, T.; Xiao, C.; Shaw, L., High efficiency perovskite quantum dot solar cells with charge separating heterostructure. *Nature communications* **2019,** *10* (1), 2842.

13. Yuan, M.; Liu, M.; Sargent, E. H., Colloidal quantum dot solids for solution-processed solar cells. *Nature Energy* **2016,** *1* (3), 1-9.

14. Dutta, A.; Behera, R. K.; Pal, P.; Baitalik, S.; Pradhan, N., Near-unity photoluminescence quantum efficiency for all CsPbX3 (X= Cl, Br, and I) perovskite nanocrystals: a generic synthesis approach. *Angewandte Chemie International Edition* **2019,** *58* (17), 5552-5556.

15. Akkerman, Q. A.; Rainò, G.; Kovalenko, M. V.; Manna, L., Genesis, challenges and opportunities for colloidal lead halide perovskite nanocrystals. *Nature materials* **2018,** *17* (5), 394-405.

16. Mannar, S.; Mandal, P.; Roy, A.; Viswanatha, R., Experimental Determination of the Molar Absorption Coefficient of Cesium Lead Halide Perovskite Quantum Dots. *The Journal of Physical Chemistry Letters* **2022,** *13* (27), 6290-6297.

17. Moreels, I.; Justo, Y.; De Geyter, B.; Haustraete, K.; Martins, J. C.; Hens, Z., Size-tunable, bright, and stable PbS quantum dots: a surface chemistry study. *ACS nano* **2011,** *5* (3), 2004-2012.

18. Ning, Z.; Gong, X.; Comin, R.; Walters, G.; Fan, F.; Voznyy, O.; Yassitepe, E.; Buin, A.; Hoogland, S.; Sargent, E. H., Quantum-dot-in-perovskite solids. *Nature* **2015,** *523* (7560), 324-328.

19. Gao, L.; Quan, L. N.; García de Arquer, F. P.; Zhao, Y.; Munir, R.; Proppe, A.; Quintero-Bermudez, R.; Zou, C.; Yang, Z.; Saidaminov, M. I., Efficient near-infrared light-emitting diodes based on quantum dots in layered perovskite. *Nature Photonics* **2020,** *14* (4), 227-233.

20. Liu, Q.; Liang, L.; Shen, H.; Li, D.; Zhou, H., Epitaxial growth of CsPbBr 3-PbS vertical and lateral heterostructures for visible to infrared broadband photodetection. *Nano Research* **2021**, 1-7.

21. Liu, X.; Wu, Z.; Zhong, H.; Wang, X.; Yang, J.; Zhang, Z.; Han, J.; Oron, D.; Lin, H., Epitaxial 2D PbS Nanosheet-Formamidinium Lead Triiodide Heterostructure

Enabling High-Performance Perovskite Solar Cells. *Advanced Functional Materials* **2023**, 2304140.

22. Zhang, X.; Wu, X.; Liu, X.; Chen, G.; Wang, Y.; Bao, J.; Xu, X.; Liu, X.; Zhang, Q.; Yu, K., Heterostructural CsPbX3-PbS (X= Cl, Br, I) quantum dots with tunable Vis–NIR dual emission. *Journal of the American Chemical Society* **2020,** *142* (9), 4464-4471.

23. Bruns, O. T.; Bischof, T. S.; Harris, D. K.; Franke, D.; Shi, Y.; Riedemann, L.; Bartelt, A.; Jaworski, F. B.; Carr, J. A.; Rowlands, C. J., Next-generation in vivo optical imaging with short-wave infrared quantum dots. *Nature biomedical engineering* **2017,** *1* (4), 0056.

24. Wang, R.; Wang, F.; Zhou, W.; Fan, J. Z.; de Arquer, F. P. G.; Xu, K.; Sargent, E. H.; Ning, Z., Colloidal-quantum-dot-in-perovskite nanowires. *Infrared Physics & Technology* **2019,** *98*, 16-22.

25. Akkerman, Q. A.; Nguyen, T. P.; Boehme, S. C.; Montanarella, F.; Dirin, D. N.; Wechsler, P.; Beiglböck, F.; Rainò, G.; Erni, R.; Katan, C., Controlling the nucleation and growth kinetics of lead halide perovskite quantum dots. *Science* **2022,** *377* (6613), 1406-1412.

26. Liu, Y.; Li, D.; Zhang, L.; Chen, Y.; Geng, C.; Shi, S.; Zhang, Z.; Bi, W.; Xu, S., Amine-and acid-free synthesis of stable CsPbBr3 perovskite nanocrystals. *Chemistry of Materials* **2020,** *32* (5), 1904-1913.

27. Nair, G. B.; Tamboli, S.; Kroon, R.; Dhoble, S.; Swart, H. C., Facile room-temperature colloidal synthesis of CsPbBr3 perovskite nanocrystals by the Emulsion-based ligand-assisted reprecipitation approach: Tuning the color-emission by the demulsification process. *Journal of Alloys and Compounds* **2022,** *928*, 167249.

28. Liang, J.; Hu, X.; Wang, C.; Liang, C.; Chen, C.; Xiao, M.; Li, J.; Tao, C.; Xing, G.; Yu, R., Origins and influences of metallic lead in perovskite solar cells. *Joule* **2022,** *6* (4), 816-833.

29. Blake, P. G.; Carley, A. F.; Di Castro, V.; Roberts, M. W., Chemisorptive replacement of surface oxygen by hydrogen halides (HCl and HBr) at Pb (110) surfaces.

Photoelectron spectroscopic and kinetic evidence for a metastable chloride overlayer. *Journal of the Chemical Society, Faraday Transactions 1: Physical Chemistry in Condensed Phases* **1986,** *82* (3), 723-737.

30. Liu, X.; Ren, S.; Li, Z.; Guo, J.; Yi, S.; Yang, Z.; Hao, W.; Li, R.; Zhao, J., Flexible transparent high-efficiency photoelectric perovskite resistive switching memory. *Advanced Functional Materials* **2022,** *32* (38), 2202951.

31. Ettema, A. R.; Haas, C., An X-ray photoemission spectroscopy study of interlayer charge transfer in some misfit layer compounds. *Journal of Physics: Condensed Matter* **1993,** *5* (23), 3817.

32. Morgan, W. E.; Van Wazer, J. R., Binding energy shifts in the x-ray photoelectron spectra of a series of related Group IVa compounds. *The Journal of Physical Chemistry* **1973,** *77* (7), 964-969.

33. Burungale, V. V.; Devan, R. S.; Pawar, S. A.; Harale, N. S.; Patil, V. L.; Rao, V.; Ma, Y.-R.; Ae, J. E.; Kim, J. H.; Patil, P. S., Chemically synthesized PbS nanoparticulate thin films for a rapid NO2 gas sensor. *Materials Science-Poland* **2016,** *34* (1), 204-211.

34. Ghorai, A.; Mahato, S.; Singh, S.; Bose, S.; Roy, B.; Jeong, U.; Kumar Ray, S., Ligand-Mediated Revival of Degraded α-CsPbI3 to Stable Highly Luminescent Perovskite. *Angewandte Chemie* **2023,** *135* (22), e202302852.

35. Krieg, F.; Ong, Q. K.; Burian, M.; Rainò, G.; Naumenko, D.; Amenitsch, H.; Süess, A.; Grotevent, M. J.; Krumeich, F.; Bodnarchuk, M. I., Stable ultraconcentrated and ultradilute colloids of CsPbX3 (X= Cl, Br) nanocrystals using natural lecithin as a capping ligand. *Journal of the American Chemical Society* **2019,** *141* (50), 19839-19849.

36. Costa, W. C.; Salla, C. A.; Ely, F.; Bechtold, I. H., Highly emissive MAPbBr3 perovskite QDs by ligand-assisted reprecipitation: The antisolvent effect. *Nanotechnology* **2021,** *33* (9), 095702.

37. Cademartiri, L.; Montanari, E.; Calestani, G.; Migliori, A.; Guagliardi, A.; Ozin, G. A., Size-dependent extinction coefficients of PbS quantum dots. *Journal of the American Chemical Society* **2006,** *128* (31), 10337-10346.

38. Jung, Y.-K.; Butler, K. T.; Walsh, A., Halide perovskite heteroepitaxy: bond formation and carrier confinement at the PbS–CsPbBr3 interface. *The Journal of Physical Chemistry C* **2017,** *121* (49), 27351-27356.

39. Jasieniak, J.; Califano, M.; Watkins, S. E., Size-dependent valence and conduction band-edge energies of semiconductor nanocrystals. *ACS nano* **2011,** *5* (7), 5888-5902.

40. Liu, Q.; Yin, J.; Zhang, B.-B.; Chen, J.-K.; Zhou, Y.; Zhang, L.-M.; Wang, L.-M.; Zhao, Q.; Hou, J.; Shu, J., Theory-guided synthesis of highly luminescent colloidal cesium tin halide perovskite nanocrystals. *Journal of the American Chemical Society* **2021,** *143* (14), 5470-5480.

41. Wu, Z.; Ou, Y.; Cai, M.; Wang, Y.; Tang, R.; Xia, Y., Short-Wave Infrared Photodetectors and Imaging Sensors Based on Lead Chalcogenide Colloidal Quantum Dots. *Advanced Optical Materials* **2023,** *11* (1), 2201577.

42. Zhang, H.; Sun, C.; Sun, L.; Xu, W.; Wu, W.; Chen, J.; Wang, B.; Yu, J.; Cui, P.; Zhang, F., Stable Monodisperse Pb1− xCdxS Quantum Dots for NIR-II Bioimaging by Aqueous Coprecipitation of Bimetallic Clusters. *Angewandte Chemie* **2022,** *134* (37), e202203851.

43. Kamath, A.; Schaller, R. D.; Guyot-Sionnest, P., Bright Fluorophores in the Second Near-Infrared Window: HgSe/CdSe Quantum Dots. *Journal of the American Chemical Society* **2023,** *145* (19), 10809-10816.

44. Lee, G.; Jeong, W. H.; Kim, B.; Jeon, S.; Smith, A. M.; Seo, J.; Suzuki, K.; Kim, J. y.; Lee, H.; Choi, H., Design and Synthesis of CdHgSe/HgS/CdZnS Core/Multi-Shell Quantum Dots Exhibiting High-Quantum-Yield Tissue-Penetrating Shortwave Infrared Luminescence. *Small* **2023**, 2301161.

45. Jagadeeswararao, M.; Vashishtha, P.; Hooper, T. J.; Kanwat, A.; Lim, J. W. M.; Vishwanath, S. K.; Yantara, N.; Park, T.; Sum, T. C.; Chung, D. S., One-Pot Synthesis and Structural Evolution of Colloidal Cesium Lead Halide–Lead Sulfide Heterostructure Nanocrystals for Optoelectronic Applications. *The Journal of Physical Chemistry Letters* **2021,** *12* (39), 9569-9578.

46. Masi, S.; Echeverría-Arrondo, C.; Salim, K. M.; Ngo, T. T.; Mendez, P. F.; López-

Fraguas, E.; Macias-Pinilla, D. F.; Planelles, J.; Climente, J. I.; Mora-Sero, I., Chemi-structural stabilization of formamidinium lead iodide perovskite by using embedded quantum dots. *ACS Energy Letters* **2020,** *5* (2), 418-427.

Chapter 4 In-situ epitaxial growth of 2D-3D perovskite nanocrystal horizontally heterojunctions

4.1 Introduction

Colloidal metal halide perovskite nanocrystals (PNCs) have emerged as promising optoelectronic materials in fields such as solar cells, light-emitting diodes, detectors, photocatalysis, and optical imaging[1-5], owing to their inherent high absorption coefficients, high defect tolerance, high color purity, high photoluminescence quantum efficiency, and excellent charge carrier transport properties[6-9]. These intrinsic properties, dependent on the composition, dimensions, size, and surface chemistry of PNCs, can be further modulated through the formation of heterostructures. By adjusting different combinations of heterostructure types, carrier recombination or separation can be facilitated, allowing precise applications in various subfields. As a result, heterostructures serve as a platform, offering superior properties compared to single nanocrystals (NCs) and enhancing the performance of optoelectronic devices across various domains.

In recent years, heterostructures formed by three-dimensional (3D) and two-dimensional (2D) perovskite have garnered significant attention due to their enhanced carrier separation characteristics and stabilized defects at the passivated interface[10-13]. Researchers have made notable progress in the construction and application of 2D-3D

perovskite heterostructures. In 2016, Hu et al. achieved a significant milestone by coating a mixture of methylammonium iodide (MAI), n-butylammonium iodide (BAI), and phenethylammonium iodide (PEAI) on a 3D perovskite ($MAPbI_3$) film, forming a 2D-3D perovskite heterostructure. This led to an increase in the photovoltaic conversion efficiency (PCE) from 13.61% (control group) to 14.94%, marking a crucial advancement[14]. Through continuous optimization, solar cells based on 2D-3D perovskite film heterostructures have achieved an impressive PCE of 24.7%[15]. Simultaneously, efficient photodetectors based on 2D-3D perovskite film heterostructures have been developed[16]. However, solution-processed 2D-3D perovskite polycrystalline film heterostructures exhibit poor compositional and structural uniformity, making it challenging to understand the formation mechanisms and control the interfaces. Addressing these challenges, in 2022, Zhu et al. demonstrated the possibility of in-depth research in this field by directly mixing $CsPbBr_3$ and PEA_2PbBr_4 nanocrystals to prepare 2D-3D perovskite nanocrystal heterostructures[17]. Nevertheless, using hydrogen bonding as the bonding method between heterostructures typically results in poor stability and conductivity, posing challenges for industrial applications. Additionally, from a synthetic chemistry and optical physics perspective, developing a low-cost, reproducible method with chemical bonding as the bonding method between heterostructure surfaces, displaying rapid carrier transfer, remains a significant challenge to unleash its potential in applications.

Here, we present, for the first time, the thermodynamically controlled, solution-processed, room-temperature, in situ epitaxial growth of 2D-3D PMA_2PbBr_4-$CsPbBr_3$

nanocrystal horizontally heterojunctions. The synthesis of the heterojunctions involves rapidly injecting a precursor solution of CsBr, $PbBr_2$, PMA (phenylmethylamine), and BA (benzoic acid) dissolved in a good solvent into a poor solvent. During the growth process, $CsPbBr_3$ nanocrystals induce the binding of free PMA^+ and lead bromide ions in the solution, triggering the thermodynamically stable in situ growth of PMA_2PbBr_4 on the surface of $CsPbBr_3$. The result is a direct connection of $[PbBr_4]^{6-}$ octahedra of the two components, avoiding the insulating barrier of the organic cation. The successful synthesis of 2D-3D PMA_2PbBr_4-$CsPbBr_3$ nanocrystal horizontally heterojunctions were confirmed through analytical methods such as scanning transmission electron microscopy (STEM), X-ray diffraction (XRD), grazing-incidence wide-angle X-ray scattering (GI-WAXs), and X-ray photoelectron spectroscopy (XPS). Density functional theory (DFT) calculations theoretically support the conclusion that the formation of the heterojunction is governed by thermodynamics. Temperature-dependent fluorescence spectra reveal strong chemical bonding at the interface, introducing significant lattice distortion in PMA_2PbBr_4. Furthermore, through time-resolved photoluminescence spectra (TRPL) and transient absorption spectra (TAS), we demonstrate ultrafast carrier transfer in the heterostructure. Our work provides an innovative pathway for constructing lateral heterojunctions of 2D-3D nanocrystals directly connected by $[PbBr_4]^{6-}$ octahedra. As an excellent platform for studying their synthetic chemistry and optical properties, our research paves the way for their future applications.

4.2 Experimental methods

Chemicals: Cesium bromide (CsBr, 99%), Lead bromide ($PbBr_2$, 99.99%), hexane (≥99%), Benzylamine (PMA), Benzoic acid (BA), N, N-dimethylformamide (DMF), Dimethyl sulfoxide (DMSO) and bromobenzene were purchased from Sigma Aldrich. Toluene, hexane, chlorobenzene (99%), and ethyl acetate were purchased from Wako. All chemicals were used as received without further purification.

Synthesis of PMA_2PbBr_4-$CsPbBr_3$ nanocrystal horizontally heterojunctions: The synthesis of PMA_2PbBr_4-$CsPbBr_3$ nanocrystal horizontally heterostructures entails the dissolution of 0.4 mmol CsBr, 2 mmol $PbBr_2$, 1 mmol PMA, and 7.4 mmol BA in a 1:1 volume ratio mixture of 4 ml DMF and DMSO. Subsequently, 200 µl of this solution is rapidly injected into 10 ml of bromobenzene, under continuous stirring at room temperature. The solution undergoes an immediate transformation into a yellow-green hue. After 1 minute, stirring is halted, yielding the crude solution of PMA_2PbBr_4-$CsPbBr_3$ nanocrystal lateral heterostructures. The comprehensive procedure is delineated in Figure 4-1:

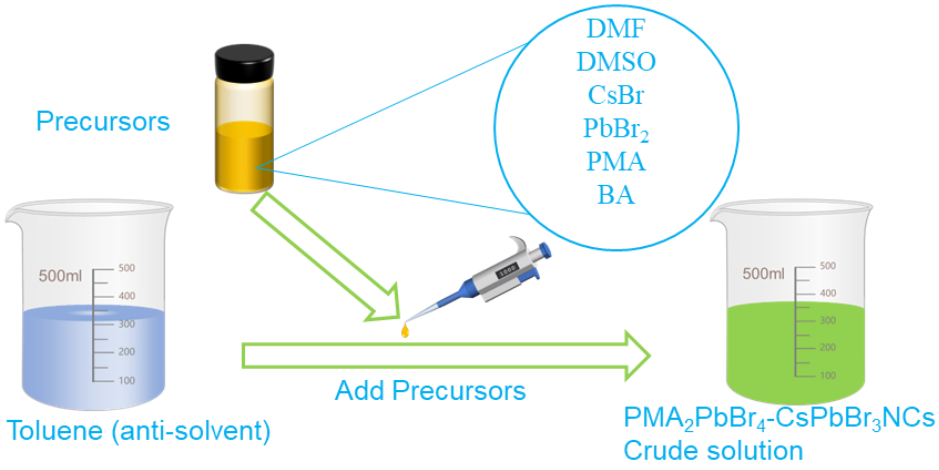

Figure 4-1. Schematic of PMA_2PbBr_4-$CsPbBr_3$ nanocrystal horizontally

heterojunctions

Purification of PMA_2PbBr_4-$CsPbBr_3$ nanocrystal horizontally heterojunctions: The crude solution of PMA_2PbBr_4-$CsPbBr_3$ nanocrystal lateral heterostructures is subjected to purification by adding ethyl acetate in a 1:3 volume ratio. The mixture is vigorously oscillated and then centrifuged at 8000 rpm for 5 minutes and 30 seconds. The resulting precipitate is redispersed in 2 ml of chlorobenzene, followed by uniform oscillation and centrifugation at 6000 rpm for 5 minutes and 30 seconds. The supernatant is collected and centrifuged at 4000 rpm for an additional 5 minutes and 30 seconds. Ultimately, the obtained precipitate is redispersed in 2 ml of chlorobenzene for further testing and analysis.

Preparation of PMA_2PbBr_4-$CsPbBr_3$ nanocrystal horizontally heterojunctions Thin Films: The thin films of PMA_2PbBr_4-$CsPbBr_3$ nanocrystal lateral heterostructures are fabricated using a modified centrifugal deposition method. In summary, the purified nanocrystal lateral heterostructure solution is diluted to 10 ml in a 50 ml centrifuge tube with chlorobenzene and then deposited onto a UV-ozone-treated quartz glass or FTO substrate measuring 1.2*1.2 cm. Subsequently, centrifugation is performed at 8000 rpm for 30 minutes, yielding the final nanocrystal lateral heterostructure thin films. The detailed procedure is illustrated in Figure 4-2:

Figure 4-2. Schematic of PMA_2PbBr_4-$CsPbBr_3$ nanocrystal horizontally heterojunctions Thin Films

Preparation of Ligand-Exchanged $CsPbBr_3$ Nanocrystal Thin Films: The fabrication of ligand-exchanged nanocrystal thin films is achieved through a modified spin-coating method. In essence, 45 µl of the purified quantum dot solution is drop-cast onto a UV-ozone-treated quartz glass or FTO substrate. The rotation is initiated at 2000 rpm for 20 seconds, followed by the addition of 100 µl of methyl acetate solution. After a brief pause at 0 rpm for 5 seconds, the rotation is resumed at 2000 rpm for an additional 30 seconds. The detailed procedure is outlined in Figure 4-3:

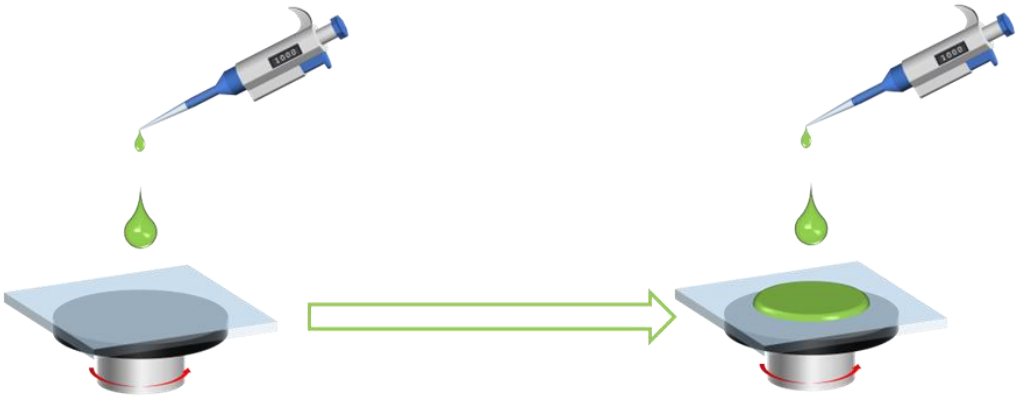

Figure 4-3. Schematic of Ligand-Exchanged $CsPbBr_3$ Nanocrystal Thin Films

DFT Calculation: The density functional theory (DFT) calculations have been performed using the Vienna *Ab Initio* Simulation Package (VASP). The projected augmented wave (PAW) method within a plane-wave basis set with a cut-off energy of 500 eV has been adopted for all static DFT calculations. We use the generalized gradient approximation (GGA) with the Perdew–Burke–Ernzerhof functional (PBE) form to approximate the exchange and correlation interactions. We constructed a heterojunction by building a supercell on the surface of $CsPbBr_3$ (111) surface and PMA_2PbBr_4 (005)

surface .and relax all the interatomic forces to less than 0.03 eV $Å^{-1}$ during internal structural optimization. We further use the DFT-D_3 method as described by Grimme and a 1 × 2 × 1 *Γ*-centered Monkhorst–Pack mesh for all the 2D-perovskites. We employed VASPKIT to assist in processing the data obtained from VASP.

4.3 Results and discussions

4.3.1 synthesis 2D-3D perovskite nanocrystal horizontally heterojunctions

In pursuit of realizing the horizontally heterostructure of 2D-3D perovskite nanocrystals (2D-3D PNC), it is imperative to ensure the nucleation of 3D perovskite while concurrently inducing the nucleation of 2D perovskite. The crux lies in achieving heterogeneous nucleation of 2D perovskite rather than homogeneous nucleation. Additionally, to ensure the stability of the heterostructure, a thermodynamically controlled reaction pathway is essential to obtain stable nanocrystal heterostructures. As illustrated in Figure 4-4 a, we opt for an improved room-temperature recrystallization method for the synthesis of $CsPbBr_3$ nanocrystals. The reaction conducted at room temperature ensures that the entire reaction system remains in a thermodynamically stable state throughout the process[18]. Crucially, we refrain from introducing traditional long-chain capping ligands to terminate the reaction. This decision preserves the highly reactive and accessible nature of the $CsPbBr_3$ nanocrystal surface. Building upon this foundation, we explore control experiments by omitting the

Cs source, as depicted in Figure 4-4 (b-d). The absence of a recrystallization process post addition of the precursor solution and the lack of absorption peaks corresponding to PMA_2PbBr_4 in the absorption spectra further affirm that PMA_2PbBr_4 undergoes heterogeneous nucleation solely with $CsPbBr_3$ as the seed. The PMA_2PbBr_4 induced by $CsPbBr_3$ nanocrystals forms heterostructures in situ on the $CsPbBr_3$ surface, driven by crystal face matching, effectively terminating the reaction. Ultimately, the two components of 2D-3D PMA_2PbBr_4-$CsPbBr_3$ PNC combine through direct coordination of $[PbBr_4]^{6-}$ octahedra, extending in space.

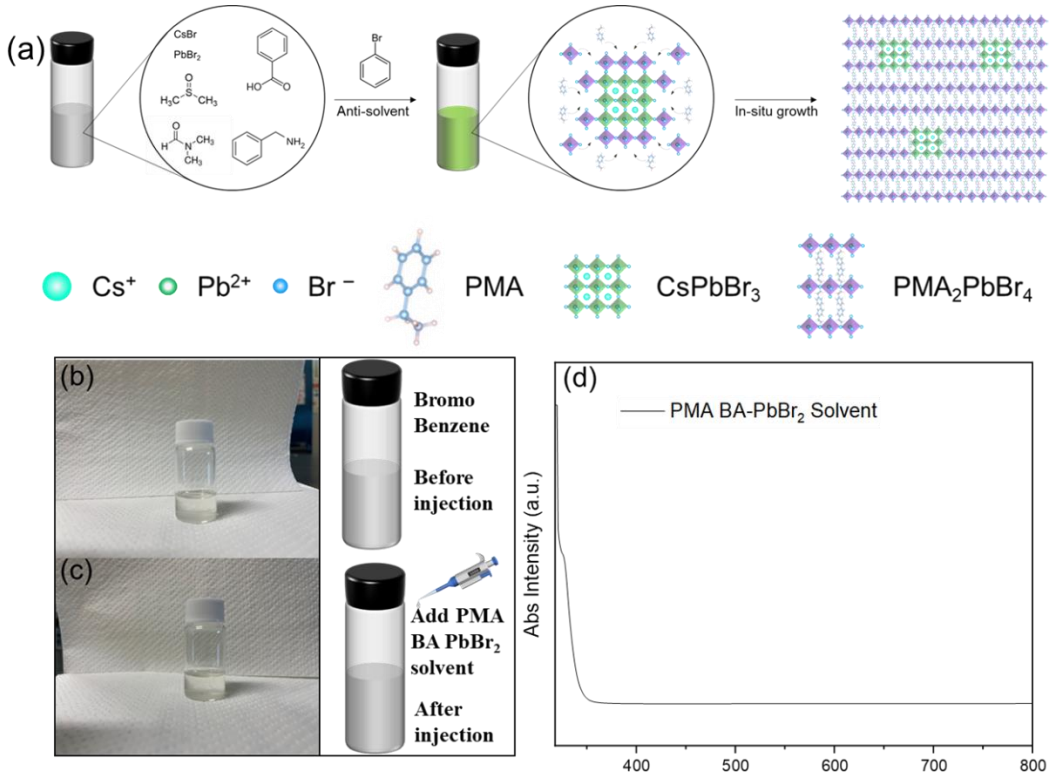

Figure 4-4. (a) Synthesis Schematic of 2D-3D PMA_2PbBr_4-$CsPbBr_3$ PNC. In the absence of Cs precursor, control experiments were conducted. Before and after the addition of the PMA BA-$PbBr_2$ precursor solution, there is no observable change in the solution. The absorption spectra also lack discernible signals, indicating that under the same conditions, the standalone synthesis of 2D PMA_2PbBr_4 is not feasible.

In Figure 4-5, the formation of the heterostructure is confirmed through STEM imaging. Due to the absence of long-chain ligands with substantial spatial hindrance, the lateral heterostructures of 2D-3D PNC are nearly fused together (Figures 4-5a, b). Further magnification in the high-resolution STEM reveals distinct color contrast, with black dots dispersed in PMA_2PbBr_4 indicating in situ formation of $CsPbBr_3$ nanocrystals on PMA_2PbBr_4 nanocrystals (white box in Figure 4-5c). High-resolution scanning transmission electron microscopy (HR-STEM) images clearly depict the lateral heterostructure of 2D-3D PNC. The interplanar distances of 0.297 Å and 0.468 Å correspond to the (002) and (007) crystal planes of $CsPbBr_3$ and PMA_2PbBr_4 nanocrystals, respectively (Figure 4-5d). Fourier transform analysis (FFT) of HRTEM images of 2D-3D PNC horizontally heterostructures reveals that $CsPbBr_3$ and PMA_2PbBr_4 project along the crystallographic (010) and (110) zone axes, respectively (Figure 4-5e, h). The corresponding crystallographic indices in reciprocal space are illustrated in Figure 4-5(f,i) distinguishing the contributions of $CsPbBr_3$ and PMA_2PbBr_4 nanocrystals. This is consistent with simulated results presented in Figure 4-5(g, j), demonstrating a perfect match between the reciprocal space indices of $CsPbBr_3$ and PMA_2PbBr_4 nanocrystals obtained experimentally and through simulation. Thus, the successful synthesis of 2D-3D PMA_2PbBr_4-$CsPbBr_3$ PNC is affirmed.

The formation of heterostructures indicates a preference for the in-situ heteroepitaxial growth of PMA_2PbBr_4 on the surface of $CsPbBr_3$ nanocrystals, without promoting the independent growth of PMA_2PbBr_4. In addition to the synthesis method, the successful synthesis of 2D-3D PNC lateral heterostructures benefits from minimal

lattice strain caused by crystal face mismatches as low as 0.94% and 1.35% for the (110), (008), (111), and (0010) crystal planes of $CsPbBr_3$ and PMA_2PbBr_4 nanocrystals, respectively. In contrast, the crystal face mismatches for (100) and (006) reach up to 5.61%, surpassing the maximum strain for in-situ heteroepitaxial growth (~ 5%)[19]. In the lateral heterostructure of 2D-3D PNC, $CsPbBr_3$ components exhibit slight low-angle misalignment on the (110) and (111) crystal planes, while PMA_2PbBr_4 components display mild high-angle misalignment (Figure 4-5e). This suggests lattice expansion (tensile strain) for $CsPbBr_3$ nanocrystals and lattice contraction (compressive strain) for PMA_2PbBr_4 nanocrystals. This reciprocal adjustment indicates their successful construction of heterostructures in the heterogeneous environment. Furthermore, it is emphasized that the synthesized $CsPbBr_3$ nanocrystals adopt a monoclinic phase instead of the typical cubic phase, evident from the distinct 30.6° diffraction peak splitting[18]. Moreover, characteristic diffraction peaks for metallic lead and PbBr2 salts are not observed at 18.4° and 31.3°[20-21]. This further confirms that heteroepitaxial anchoring occurs exclusively between pure $CsPbBr_3$ and PMA_2PbBr_4 nanocrystals, excluding metallic lead and PbBr2 salts from the process (depicted by the blue dashed lines in Figure 4-5e).

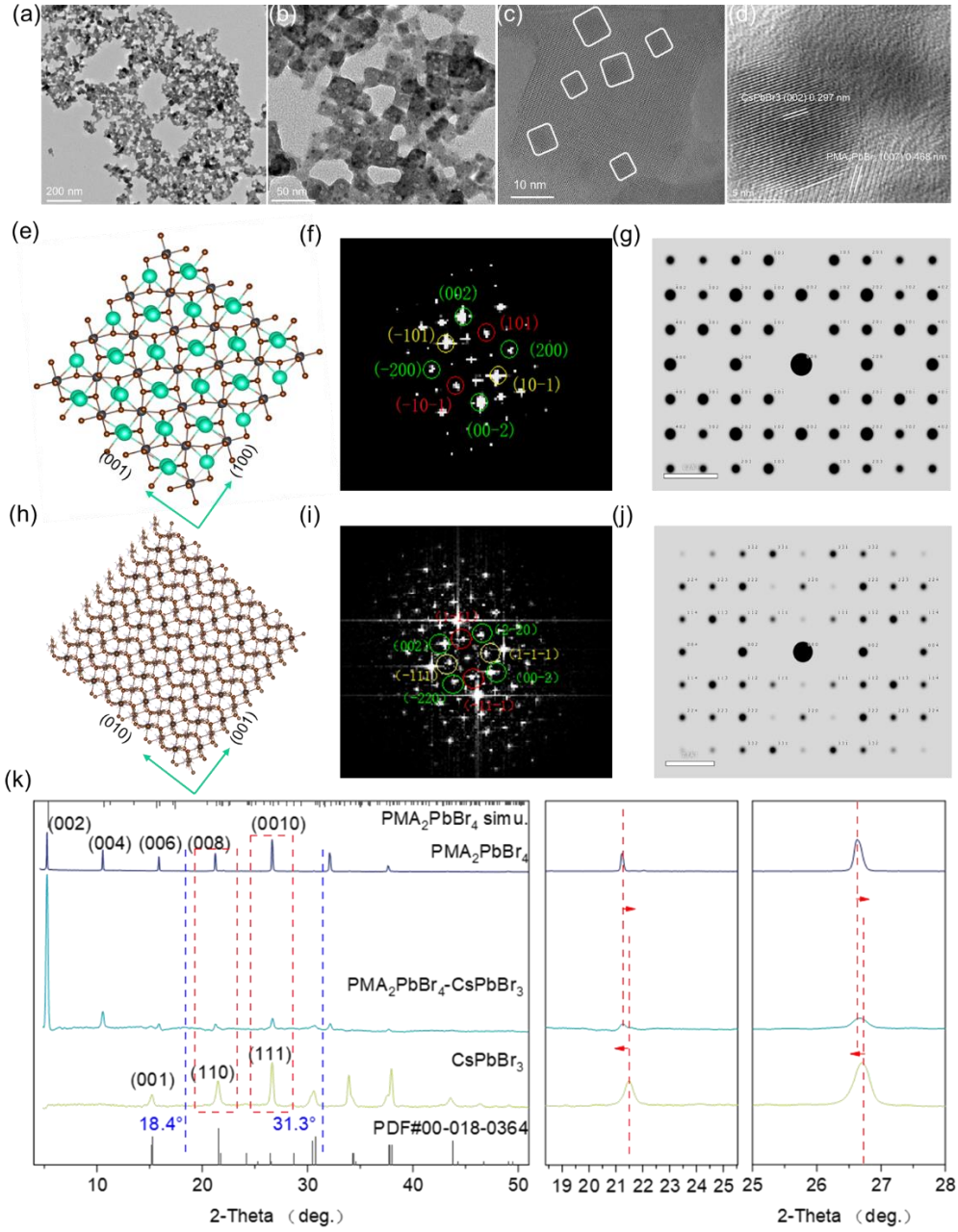

Figure 4-5. (a-d) STEM Images of 2D-3D PMA_2PbBr_4-$CsPbBr_3$ PNC. (e, h) Models of the (010) and (110) zone axis projections of 3D $CsPbBr_3$ and 2D PMA_2PbBr_4. (f, i) FFT of HRTEM images showing the (010) and (110) zone axis projections of 3D $CsPbBr_3$ and 2D PMA_2PbBr_4. (g, j) FFT Simulations of the (010) and (110) Zone Axis Projections for 3D $CsPbBr_3$ and 2D PMA_2PbBr_4.

To delve further into the structural intricacies of the 2D-3D PMA_2PbBr_4-$CsPbBr_3$ PNC horizontally heterojunctions, we have procured grazing incidence X-ray diffraction (GIXD) patterns for both the lateral heterojunction and its corresponding pure components (Figure 4-6a). The GIXD of pure 3D $CsPbBr_3$ nanocrystals manifests diffraction peaks indicative of the corresponding monoclinic phase. The broadening of these peaks implies a diminished size of $CsPbBr_3$ nanocrystals, approximately ~7.6 nm. This observation suggests that the epitaxial growth of PMA_2PbBr_4 terminates the growth of $CsPbBr_3$ nanocrystals. In contrast, the two-dimensional perovskite component exhibits narrower diffraction peaks due to its larger size, approximately ~25.8 nm. These peaks correspond to the (002) and (004) crystal planes of pure 2D PMA_2PbBr_4, denoted by the red dashed lines in Figure 4-6a. Additionally, the blue dashed line is attributed to the diffraction peaks of quasi-2D perovskite (n=2) structures[22-23]. Notably, these signals are absent in the 2D-3D PNC lateral heterojunction, and the GIXD of the heterojunction distinctly exhibits an overlay of $CsPbBr_3$ and PMA_2PbBr_4 nanocrystal diffraction peaks, confirming the successful synthesis of the 22D-3D PMA_2PbBr_4-$CsPbBr_3$ PNC horizontally heterojunctions. To ascertain the orientation of the 2D-3D PMA_2PbBr_4-$CsPbBr_3$ PNC horizontally heterojunctions, we conducted grazing incidence wide-angle X-ray scattering (GI-WAXs). In Figure 4-6b, the $CsPbBr_3$ nanocrystal film displays Debye-Scherrer rings at specific q values, indicating a random orientation of crystalline grains within the $CsPbBr_3$ nanocrystal film. In contrast, the 2D-3D PMA_2PbBr_4-$CsPbBr_3$ PNC horizontally heterojunctions film, depicted in Figure 4-6c, not only exhibits diffraction rings corresponding to

$CsPbBr_3$ nanocrystals but also reveals sharp and discrete Bragg spots along the q_z direction for PMA_2PbBr_4. This observation signifies a highly oriented alignment of crystal particles within the film. Analyzing the observed Bragg peaks, we confirm that PMA_2PbBr_4 is aligned along the (002) crystal plane, indicating a parallel alignment with the substrate[24]. In this context, we conclude that disordered $CsPbBr_3$ nanocrystals are directly connected and randomly distributed within the PMA_2PbBr_4, aligned parallel to the substrate. Furthermore, despite the additional presence of quasi-2D perovskite components, the two-dimensional perovskite film maintains its orientation parallel to the substrate, akin to pure 2D PMA_2PbBr_4.

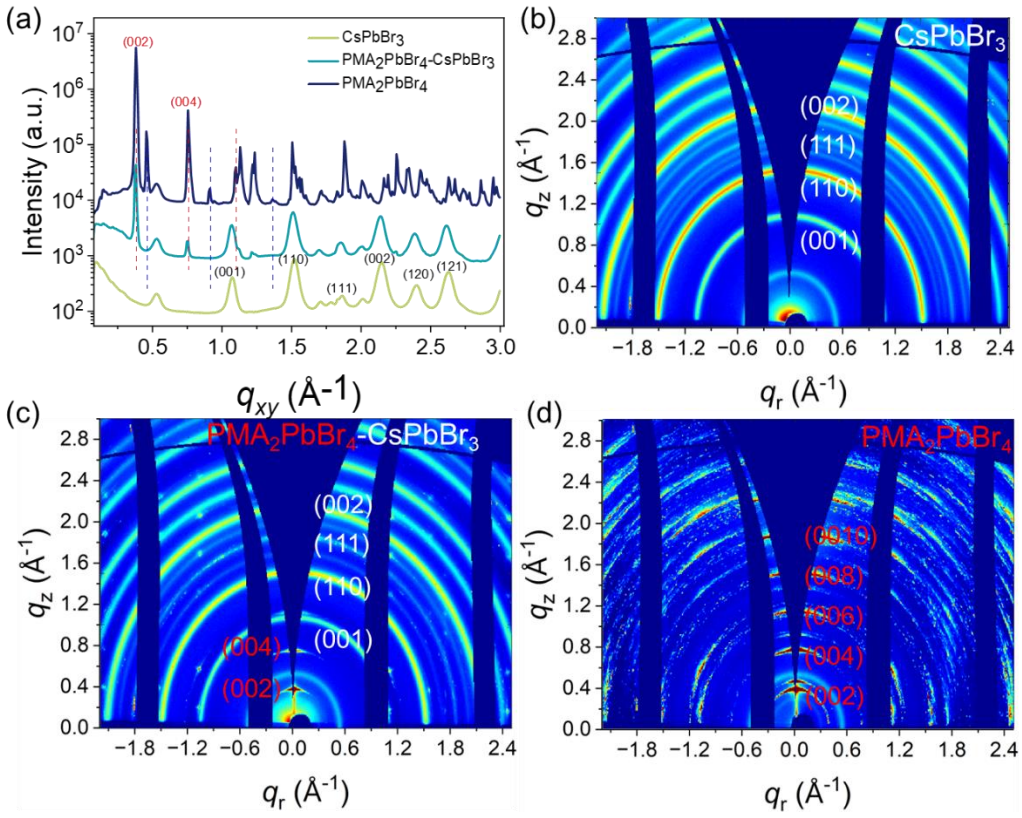

Figure 4-6. (a) GIXD patterns of $CsPbBr_3$, PMA_2PbBr_4, and 2D-3D PMA_2PbBr_4-$CsPbBr_3$ PNC horizontally heterojunctions. (b) GI-WAXs pattern of $CsPbBr_3$. (c) GI-WAXs image of 2D-3D PMA_2PbBr_4-$CsPbBr_3$ PNC horizontally heterojunctions. (d)

GI-WAXs pattern of PMA_2PbBr_4.

4.3.2 Optoelectronic property of 2D-3D perovskite nanocrystal horizontally heterojunctions

Figure 4-7 illustrates the spectral characteristics of the heterojunction. In Figure 4-7a, the 2D-3D PMA_2PbBr_4-$CsPbBr_3$ PNC horizontally heterojunctions exhibit distinct excitonic absorption peaks at 400 and 494 nm, corresponding to the absorptions of $CsPbBr_3$ and PMA_2PbBr_4 components, respectively. Comparative to the absorption peak positions, the photoluminescence wavelengths (PLW) are observed at 518 and 410 nm, showing a consistent Stokes shift trend. In comparison to the fluorescence of pure $CsPbBr_3$, the fluorescence color of the 2D-3D PMA_2PbBr_4-$CsPbBr_3$ PNC horizontally heterojunctions exhibit no apparent change, while the fluorescence intensity diminishes (as depicted in the inset of Figure 4-7a). The nearly constant fluorescence color is attributed to Föster energy transfer from PMA_2PbBr_4 to $CsPbBr_3$ within the 2D-3D PMA_2PbBr_4-$CsPbBr_3$ PNC horizontally heterojunctions, resulting in purple fluorescence at 410 nm as the donor (Figure 4-7b) and $CsPbBr_3$ acting as the acceptor[17].

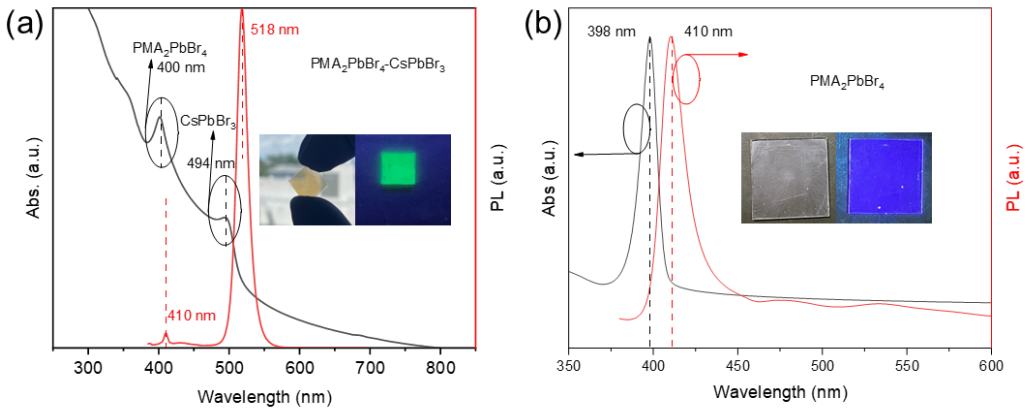

Figure 4-7. (a) PL and Abs. spectra of 2D-3D PMA_2PbBr_4-$CsPbBr_3$ PNC horizontally heterojunctions thin film. (b) PL and Abs. spectra of pure 2D PMA_2PbBr_4.

The decline in the fluorescence intensity of the 2D-3D PMA_2PbBr_4-$CsPbBr_3$ PNC horizontally heterojunctions is further illustrated in Figure 4-8a. In comparison to $CsPbBr_3$ nanocrystal films with traditional oleic acid and oleylamine as capping ligands, which exhibit an average photoluminescence quantum yield (PLQY) of 45.6%, the PLQY decreases to 7.1% when using oleic acid and benzylamine as ligands. Films obtained through solid-state ligand exchange exhibit a further reduction in PLQY to 2.1%, and the PLQY of 2D-3D PMA_2PbBr_4-$CsPbBr_3$ PNC horizontally heterojunction is 1.0%. Focusing on the latter two types of nanocrystal films, the notably low PLQY is attributed to two potential reasons: (1) the presence of a significant number of defect states in the nanocrystal or heterojunction film; (2) the rapid and efficient transfer of charge carriers in the nanocrystal film. To delve into the defect density within the two nanocrystal films, we further explore the light-intensity-dependent PL spectra, as depicted in Figure 4-8b. At extremely low light intensities, both the solid-state ligand exchange film and the 2D-3D PMA_2PbBr_4-$CsPbBr_3$ PNC horizontally heterojunction film undergo rapid defect filling processes. However, the fitting results ultimately reveal that the latter exhibits a smaller defect density ($4.74*10^{17}cm^{-3}$) compared to the former ($5.36*10^{17}cm^{-3}$). Additionally, due to the lower defect density in the 2D-3D PMA_2PbBr_4-$CsPbBr_3$ PNC horizontally heterojunction film, its time-resolved photoluminescence (TRPL) spectrum also demonstrates a fluorescence lifetime of up

to 82.5 ns, contrasting with the 19.5 ns observed in the solid-state ligand exchange film. However, this extended lifetime contradicts the 2D-3D PNC lateral heterojunction film's PLQY of ~1.0%. Therefore, we posit that the lower PLQY in the 2D-3D PMA_2PbBr_4-$CsPbBr_3$ PNC horizontally heterojunction film is attributed to a more rapid and efficient charge carrier transfer.

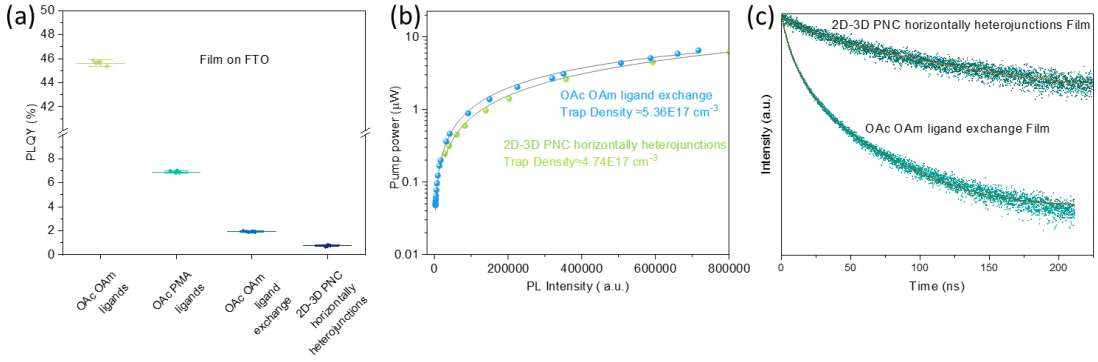

Figure 4-8. (a) PLQY of OAc OAm ligands, OAc PMA ligands, OAc OAm ligand exchange, and 2D-3D PMA_2PbBr_4-$CsPbBr_3$ PNC horizontally heterojunction thin films. (b) Light-intensity-dependent PL spectra for OAc OAm ligand exchange and 2D-3D PMA_2PbBr_4-$CsPbBr_3$ perovskite nanocrystal horizontally heterojunction thin films. (c) Time-resolved photoluminescence (TRPL) spectra of OAc OAm ligand exchange and 2D-3D PMA_2PbBr_4-$CsPbBr_3$ PNC horizontally heterojunction thin films.

The charge carrier transfer between these heterojunctions has been further confirmed through ultraviolet photoelectron spectroscopy (UPS) and ultraviolet-visible absorption spectroscopy (UV-Vis). As depicted in Figure 4-9, the work functions (φ) of $CsPbBr_3$ and PMA_2PbBr_4 are confirmed to be 4.56 and 4.85 eV, respectively (Figure 4-9 a,d). Their valence band maximums (VBMs) are determined to be 1.4 and 0.45 eV,

respectively (Figure 4-9 b,e). Through absorption spectroscopy, we ascertain that the band gaps of $CsPbBr_3$ and PMA_2PbBr_4 are 2.37 and 3.06 eV, respectively. Combining these data, we conclusively determine the band alignment of the 2D-3D PMA_2PbBr_4-$CsPbBr_3$ PNC horizontally heterojunction, as illustrated in Figure 4-9j. The n-type $CsPbBr_3$ and p-type PMA_2PbBr_4 form a type II heterojunction, a configuration previously proven to efficiently facilitate charge carrier transfer. This affirmation aligns with our experimental results presented earlier[25].

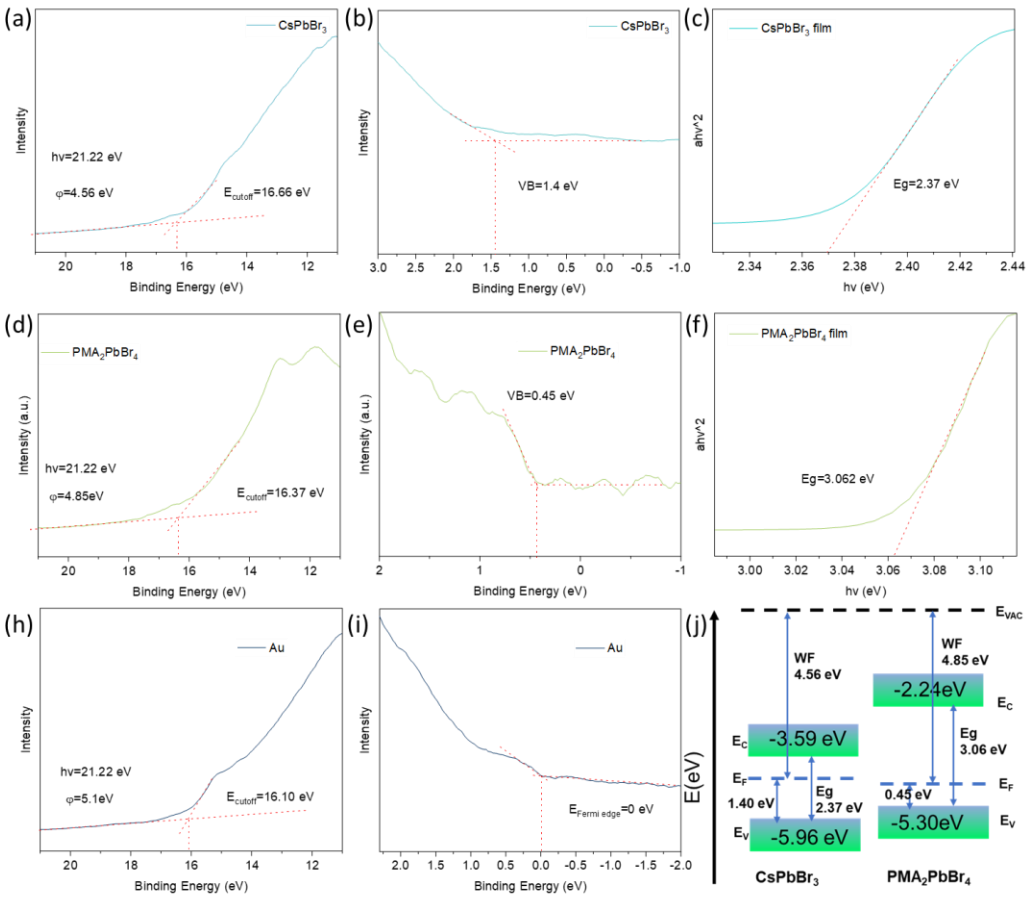

Figure 4-9. (a,b) Zoom-in UPS spectra of $CsPbBr_3$. (c) Tauc plot for $CsPbBr_3$. (d,e) Zoom-in UPS spectra of PMA_2PbBr_4. (f) Tauc plot for PMA_2PbBr_4. (h,i) Zoom-in UPS spectra of Au. (j) The schematic band alignment of 2D-3D PMA_2PbBr_4-$CsPbBr_3$ PNC

horizontally heterojunction.

The established pathway for unimpeded charge carrier transfer lays the foundation for the long-distance transport of carriers. Consequently, we scrutinized the transport properties of the 2D-3D PMA_2PbBr_4-$CsPbBr_3$ PNC horizontally heterojunction film, prepared through centrifugal deposition on glass[26]. For comparison, we employed a layer-by-layer deposition method to prepare a ligand-exchanged pure $CsPbBr_3$ nanocrystal film on glass[27] An equal concentration of Spiro and PCBM was spin-coated as hole and electron extraction layers, respectively, onto both films at the same rotation speed[28]. As illustrated in Figure 4-10 (a, c）, the green fluorescence emission of the 2D-3D PMA_2PbBr_4-$CsPbBr_3$ PNC horizontally heterojunction film decreases by 97.08% of its original intensity after spin-coating the Spiro layer. In contrast, the fluorescence of the ligand-exchanged $CsPbBr_3$ nanocrystal film decreases by 82.42% under the same conditions. Additionally, after spin-coating the PCBM layer, the fluorescence of the 2D-3D PMA_2PbBr_4-$CsPbBr_3$ PNC horizontally heterojunction film decreases by 99.70%, while the fluorescence of the ligand-exchanged $CsPbBr_3$ nanocrystal film decreases by 96.17%. This indicates superior performance in both electron and hole extraction for the 2D-3D PMA_2PbBr_4-$CsPbBr_3$ PNC horizontally heterojunction film compared to the traditional ligand-exchanged film. This superiority is further confirmed by time-resolved photoluminescence (TRPL) spectra, as shown in Figure 4-10 (b, d). The fluorescence lifetime of the 2D-3D PMA_2PbBr_4-$CsPbBr_3$ PNC horizontally heterojunction film is 9.2 ns, decreasing to 1.8 and 1.0 ns after spin-coating the Spiro

and PCBM layers, respectively. In contrast, the initial fluorescence lifetime of the ligand-exchanged $CsPbBr_3$ nanocrystal film is 6.0 ns, decreasing to 5.1 and 3.9 ns after spin-coating the Spiro and PCBM layers, respectively. The more substantial reduction in fluorescence lifetime in the 2D-3D PMA_2PbBr_4-$CsPbBr_3$ PNC horizontally heterojunction film indicates a more effective charge carrier transfer pathway. As shown in Table 4-1, the calculated diffusion coefficients (D_e, D_h) and mobilities (μ_e, μ_h) of electrons and holes in the 2D-3D PMA_2PbBr_4-$CsPbBr_3$ PNC horizontally heterojunction film are an order of magnitude larger than those in the ligand-exchanged film. Furthermore, the diffusion lengths (L_D^e, L_D^h) for electrons and holes in the 2D-3D PMA_2PbBr_4-$CsPbBr_3$ PNC horizontally heterojunction film reach 181 and 127 nm, respectively, surpassing those in the ligand-exchanged $CsPbBr_3$ nanocrystal film ($L_D^e = 49\ nm, L_D^h = 30\ nm$) (Figure 4-10e).

Table 4-1. The diffusion coefficients (D_e, D_h) and mobilities (μ_e, μ_h) of OAc OAm ligand exchange and 2D-3D PMA_2PbBr_4-$CsPbBr_3$ PNC horizontally heterojunctions thin films.

	D_e	D_h	μ_e	μ_h
	nm	nm	$cm^2V^{-1}S^{-1}$	$cm^2V^{-1}S^{-1}$
2D-3D PNC heterojunction	3.56E-2	1.76E-2	1.40	0.68
OAc OAm ligand exchange	3.83E-3	1.44E-3	0.15	0.056

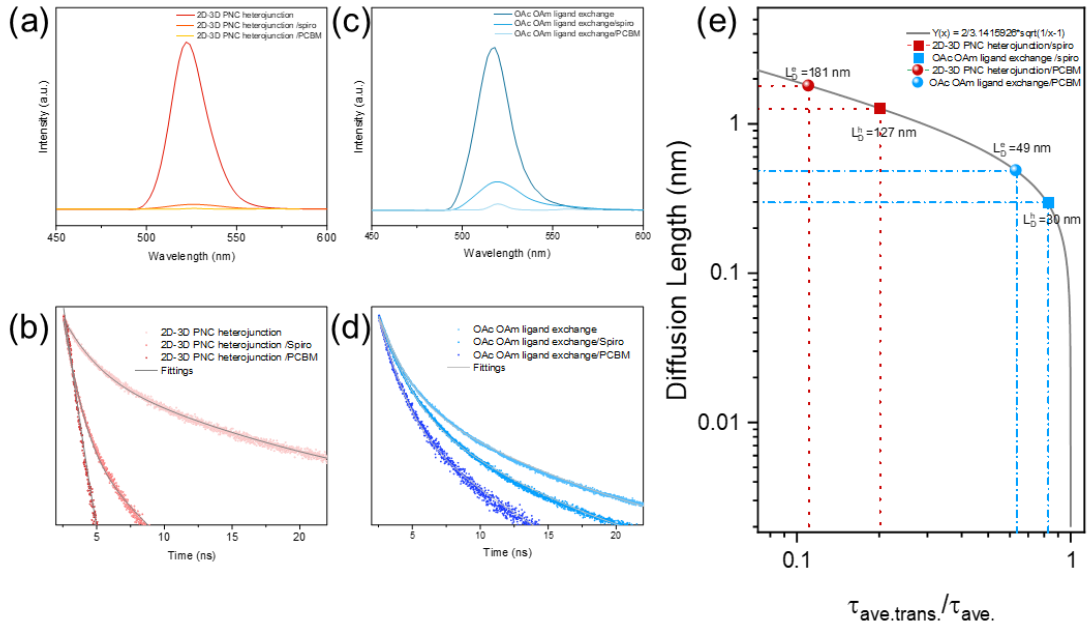

Figure 4-10. (a, c) The PL Intensity of OAc OAm ligand exchange and 2D-3D PMA_2PbBr_4-$CsPbBr_3$ PNC horizontally heterojunctions thin films with Original, Spiro-Coated and PCBM-Coated Layers. (b, d) The TRPL of OAc OAm ligand exchange and 2D-3D PMA_2PbBr_4-$CsPbBr_3$ PNC horizontally heterojunctions thin films with Original, Spiro- Coated and PCBM-Coated Layers. (e) Computational diffusion lengths (L_D^e, L_D^h) of OAc OAm ligand exchange and 2D-3D PMA_2PbBr_4-$CsPbBr_3$ PNC horizontally heterojunctions thin films.

To further investigate the optical properties of the 2D-3D PMA_2PbBr_4-$CsPbBr_3$ PNC horizontally heterojunction, we measured their temperature-dependent photoluminescence spectra. At room temperature, the 2D-3D PMA_2PbBr_4-$CsPbBr_3$ PNC horizontally heterojunction exhibits intrinsic fluorescence emission peaks at 408 and 510 nm, attributable to PMA_2PbBr_4 and $CsPbBr_3$, respectively. However, at 5 K, multiple new emission peaks emerge between 408 and 510 nm (Figure 4-11a). These

new fluorescence peaks appear at 436, 468, and 487 nm, initiating at temperatures below 260 K (here termed the critical temperature for the appearance of new fluorescence peaks). This critical temperature is significantly higher than the reported 220 K and 160 K critical temperatures for longitudinal heterojunctions[17], highlighting the distinct behavior between lateral and longitudinal heterojunctions. Furthermore, we ruled out the possibility that these new peaks originated from other quasi-2D perovskite phases, as their existence was not observed in XRD and ABS. To investigate the origin of these new peaks, we analyzed the temperature-dependent photoluminescence spectra. With increasing temperature, the apparent blue-shift in emission peaks from the 3D perovskite is primarily attributed to lattice thermal expansion. However, emissions from the 2D perovskite and the new peaks show either no shift or a slight blue-shift, indicating a competition between abundant electron-phonon interactions causing redshift and lattice thermal expansion causing blueshift. This competition offsets the effect of thermal expansion[28-29]. Another potential cause for the new emission peaks is vacancy defects, but previous studies suggested that the energy level changes induced by vacancy defects are approximately 0.1-0.2 eV, significantly smaller than the observed shift of approximately 0.5 eV. Therefore, we attribute these new emission peaks to more intense electron-phonon coupling resulting from lattice distortion in PMA_2PbBr_4[17, 30-31].

To validate our hypothesis, we employed graphical phase analysis to study the strain distribution at the interface of the 2D-3D PMA_2PbBr_4-$CsPbBr_3$ PNC horizontally heterojunction[32]. As shown in Figure 4-11(b,c), we first obtained the in-plane strain

distribution of $CsPbBr_3$, observing only ~5% average lattice strain near the heterojunction interface. In contrast, based on PMA_2PbBr_4, an average lattice strain of ~30% was observed in the in-plane strain distribution. Such significant lattice strain leads to the appearance of new emission peaks. Moreover, this strain magnitude exceeds that reported for longitudinally heterojunctions formed by intermolecular hydrogen bonding, indicating that chemically bonded lateral heterojunctions, while forming more stable structures and facilitating effective charge carrier transfer, also induce more severe lattice distortion. This distortion primarily occurs in PMA_2PbBr_4, as the elastic modulus of 2D perovskite is smaller than that of 3D perovskite[33], and stress can be relieved through octahedral distortion and relaxation of the organic layer.

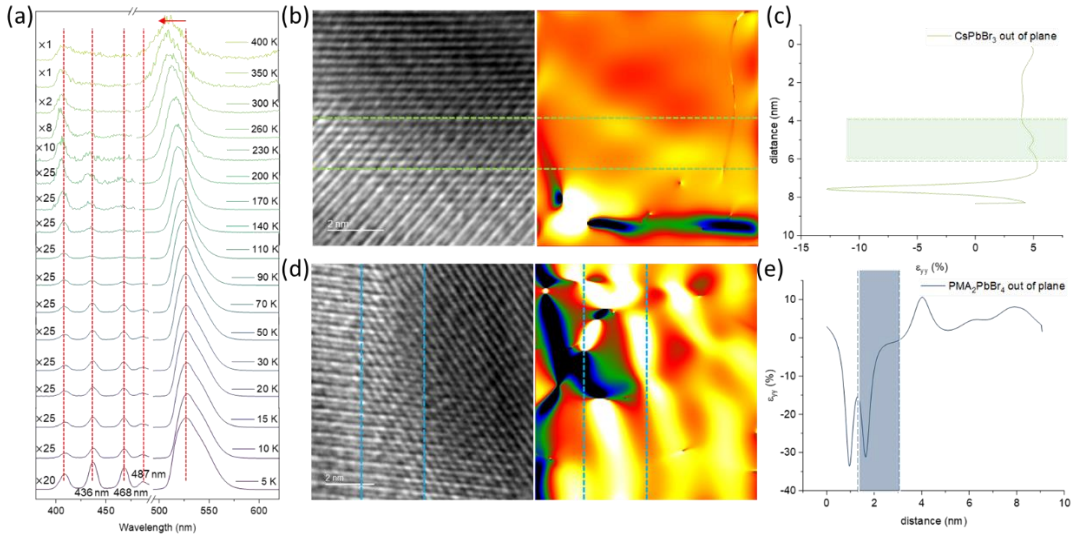

Figure 4-11. (a) Temperature-Dependent Fluorescence Spectra of 2D-3D PMA_2PbBr_4-$CsPbBr_3$ PNC horizontally heterojunction. (b) HRTEM Images of 2D-3D PMA_2PbBr_4-$CsPbBr_3$ PNC horizontally heterojunction and Strain Mapping Based on $CsPbBr_3$. (c) Out-of-Plane Strain Profiles Based on $CsPbBr_3$ in 2D-3D PMA_2PbBr_4-$CsPbBr_3$ PNC horizontally heterojunction. (d) HRTEM Images of 2D-3D PMA_2PbBr_4-$CsPbBr_3$ PNC

horizontally heterojunction and Strain Mapping Based on PMA_2PbBr_4. (e) Out-of-Plane Strain Profiles Based on PMA_2PbBr_4 in 2D-3D PMA_2PbBr_4-$CsPbBr_3$ PNC horizontally heterojunction.

4.3.3 Density Functional Theory (DFT) calculations of 2D-3D perovskite nanocrystal horizontally heterojunctions

To provide a theoretical elucidation of the formation and properties of the 2D-3D PMA_2PbBr_4-$CsPbBr_3$ PNC horizontally heterojunction, we conducted first-principles calculations on its properties. Figure 4-12a displays the local density of states for isolated $CsPbBr_3$, consistent with previous reports, where the conduction band minimum (CBM) and valence band maximum (VBM) of $CsPbBr_3$ are mainly contributed by Pb and Br elements. Similarly, PMA_2PbBr_4 exhibits a situation akin to $CsPbBr_3$, indicating that PMA has minimal impact on the band structure of PMA_2PbBr_4 (Figure 4-12b). This pattern is also observed in the local density of states for the 2D-3D PMA_2PbBr_4-$CsPbBr_3$ PNC horizontally heterojunction, suggesting that the optical properties of the 2D-3D PMA_2PbBr_4-$CsPbBr_3$ PNC horizontally heterojunction can be conveniently adjusted by tuning the metal cations and halogen anions. This aligns with our understanding of pure 3D perovskite nanocrystals (Figure 4-12c). Moreover, in the comparison of the local density of states for pure $CsPbBr_3$, PMA_2PbBr_4, and the 2D-3D PMA_2PbBr_4-$CsPbBr_3$ PNC horizontally heterojunction, we find that the latter has the smallest bandgap width. This aligns with the general understanding of type II

heterojunctions, as illustrated in Figure 4-12d.

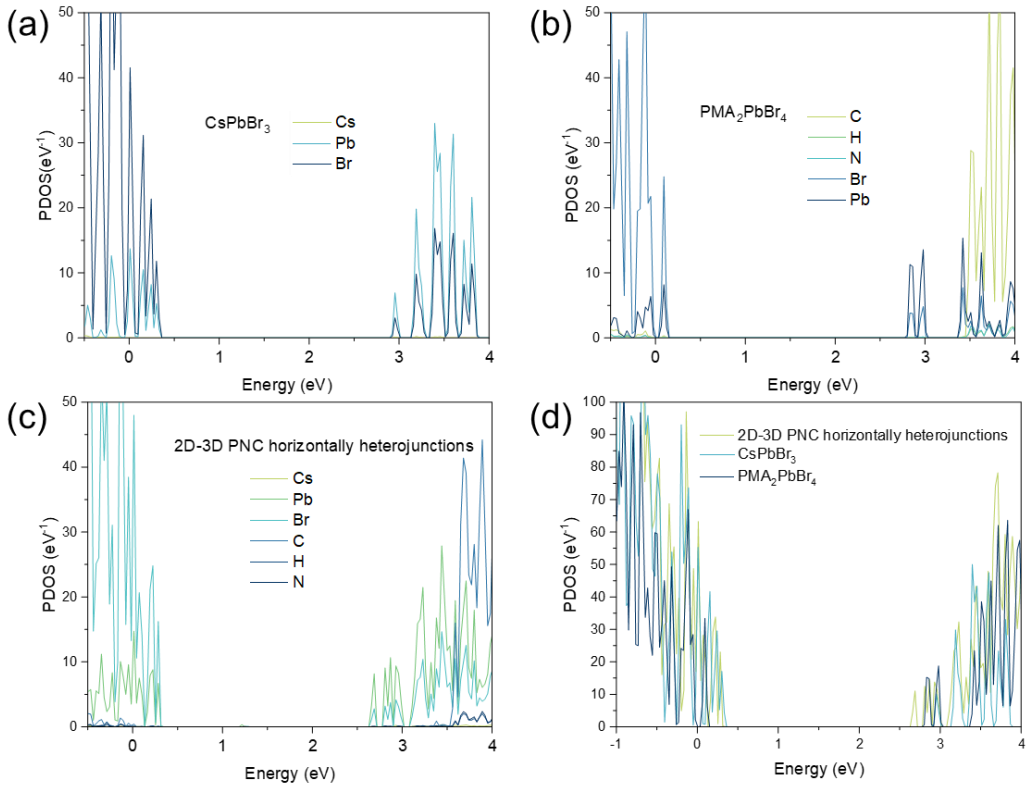

Figure 4-12. (a) Partial density of state (pDOS) of Cs, Pb, Br in $CsPbBr_3$ (b) Partial density of state pDOS of C, H, N, Pb, Br in PMA_2PbBr_4 (c) pDOS of C, H, N, Cs, Pb, Br in 2D-3D PMA_2PbBr_4-$CsPbBr_3$ PNC horizontally heterojunctions (d) pDOS of $CsPbBr_3$, PMA_2PbBr_4, 2D-3D PMA_2PbBr_4-$CsPbBr_3$ PNC horizontally heterojunctions

From a theoretical perspective on the formation of the 2D-3D PMA_2PbBr_4-$CsPbBr_3$ PNC horizontally heterojunction, we initially considered the role of PMA as a surface ligand for $CsPbBr_3$. As shown in Figure 4-13, PMA^+ is placed on the surface of the $CsPbBr_3$ model, and the calculated interface energy is -237 eV. Subsequently, the interface energy for forming a vertical heterojunction is calculated to be -343 eV. This indicates that whether PMA acts as a surface ligand or forms a longitudinal

heterojunction as 2D PMA_2PbBr_4, both scenarios are thermodynamically unstable (Figure 4-14a). In comparison, when forming a horizontally heterojunction with $CsPbBr_3$ on the (111) and (110) crystal faces, the interface energies for 2D PMA_2PbBr_4 are -1411 and -1761 eV, respectively (Figure 4-14c, e). This suggests a spontaneous tendency and a more stable structure for the formation of the lateral heterojunction, consistent with our experimental observations.

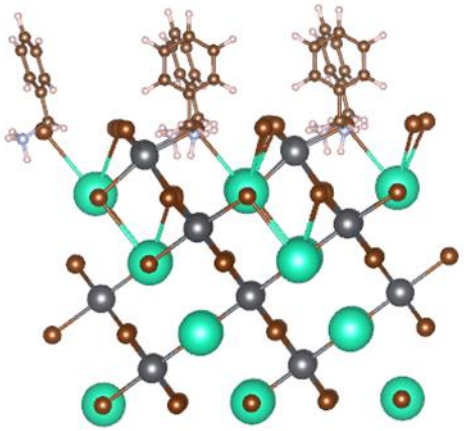

Figure 4-13. Structural model of $CsPbBr_3$ with PMA as the surface ligand

As shown in Figure 4-14a, the vertical heterojunction, formed with intermolecular hydrogen bonding as the binding mechanism, exhibits an indistinct charge density distribution on the 2D interface. This suggests that charge transfer is severely restricted. The planar-averaged total charge difference reveals the overall charge distribution in the system, as depicted in Figure 4-14b, where the average charge difference at the interface of the longitudinal heterojunction is ~0.12 eV. On the other hand, the lateral heterojunctions grown by epitaxial extension on the (111) crystal face of $CsPbBr_3$ exhibit a significant charge density distribution at the interface (Figure 4-14c). The average charge difference at the interface of the lateral heterojunction is ~0.45 eV

(Figure 4-14d). Similarly, lateral heterojunctions grown on the (110) crystal face of $CsPbBr_3$ also display a pronounced charge density distribution (Figure 4-14e), with an average charge difference at the interface of ~0.5 eV (Figure 4-14f). The fourfold larger average charge difference in lateral heterojunctions compared to vertical heterojunctions indicates more effective charge transfer in the former, aligning with the experimental observations.

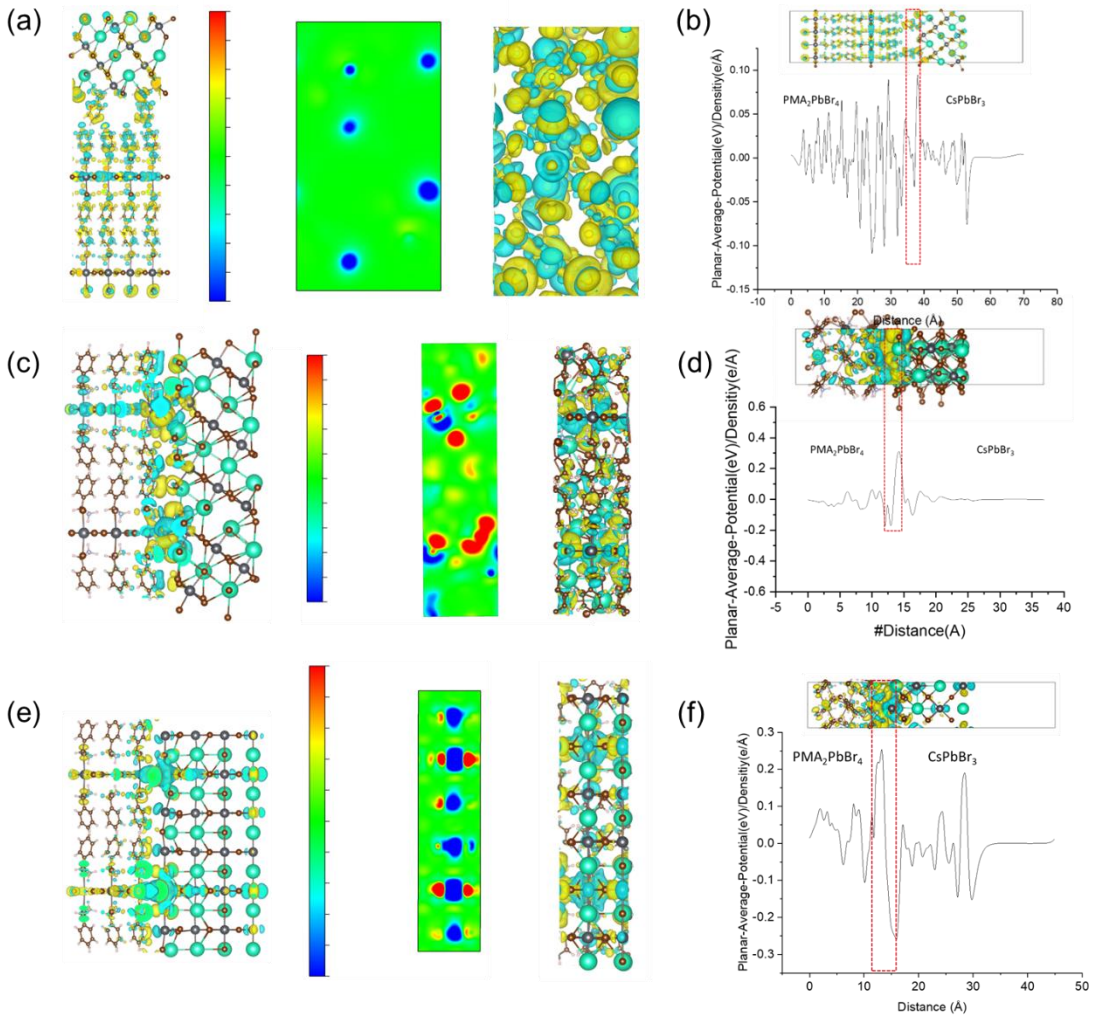

Figure 4-14. (a) Structural model and 2D Cross-Section at the interface of 2D-3D PMA_2PbBr_4-$CsPbBr_3$ PNC vertical heterojunctions. (b) Planar-Averaged total charge

difference in the vertical interface direction of 2D-3D PMA_2PbBr_4-$CsPbBr_3$ PNC vertical heterojunctions. (c, d) Structural model and 2D cross-section at the interface of 2D-3D PMA_2PbBr_4-$CsPbBr_3$ PNC horizontally heterojunctions with (111) crystal plane growth based on $CsPbBr_3$ (c), and Planar-averaged total charge difference in the vertical interface direction (d). (e, f) Structural model and 2D cross-section at the interface of 2D-3D PMA_2PbBr_4-$CsPbBr_3$ PNC horizontally heterojunctions with (110) crystal plane growth based on $CsPbBr_3$ (e), and Planar-averaged total charge difference in the vertical interface direction (f).

4.4 Summary

In conclusion, we have developed a straightforward and reproducible room-temperature in-situ synthesis method for the synthesis of low-cost processable 2D-3D PMA_2PbBr_4-$CsPbBr_3$ PNC horizontally heterojunction. This success is attributed to the implementation of a thermodynamically controlled experimental approach. Through various testing techniques such as STEM, GI-WAXs, we have demonstrated the successful synthesis of the heterojunction structure and the octahedra-to-octahedra binding mode. TRPL has unveiled outstanding charge diffusion lengths. Additionally, through DFT calculations, we have theoretically elucidated the thermodynamic control of the formation of 2D-3D PMA_2PbBr_4-$CsPbBr_3$ PNC horizontally heterojunction and the binding mode involving direct octahedral connections. Our study provides valuable insights into the synthesis of 2D-3D PMA_2PbBr_4-$CsPbBr_3$ PNC horizontally heterojunction, opening new avenues for their application in optoelectronic devices.

4.5 Bibliography

1. Akkerman, Q. A.; Gandini, M.; Di Stasio, F.; Rastogi, P.; Palazon, F.; Bertoni, G.; Ball, J. M.; Prato, M.; Petrozza, A.; Manna, L., Strongly emissive perovskite nanocrystal inks for high-voltage solar cells. *Nature Energy* **2016,** *2* (2), 1-7.

2. Hassan, Y.; Park, J. H.; Crawford, M. L.; Sadhanala, A.; Lee, J.; Sadighian, J. C.; Mosconi, E.; Shivanna, R.; Radicchi, E.; Jeong, M., Ligand-engineered bandgap stability in mixed-halide perovskite LEDs. *Nature* **2021,** *591* (7848), 72-77.

3. Yi, L.; Hou, B.; Zhao, H.; Liu, X., X-ray-to-visible light-field detection through pixelated colour conversion. *Nature* **2023**, 1-6.

4. Zhu, X.; Lin, Y.; San Martin, J.; Sun, Y.; Zhu, D.; Yan, Y., Lead halide perovskites for photocatalytic organic synthesis. *Nature communications* **2019,** *10* (1), 2843.

5. Song, W.; Wang, D.; Tian, J.; Qi, G.; Wu, M.; Liu, S.; Wang, T.; Wang, B.; Yao, Y.; Zou, Z., Encapsulation of Dual-Passivated Perovskite Quantum Dots for Bio-Imaging. *Small* **2022,** *18* (42), 2204763.

6. Dutta, A.; Behera, R. K.; Pal, P.; Baitalik, S.; Pradhan, N., Near-unity photoluminescence quantum efficiency for all CsPbX3 (X= Cl, Br, and I) perovskite nanocrystals: a generic synthesis approach. *Angewandte Chemie International Edition* **2019,** *58* (17), 5552-5556.

7. Akkerman, Q. A.; Rainò, G.; Kovalenko, M. V.; Manna, L., Genesis, challenges and opportunities for colloidal lead halide perovskite nanocrystals. *Nature materials* **2018,** *17* (5), 394-405.

8. Mannar, S.; Mandal, P.; Roy, A.; Viswanatha, R., Experimental determination of the molar absorption coefficient of cesium lead halide perovskite quantum dots. *The Journal of Physical Chemistry Letters* **2022,** *13* (27), 6290-6297.

9. Gutiérrez Álvarez, S.; Lin, W.; Abdellah, M.; Meng, J.; Zidek, K.; Pullerits, T. n.; Zheng, K., Charge carrier diffusion dynamics in multisized quaternary alkylammonium-capped CsPbBr3 perovskite nanocrystal solids. *ACS Applied Materials & Interfaces* **2021,** *13* (37), 44742-44750.

10. Wei, K.; Jiang, T.; Xu, Z.; Zhou, J.; You, J.; Tang, Y.; Li, H.; Chen, R.; Zheng, X.;

Wang, S., Ultrafast carrier transfer promoted by interlayer coulomb coupling in 2D/3D perovskite heterostructures. *Laser & Photonics Reviews* **2018,** *12* (10), 1800128.

11. Li, C.; Pan, Y.; Hu, J.; Qiu, S.; Zhang, C.; Yang, Y.; Chen, S.; Liu, X.; Brabec, C. J.; Nazeeruddin, M. K., Vertically aligned 2D/3D Pb–Sn perovskites with enhanced charge extraction and suppressed phase segregation for efficient printable solar cells. *ACS Energy Letters* **2020,** *5* (5), 1386-1395.

12. Sidhik, S.; Wang, Y.; De Siena, M.; Asadpour, R.; Torma, A. J.; Terlier, T.; Ho, K.; Li, W.; Puthirath, A. B.; Shuai, X., Deterministic fabrication of 3D/2D perovskite bilayer stacks for durable and efficient solar cells. *Science* **2022,** *377* (6613), 1425-1430.

13. Ma, K.; Sun, J.; Atapattu, H. R.; Larson, B. W.; Yang, H.; Sun, D.; Chen, K.; Wang, K.; Lee, Y.; Tang, Y., Holistic energy landscape management in 2D/3D heterojunction via molecular engineering for efficient perovskite solar cells. *Science Advances* **2023,** *9* (23), eadg0032.

14. Hu, Y.; Schlipf, J.; Wussler, M.; Petrus, M. L.; Jaegermann, W.; Bein, T.; Müller-Buschbaum, P.; Docampo, P., Hybrid perovskite/perovskite heterojunction solar cells. *ACS nano* **2016,** *10* (6), 5999-6007.

15. McGott, D. L.; Muzzillo, C. P.; Perkins, C. L.; Berry, J. J.; Zhu, K.; Duenow, J. N.; Colegrove, E.; Wolden, C. A.; Reese, M. O., 3D/2D passivation as a secret to success for polycrystalline thin-film solar cells. *Joule* **2021,** *5* (5), 1057-1073.

16. Xu, X.; Qian, W.; Wang, J.; Yang, J.; Chen, J.; Xiao, S.; Ge, Y.; Yang, S., Sequential Growth of 2D/3D Double-Layer Perovskite Films with Superior X-Ray Detection Performance. *Advanced Science* **2021,** *8* (21), 2102730.

17. Zhu, Z.; Zhu, C.; Yang, L.; Chen, Q.; Zhang, L.; Dai, J.; Cao, J.; Zeng, S.; Wang, Z.; Wang, Z., Room-temperature epitaxial welding of 3D and 2D perovskites. *Nature Materials* **2022,** *21* (9), 1042-1049.

18. Li, X.; Wu, Y.; Zhang, S.; Cai, B.; Gu, Y.; Song, J.; Zeng, H., CsPbX3 quantum dots for lighting and displays: room-temperature synthesis, photoluminescence superiorities, underlying origins and white light-emitting diodes. *Advanced Functional Materials* **2016,** *26* (15), 2435-2445.

19. Liu, J.; Zhang, J., Nanointerface chemistry: Lattice-mismatch-directed synthesis and application of hybrid nanocrystals. *Chemical reviews* **2020,** *120* (4), 2123-2170.

20. Liang, J.; Hu, X.; Wang, C.; Liang, C.; Chen, C.; Xiao, M.; Li, J.; Tao, C.; Xing, G.; Yu, R., Origins and influences of metallic lead in perovskite solar cells. *Joule* **2022,** *6* (4), 816-833.

21. Fang, X.; Zhang, K.; Li, Y.; Yao, L.; Zhang, Y.; Wang, Y.; Zhai, W.; Tao, L.; Du, H.; Ran, G., Effect of excess PbBr2 on photoluminescence spectra of CH3NH3PbBr3 perovskite particles at room temperature. *Applied Physics Letters* **2016,** *108* (7).

22. Liu, Y.; Akin, S.; Pan, L.; Uchida, R.; Arora, N.; Milić, J. V.; Hinderhofer, A.; Schreiber, F.; Uhl, A. R.; Zakeeruddin, S. M., Ultrahydrophobic 3D/2D fluoroarene bilayer-based water-resistant perovskite solar cells with efficiencies exceeding 22%. *Science advances* **2019,** *5* (6), eaaw2543.

23. Duan, Y.; Oropeza, F. E.; Jin, X.; Amargós-Reyes, O.; Atoini, Y.; Cavinato, L. M.; Nagy, G. N.; Kahaly, M. U.; de la Peña O'Shea, V. A.; Wang, D. Y., Holy Water: Photo-Brightening in Quasi-2D Perovskite Films under Ambient Enables Highly Performing Light-Emitting Diodes. *Advanced Functional Materials* **2023,** *33* (7), 2209249.

24. Chen, A. Z.; Shiu, M.; Ma, J. H.; Alpert, M. R.; Zhang, D.; Foley, B. J.; Smilgies, D.-M.; Lee, S.-H.; Choi, J. J., Origin of vertical orientation in two-dimensional metal halide perovskites and its effect on photovoltaic performance. *Nature communications* **2018,** *9* (1), 1336.

25. Kuo, M.-Y.; Spitha, N.; Hautzinger, M. P.; Hsieh, P.-L.; Li, J.; Pan, D.; Zhao, Y.; Chen, L.-J.; Huang, M. H.; Jin, S., Distinct carrier transport properties across horizontally vs vertically oriented heterostructures of 2D/3D perovskites. *Journal of the American Chemical Society* **2021,** *143* (13), 4969-4978.

26. Kim, Y.; Yassitepe, E.; Voznyy, O.; Comin, R.; Walters, G.; Gong, X.; Kanjanaboos, P.; Nogueira, A. F.; Sargent, E. H., Efficient luminescence from perovskite quantum dot solids. *ACS applied materials & interfaces* **2015,** *7* (45), 25007-25013.

27. Wheeler, L. M.; Sanehira, E. M.; Marshall, A. R.; Schulz, P.; Suri, M.; Anderson, N. C.; Christians, J. A.; Nordlund, D.; Sokaras, D.; Kroll, T., Targeted ligand-exchange

chemistry on cesium lead halide perovskite quantum dots for high-efficiency photovoltaics. *Journal of the American Chemical Society* **2018,** *140* (33), 10504-10513.

28. Wang, S.; Ma, J.; Li, W.; Wang, J.; Wang, H.; Shen, H.; Li, J.; Wang, J.; Luo, H.; Li, D., Temperature-dependent band gap in two-dimensional perovskites: Thermal expansion interaction and electron–phonon interaction. *The journal of physical chemistry letters* **2019,** *10* (10), 2546-2553.

29. Long, H.; Peng, X.; Lu, J.; Lin, K.; Xie, L.; Zhang, B.; Ying, L.; Wei, Z., Exciton–phonon interaction in quasi-two dimensional layered (PEA) 2 (CsPbBr 3) n− 1 PbBr 4 perovskite. *Nanoscale* **2019,** *11* (45), 21867-21871.

30. Ni, L.; Huynh, U.; Cheminal, A.; Thomas, T. H.; Shivanna, R.; Hinrichsen, T. F.; Ahmad, S.; Sadhanala, A.; Rao, A., Real-time observation of exciton–phonon coupling dynamics in self-assembled hybrid perovskite quantum wells. *ACS nano* **2017,** *11* (11), 10834-10843.

31. Wu, X.; Trinh, M. T.; Niesner, D.; Zhu, H.; Norman, Z.; Owen, J. S.; Yaffe, O.; Kudisch, B. J.; Zhu, X.-Y., Trap states in lead iodide perovskites. *Journal of the American Chemical Society* **2015,** *137* (5), 2089-2096.

32. Hÿtch, M.; Snoeck, E.; Kilaas, R., Quantitative measurement of displacement and strain fields from HREM micrographs. *Ultramicroscopy* **1998,** *74* (3), 131-146.

33. Wang, H.; Zhu, C.; Liu, L.; Ma, S.; Liu, P.; Wu, J.; Shi, C.; Du, Q.; Hao, Y.; Xiang, S., Interfacial residual stress relaxation in perovskite solar cells with improved stability. *Advanced Materials* **2019,** *31* (48), 1904408.

Chapter 5 Conclusion and prospective

5.1 Summary

In this manuscript, our primary focus lies in the investigation of the synthetic chemistry and photophysical properties of in situ-grown perovskite nanocrystal heterostructures at room temperature, as elucidated in Chapters 3 and 4. Our research advances a one-step synthesis methodology for in situ constructing perovskite nanocrystal heterostructures at room temperature, deepening our comprehension of in situ epitaxial growth of heterostructures. Additionally, we provide an insightful elucidation of the carrier transfer dynamics induced by these heterostructures. The novelty and significance of our study are outlined as follows:

In Chapter 3:

- For the first time, we employ a one-step, dynamically controlled in situ epitaxial synthesis to produce $CsPbBr_3$-PbS quantum dot heterostructures.
- By manipulating the Pb/S molar ratio, the fluorescence of $CsPbBr_3$-PbS quantum dot heterostructures can be conveniently tuned. Time-resolved absorption spectroscopy (TAS) reveals rapid carrier transfer dynamics (initiation time <1 ps).
- We introduce the application of $CsPbBr_3$-PbS quantum dot heterostructures in the shortwave infrared (SWIR) region, achieving a resolution of 3.44 μm and demonstrating superior imaging capabilities compared to pure PbS quantum dots.

In Chapter 4:

- For the first time, we employ a one-step, thermodynamically controlled in situ epitaxial synthesis to produce 2D-3D PMA_2PbBr_4-$CsPbBr_3$ PNC horizontally heterojunction.
- The octahedral direct connectivity in 2D-3D PMA_2PbBr_4-$CsPbBr_3$ PNC horizontally heterojunction enhances carrier diffusion lengths ($L_D^e = 49\ nm, L_D^h = 30\ nm$).
- Through Density Functional Theory (DFT) calculations, we theoretically reveal the thermodynamic control behind synthesizing 2D-3D PMA_2PbBr_4-$CsPbBr_3$ PNC horizontally heterojunction.

5.2 Future work

Our work, rooted in the development of perovskite nanocrystals, has pioneered a one-step synthesis approach for in situ epitaxial formation of heterostructures at room temperature. We have delved into the photophysical properties, providing profound insights into the understanding of perovskite nanocrystal heterostructures. However, several challenges persist, demanding resolution for the commercial application of perovskite nanocrystal heterostructures:

1. In our research, the reactivity of $(TMS)_2S$ as a sulfur source is excessively high, hindering the precise control of PbS size formation. Moreover, $(TMS)_2S$ causes severe etching of $CsPbBr_3$, introducing defects that impede achieving a high PLQY. Thus, there is a need to explore a suitable sulfur source that facilitates the controlled formation of PbS on the surface of $CsPbBr_3$.

2. 2D-3D PMA_2PbBr_4-$CsPbBr_3$ PNC horizontally heterojunction exhibit a high carrier diffusion length, yet their sensitivity to moisture and inability to form monodisperse states in solution, due to the lack of organic ligand protection and steric hindrance effects, pose challenges. Hence, identifying a suitable ligand that offers protection and dispersion without compromising carrier diffusion is crucial.

3. The carrier diffusion in 2D-3D PMA_2PbBr_4-$CsPbBr_3$ PNC horizontally heterojunction is limited to in-plane diffusion. Introducing a self-assembly process to vertically assemble 2D-3D PMA_2PbBr_4-$CsPbBr_3$ PNC horizontally heterojunction into thin films could significantly enhance their application in the field of solar cells.

In summary, challenges and opportunities coexist, and the exploration and resolution of challenges underscore the essence of scientific endeavor. I believe that delving deeper into the study of heterostructures based on perovskite nanocrystals holds great promise.

List of publications

Papers

Yongge Yang, Dandan Wang, Yusheng Li, Jing Xia, Huiyun Wei, Chao Ding, Yuyu Hu, Yuyao Wei, Hua Li, Dong Liu, Guozheng Shi, Yaohong Zhang, Huan Bi, Shikai Chen, Hongshi Li, Xiang-Min Meng, Shuzi Hayase, and Qing Shen In Situ Room-Temperature Synthesis of All-Colloidal Quantum Dot $CsPbBr_3$–PbS Heterostructures. 11. 2023. 10.1021/acsphotonics.3c01099

Dandan Wang, Yusheng Li, Yongge Yang, Chao Ding, Qing Shen Unveiling of efficiency limit to fabricate high-performance PbSe quantum dot solar cells Solar Energy, 2022, 247: 432-440

Dandan Wang , Yusheng Li , Yongge Yang , Shuzi Hayase , Haifeng Wu , Ruixiang Wang , Chao Ding , Qing Shen How to minimize voltage and fill factor losses to achieve over 20% efficiency lead chalcogenide quantum dot solar cells: Strategies expected through numerical simulation Applied Energy, 2023, 341: 121124

Yuyao Wei, Mako Nakamura, Chao Ding, Dong Liu, Hua Li, Yusheng Li, Yongge Yang, Dandan Wang, Ruixiang Wang, Shuzi Hayase, Taizo Masuda, and Qing Shen Unraveling the Organic and Inorganic Passivation Mechanism of ZnO Nanowires for Construction of Efficient Bulk Heterojunction Quantum Dot Solar Cells ACS Applied Materials & Interfaces, 2022, 14(31): 36268-36276.

Hua Li, Qing Wang, Yusuke Oteki, Chao Ding, Dong Liu, Yao Guo, Yusheng Li, Yuyao Wei, Dandan Wang, Yongge Yang, Taizo Masuda, Mengmeng Chen, Zheng Zhang, Tomah Sogabe, Shuzi Hayase, Yoshitaka Okada, Satoshi Iikubo, Qing Shen Enhanced Hot-Phonon Bottleneck Effect on Slowing Hot Carrier Cooling in Metal Halide

Perovskite Quantum Dots with Alloyed A-Site . Advanced Materials, 2023: 2301834.

Yusheng Li, Dandan Wang ,Shuzi Hayase, Yongge Yang, Chao Ding and Qing Shen Efficient Exciton Dislocation and Ultrafast Charge Extraction in $CsPbI_3$ Perovskite Quantum Dots by Using Fullerene Derivative as Semiconductor Ligand. Nanomaterials, 2022, 12(18): 3101

Huan Bi, Jiaqi Liu, Raminta Beresneviciute, Daiva Tavgeniene, Zheng Zhang, Liang Wang, Gaurav Kapil, Chao Ding, Shahrir Razey Sahamir, Yoshitaka Sanehira, Ajay Kumar Baranwal, Takeshi Kitamura, Dandan Wang, Yuyao Wei, Yongge Yang, Dong-Won Kang, Saulius Grigalevicius, Qing Shen, and Shuzi Hayase Efficiency Enhancement of Wide Bandgap Lead Perovskite Solar Cells with PTAA Surface-Passivated with Monomolecular Layer from the Viewpoint of PTAA Band Bending ACS Applied Materials & Interfaces 2023, 15, 35, 41549–41559

Huan Bi, Jiaqi Liu, Zheng Zhang, Liang Wang, Gaurav Kapil, Yuyao Wei, Ajay Kumar Baranwal, Shahrir Razey Sahamir, Yoshitaka Sanehira, Dandan Wang, Yongge Yang, Takeshi Kitamura, Raminta Beresneviciute, Saulius Grigalevicius, Qing Shen, Shuzi Hayase Ferrocene Derivatives for Improving the Efficiency and Stability of MA-Free Perovskite Solar Cells from the Perspective of Inhibiting Ion Migration and Releasing Film Stress. Advanced Science, 2023: 2304790.

Conference Presentations

Poster: Yongge Yang, Chao Ding, Qing Shen1 Research and Application on Stability and Non-toxicity of Halide Perovskite Materials and Its Fluorescence Properties. nanoGe Spring Meeting 2022 (Spain)

Poster: Yongge Yang, Yusheng Li, Dandan Wang, Hua Li, Dong Liu, Yuyao Wei, Shuzi Hayase, Chao Ding, Qing Shen Short-ligand perovskite quantum dot films with high

conductivity and their thermoelectric performances. PVSEC-33 (Nagoya, Japan)

Poster: Yongge Yang, Chao Ding, Shuzi Hayase, Qing Shen Research on Synthesis and Properties of Stable Perovskite Materials. 10.57295/jpvsproc.2.0_67. 第 19 回「次世代の太陽光発電システム」シンポジ ウム（第 2 回日本太陽光発電学会学術講演会）

Acknowledgements

First and foremost, I would like to express my heartfelt gratitude to Professor Qing Shen, my mentor, for her invaluable guidance and support throughout my doctoral journey. Her dedication to scientific research and meticulous approach has greatly benefited me. I extend my thanks to Professor Hayase for the support provided in testing. I am grateful for the financial support from JST, enabling me to focus on scientific research. Dr. Yusheng Li deserves special thanks for his detailed assistance and care, both in research and daily life. His profound theoretical knowledge and keen scientific intuition have been truly inspiring, making him a role model in my research endeavors. Additionally, I would like to express my sincere appreciation to Dr. Dandan Wang for her valuable advice and assistance in scientific matters. Moreover, as a witness to the love story between Dr. Li Yusheng and Dr. Dandan Wang, and as their colleague and friend, I wholeheartedly wish them a future filled with happiness. I extend my gratitude to Dr. Chao Ding for his guidance in scientific research and imparting knowledge and experimental skills. Thanks to Dr. Yao Hong Zhang and Dr. Guozheng Shi for their assistance and support in research. Dr. Dong Liu, Dr. Hua Li, Dr. Yuyao Wei, Dr. Huan Bi, and Dr. Zheng Zhang, I appreciate your help both in research and daily life. Dr. Zitao Ni, thank you for your assistance and support in DFT theoretical calculations. Special thanks to Mr. Akihito Fuchimoto, Mr. Keita Tosa, and Mr. Kei Takahashi for their help in language and experiments. Lastly, I want to convey my heartfelt thanks to my parents and sister for their understanding and support in my pursuit of a doctoral

degree. I am grateful for my sister and her husband's dedication to our parents during my doctoral studies. A special thank you to my life partner, Ms. Yanmin Duan, for her continuous dedication and support.